Springer Theses
Recognizing Outstanding Ph.D. Research

Sarah Elizabeth Morgan

Ultrafast Quantum Effects and Vibrational Dynamics in Organic and Biological Systems

Springer

Springer Theses

Recognizing Outstanding Ph.D. Research

Aims and Scope

The series "Springer Theses" brings together a selection of the very best Ph.D. theses from around the world and across the physical sciences. Nominated and endorsed by two recognized specialists, each published volume has been selected for its scientific excellence and the high impact of its contents for the pertinent field of research. For greater accessibility to non-specialists, the published versions include an extended introduction, as well as a foreword by the student's supervisor explaining the special relevance of the work for the field. As a whole, the series will provide a valuable resource both for newcomers to the research fields described, and for other scientists seeking detailed background information on special questions. Finally, it provides an accredited documentation of the valuable contributions made by today's younger generation of scientists.

Theses are accepted into the series by invited nomination only and must fulfill all of the following criteria

- They must be written in good English.
- The topic should fall within the confines of Chemistry, Physics, Earth Sciences, Engineering and related interdisciplinary fields such as Materials, Nanoscience, Chemical Engineering, Complex Systems and Biophysics.
- The work reported in the thesis must represent a significant scientific advance.
- If the thesis includes previously published material, permission to reproduce this must be gained from the respective copyright holder.
- They must have been examined and passed during the 12 months prior to nomination.
- Each thesis should include a foreword by the supervisor outlining the significance of its content.
- The theses should have a clearly defined structure including an introduction accessible to scientists not expert in that particular field.

More information about this series at http://www.springer.com/series/8790

Sarah Elizabeth Morgan

Ultrafast Quantum Effects and Vibrational Dynamics in Organic and Biological Systems

Doctoral Thesis accepted by
the University of Cambridge, UK

Springer

Author
Dr. Sarah Elizabeth Morgan
Theory of Condensed Matter Group,
Department of Physics
University of Cambridge
Cambridge
UK

Supervisor
Dr. Alex W. Chin
Theory of Condensed Matter Group,
Department of Physics
University of Cambridge
Cambridge
UK

ISSN 2190-5053 ISSN 2190-5061 (electronic)
Springer Theses
ISBN 978-3-319-63398-5 ISBN 978-3-319-63399-2 (eBook)
DOI 10.1007/978-3-319-63399-2

Library of Congress Control Number: 2017946654

Printed on acid-free paper

This Springer imprint is published by Springer Nature
The registered company is Springer International Publishing AG
The registered company address is: Gewerbestrasse 11, 6330 Cham, Switzerland

Supervisor's Foreword

The remarkable efficiency and reliability of photosynthetic light reactions has been studied for many decades, giving us important insight into how sustainable solar energy transduction is directed by the molecular optoelectronics of biological nanostructures [1]. However, the recent and unexpected observation of robust quantum dynamics in photosynthetic complexes has challenged our fundamental understanding of biological photophysics, raising profound debates, and much interdisciplinary research, on the possible roles of quantum mechanics in biological and organic systems [2]. Understanding how such ephemeral and non-classical processes can impact the efficiency of organic light harvesting materials not only sheds new light on the marvels and intricacy of functional biological nanostructures; it could also provide a route towards new quantum design principles for artificial energy technologies [3]. At the same time, these processes challenge us to develop the theoretical tools capable of describing the complexity of the novel, real-time, non-equilibrium dynamics whose exploitation may prove to be just as important as basic electronic structure for the next generation of efficient energy materials.

Dr. Morgan's thesis is an important contribution to this exciting new field and focuses on the theoretical prediction and analysis of the sophisticated ultrafast optical spectra that probe the crucial first few picoseconds of quantum light harvesting. By studying the novel photophysics of thin films of organic pentacene, Dr. Morgan's doctoral work provides new insight into the process of singlet fission, a quantum mechanical effect that allows a single photon to be "doubled" into two electron-hole pairs, potentially boosting the efficiency of organic photovoltaics. Simulating the ultrafast nonlinear spectra of pentacene films, Dr. Morgan identified the experimental signatures of an entangled intermediate state, normally "dark" to standard optical probes, that leads to fission on sub-picosecond timescales [4]. Proving that this novel detection arises from quantum vibrational effects, this thesis also reports a collaboratively developed wavelet method to identify similar vibronic dynamics in photosynthetic reaction centres. This was then applied to real spectroscopic data to test the robustness of recently proposed quantum transport mechanisms in which vibronic effects generate coherent wave-like dynamics, even

in the presence of the aggressive fluctuation "noise" in the surrounding protein environment [5].

Such "noisy" interactions are the fundamental origin of energy dissipation and the—normally—rapid degradation of quantum effects in nanostructured systems. Elucidating the microscopic physics of protein vibrations is therefore of vital importance in the quest to understand how quantum effects can be stabilised and harnessed in molecular devices. The final part of this thesis looks at the dynamics of vibrational energy in real protein structures, using molecular dynamics and coarse-grained models to understand the role of nonlinear vibrational modes that, *inter alia,* can transfer vibrational energy over extremely long distances and/or even harvest it from their surroundings when excited out of equilibrium [6]. The structure-function relations underlying these rich protein dynamics have many potential applications for light harvesting functions, as well as an impact on several medically relevant, but still not well understood, biological processes such as allostery.

It is an immense pleasure to write this foreword for Dr. Morgan's thesis, which is a body of work that testifies, on every page, to her outstanding creativity and intellectual bravery. I am sure that every one of Dr. Morgan's many experimental and theoretical collaborators will be as inspired, delighted and proud as I am that this work has been recognised for this prestigious Springer Thesis Prize, and I look forward with great anticipation to seeing how the many deeply mined gems of theoretical insight contained in this thesis will inspire further work through the publication of this monograph.

Cambridge, UK
May 2017

Dr. Alex W. Chin

References

1. Blankenship, R.E.: Molecular Mechanisms of Photosynthesis. Wiley (2013)
2. Lambert, N., Chen, Y.N., Cheng, Y.C., Li, C.M., Chen, G.Y., Nori, F.: Quantum Biology. Nat. Phys. **9**(1), 10–18 (2013)
3. Scholes, G.D., Fleming, G.R., Chen, L.X., Aspuru-Guzik, A., Buchleitner, A., Coker, D.F., Lundeen, J.S.: Using coherence to enhance function in chemical and biophysical systems. Nature **543**(7647), 647–656 (2017)
4. Bakulin, A.A., Morgan, S.E., Kehoe, T.B., Wilson, M.W., Chin, A.W., Egorova, D., Rao, A.: Real-time observation of multiexcitonic states in ultrafast singlet fission using coherent 2D electronic spectroscopy. Nat. Chem. **8**, 16–23 (2016)
5. Romero, E., Prior, J., Chin, A.W., Morgan, S.E., Novoderezhkin, V.I., Plenio, M.B., van Grondelle, R.: Quantum coherent dynamics in photosynthetic charge separation revealed by wavelet analysis. Sci. Rep. **7**, 2890 (2017)
6. Morgan, S.E., Cole, D.J., Chin, A.W.: Nonlinear network model analysis of vibrational energy transfer and localisation in the Fenna-Matthews-Olson complex. Sci. Rep. **6**, 36703 (2016)

Abstract

Recently, evidence has emerged that quantum coherences can be sustained in photosynthetic complexes over much longer timescales than initially expected. This evidence comes predominantly from a new technique called 2D electronic spectroscopy (2DES), which provides unprecedented access to the ultrafast quantum and vibrational dynamics of organic and biological systems. Intriguing suggestions have been made that these quantum coherences might be sustained or even regenerated by molecular vibrations; however, a full understanding of their origins has proved elusive. This is due to the exceptional difficulty of interpreting 2DES experiments, combined with the complexity of the underlying biological systems.

One approach to tackling these challenges is to study simpler organic molecules first, which nonetheless exhibit fascinating ultrafast photophysics and have useful applications for photovoltaics. Therefore, here, I begin by presenting an extensive theoretical analysis of 2DES data for the organic material pentacene, which undergoes a novel process known as singlet fission. This work elucidates "dark" entangled states in pentacene and the importance of vibrations during fission.

Time-frequency analysis offers an opportunity to extract further information from oscillatory 2DES signals. I discuss the difficulties surrounding using time-frequency analysis to distinguish non-trivial regeneration of electronic coherences from interferences between vibrational modes. I use 2DES data from photosystem II as an example and propose that theoretical simulations are essential to unravel these complicated effects.

Ultimately, microscopic analysis of vibrations is required to fully understand the complex relationship between electronic and vibrational dynamics in organic and biological systems. This analysis may be particularly important for nonlinear collective protein modes. Therefore, in the final chapter, I use the nonlinear network model and molecular dynamics simulations to study vibrations in the Fenna–Matthews–Olson complex (FMO). This work suggests that localised, nonlinear discrete breather modes might be formed in biologically relevant parts of FMO and that the optical properties of FMO could be altered by protein vibrations. Overall, this approach represents a promising avenue for further research.

Acknowledgements

Firstly, I would like to thank my supervisor, Alex Chin, for his excellent advice, patience and unquenchable optimism, without which this dissertation would not have been possible. I have also been lucky to work with several fantastic experimentalists, including Artem Bakulin, Akshay Rao, Andrew Musser and Hannah Stern in Cambridge, as well as Eli Romero and Rienk van Grondelle from VU Amsterdam. On the theory side, Danny Cole made substantial contributions to the work on FMO and made many helpful suggestions. Dassia Egorova had significant input into the work on pentacene, in particular the simulations of the ultrafast dynamics, whilst the work on wavelet analysis of PSII builds on Javier Prior's work.

Sam Smith has always been happy to share ideas and both he and Tom Price have been great office-mates throughout. Several other friends have also been extremely supportive, not least Laura Brooks, Rosie Mantell, Helen Smalley and Catrin Treharne.

Eros Mariani first introduced me to condensed matter theory and encouraged me to begin my studies in Cambridge. Towards the end of my Ph.D., Petra Vértes has helped to inspire my interest in complex networks and has been incredibly generous with her time in doing so.

Above all, I would like to thank my family—Mum, Dad, Ba, Zoë, Ben, Sam and my wider family—for their constant support and encouragement. It means the world to me.

Contents

Nomenclature

Roman Symbols

E	Energy
$\vec{E}$	Electric field
$\hbar$	Reduced Planck constant
H	Hamiltonian
J	Electronic coupling
J_s	Spectral density function
$\vec{k}$	Wavevector
$\vec{P}$	Polarisation
q	Charge
$\vec{r}$	Displacement
R_c	Cut-off distance
$S_{R/NR}$	Rephasing/non-rephasing 2D signal
S_1	Singlet state
S	Huang-Rhys factor
t_d	Detection time
Tr	Trace
T	Waiting time
t	Time
TT_n	Higher lying multiexciton state
TT	Multiexciton state
U_0	Time evolution operator

Greek Symbols

β	$1/k_BT$, where k_B is the Boltzmann constant and T is the temperature
χ	Susceptibility
δ	Dirac delta function

ε	Permittivity
ε_0	Permittivity of free space
$\vec{\mu}$	Transition dipole moment
ω	Frequency
ϕ	Wavefunction
ρ	Density matrix
σ	Charge distribution
τ	Coherence time
ω_c	Cut-off frequency
ω_τ	Absorption frequency
ω_{t_d}	Emission frequency

Acronyms/Abbreviations

2D	Two dimensional
2DES	Two-dimensional electronic spectroscopy
Å	Angstrom
BChl	Bacteriochlorophyll
bRC	Bacterial reaction centre
C_α	Carbon alpha atom
CD	Circular dichroism
CT	Charge transfer
CWT	Continuous wavelet transform
DB	Discrete breather
DO	Displaced harmonic oscillator
DTP	6,13-di(2-thienyl) pentacene
ED	Electronic dimer
ENM	Elastic network model
ESA	Excited state absorption
eV	Electron volt
FMO	Fenna–Matthews–Olson complex
fs	Femtosecond
GSB	Ground-state bleach
h.c.	Hermitian conjugate
HOMO	Highest occupied molecular orbital
LA	Linear absorption
LD	Linear dichroism
LUMO	Lowest unoccupied molecular orbital
NADP	Nicotinamide adenine dinucleotide phosphate
NM	Normal mode
NMR	Nuclear magnetic resonance
NNM	Nonlinear network model
NR	Non-rephasing
PPC	Pigment–protein complex

ps	Picosecond
PSI	Photosystem I
PSII	Photosystem II
R	Rephasing
Rb	Rhodobacter
RC	Reaction centre
Re	Real
SE	Stimulated emission
TEDOPA	Time Evolving Density with Orthogonal Polynomial Algorithm
TIPS	6,13-bis(triisopropyl-silylethynyl) pentacene

Chapter 1
Introduction

If the 20th century was the century of physics, the 21st century will be the century of biology.,
Craig Venter and Daniel Cohen [1]

The 20th century witnessed huge breakthroughs in physics, perhaps most spectacularly the foundation of quantum mechanics in the 1920s. It is no exaggeration to say that quantum mechanics fundamentally changed our world view, whilst opening the gate to technologies which were unimaginable one hundred years ago, including modern computers. In turn, this computational revolution has allowed us to create and store increasing amounts of data. Big data is particularly valuable in biology and is now available in a myriad of forms, from protein data banks to genetic data. Overall, it may be tempting to imagine that physics is now broadly understood and the next scientific challenges are biological.

And yet it is increasingly clear that the quantitative approach of physics is essential to understand and model these complex biological systems. Meanwhile, thanks to experimental advances and our ability to interrogate biological systems with ever greater resolution, intriguing suggestions of quantum mechanical effects in biology have emerged. These quantum effects are remarkably long-lived at room temperature and have been proposed to participate in a range of biological functions, from energy transfer to charge separation. Perhaps biology has something new to teach us about physics? Undoubtedly nature has benefited from millions of years of evolution and may have learnt to stabilise quantum processes through nanostructuring and dynamical environmental engineering. Understanding and exploiting these design principles could be the key to the next generation of quantum technologies.

This dissertation aims to build a better picture of both quantum (electronic) and vibrational dynamics in organic and biological light harvesting systems and to elucidate the interplay between electronic coherences and vibrational modes. An excitonic framework is required to study these systems, which I introduce in the second chapter.

S.E. Morgan, *Ultrafast Quantum Effects and Vibrational Dynamics in Organic and Biological Systems*, Springer Theses, DOI 10.1007/978-3-319-63399-2_1

No system exists in complete isolation from its environment and work has shown that the dissipative dynamics of biological light harvesting complexes can be non-trivial [2], hence I also discuss approaches to modelling dissipative processes. These techniques come from the field of open quantum sytems, which is described in detail by Weiss [3]. In the latter part of the second chapter I introduce a novel ultrafast technique known as two-dimensional electronic spectroscopy (2DES). 2DES is a relatively new experimental technique which is the optical equivalent of 2D infrared spectroscopy and stems from that literature [4]. The ultrafast nature of 2DES and the quantity of information contained within 2DES spectra make it an ideal probe of organic and biological systems and in recent years 2DES has been instrumental in observing long-lived electronic coherences in photosynthetic pigment protein complexes (PPCs) [4–8]. PPCs are large proteins with light absorbing pigments embedded in them, and perform key energy and electron transfer processes during photosynthesis. The protein is often thought of as a scaffold, holding the pigments in place and tuning the complex interactions between pigments by changing the distance between them and their relative orientations. For a description of the different types of PPCs and their role in photosynthesis, see Blankenship [9].

One archetypal PPC is the Fenna-Matthews-Olson complex (FMO), which is found in green sulfur bacteria and is responsible for transferring energy excitations to the bacterial reaction centre (RC). Green sulfur bacteria live deep at the bottom of the ocean and hence are exposed to very little light and need to perform photosynthesis efficiently. In 2007, Engel et al. were the first to apply 2DES to study FMO and observed long-lived (660 fs) quantum coherence between the electronic excitations of pigments at a temperature of 77K. This observation was surprising, as quantum effects are not normally expected to survive in the 'warm, wet and noisy' environments of biological systems. The result also led to intriguing and controversial suggestions that quantum coherences might contribute functionally to the high efficiency of energy transfer in photosynthetic light harvesting complexes. If this is the case, understanding the origins and function of electronic coherences in biological light harvesting complexes could lead to design principles for building more efficient artificial photovoltaic systems. Since 2007, other experimental work has confirmed and elucidated the existence of quantum coherences in PPCs. Several authors have focussed on light harvesting reaction centres, which are the PPCs responsible for charge separation during photosynthesis. For example, in 2012 Westenhoff et al. used cross-polarised 2D spectroscopy to observe oscillations in a bacterial reaction centre known as *Rhodobacter (Rb.) sphaeroides* which lasted for over 1 ps [10]; see Fig. 1.1. In 2014, Romero et al. and Fuller et al. both observed long-lived oscillations in the photosystem II (PSII) RC [11, 12]. These are just some examples and detailed reviews of quantum coherence signals observed in light harvesting complexes can be found in [4, 7]. A thorough introduction to the broad field of quantum effects in biological systems is given by Mohseni et al. [8] and includes discussions of open quantum system approaches to biology as well as describing applications beyond photosynthesis, for example avian navigation.

However, whilst the 2DES experiments used to observe these effects contain crucial information, the sheer volume of data they produce makes them difficult to

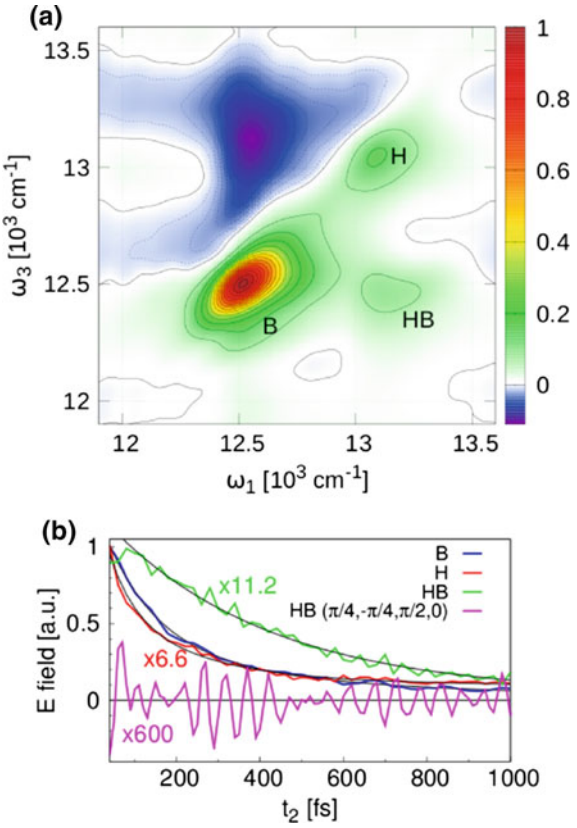

Fig. 1.1 **a** 2D spectrum where the cross-peak (labelled HB) provides evidence for electronic coherence between two states labelled H and B. **b** Time traces taken at different points in the spectrum. The *pink lin*e plots the amplitude of peak HB over the waiting time with a cross-polarisation pulse sequence. Long lived oscillations are observed for at least 1 ps. Figure adapted with permission from [10]. Copyright 2012 American Chemical Society

interpret and a key challenge is distinguishing the oscillatory signals produced by electronic coherences from the many intermolecular and intramolecular vibrations which exist in PPCs. The picture is complicated by the fact that photosynthetic complexes have several vibrational and electronic states and the energy gaps between electronic states are often resonant with vibrational modes. There is now growing consensus within the literature that many of the signals observed have mixed vibrational/electronic origins [2, 8, 13–15] and that the interplay between these different origins is often complex. For example, in 2012 Christensson et al. proposed a vibronic exciton model to describe the long-lived oscillations observed in FMO [13]. In 2013, theoretical work by Chin et al. [2] suggested that vibrations can help to sustain electronic coherences, rather than destroying them as is normally expected. Chin et al. used a numerically exact approach (the Time Evolving Density with Orthogonal Polynomial Algorithm, TEDOPA) to model coherences in FMO; the results are shown in Fig. 1.2. Crucially, they employed a spectral density (a function used to model the environment) which includes an underdamped discrete mode close to resonance with the energy difference between two important electronic states. The key insight behind their paper is that this underdamped mode couples different excitonic

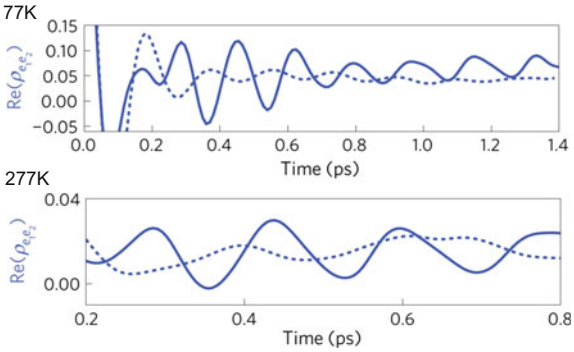

Fig. 1.2 Numerically exact (TEDOPA) simulation results for the dynamics of a key electronic coherence in FMO at 77 K and 277 K. The *bold line* shows the dynamics when the resonant mode is included, whereas for the *dotted line* the resonant mode is not included. Including the resonant mode leads to significantly longer lived electronic coherences. Figure adapted from [2]

states via non adiabatic terms (outside of the Born-Oppenheimer approximation) and can therefore generate and sustain electronic coherences in a non-equilibrium manner. Other theoretical work has also suggested that vibrations can play important non-trivial and sometimes counter-intuitive roles in these systems [14, 16].

With this emerging vibronic picture of biological systems and the difficulties of interpreting 2DES experiments in mind, in the third chapter I present recent work carried out in collaboration with experimentalists who applied 2DES to thin films of the organic semi-conductor pentacene [17]. Pentacene is an organic molecule composed of five fused benzene rings. Organic materials have similar excitonic descriptions and photophysics to their biological counterparts, but are generally more stable, with simpler structures and fewer electronic states. Hence they provide a useful first step towards studying 2DES of biological light harvesting systems. They also have interesting photovoltaic applications in their own right. For example, pentacene undergoes singlet fission; a '2 for 1' process which generates two charge carriers from a single photon. This process can increase the maximum theoretical energy efficiency of solar cells [18], overcoming the Shockley-Queisser limit which limits the maximum energy efficiency to 33.7% [19], and hence has attracted significant attention in recent years. Our work provides the first direct evidence of the entangled multiexcitonic state which is believed to mediate fission and is normally considered to be optically dark, i.e. it has no significant transition dipole moment. We show that vibrational coupling can allow this dark state to borrow dipole moment from the nearby bright singlet state and we propose a theoretical model for pentacene which incorporates vibrations on an equal footing with the electronic states. Our model is able to reproduce the experimental 2DES spectra of pentacene thin films, as well as the ultrafast timescale of fission in this material which is less than 100 femtoseconds. Our results underline the importance of vibrations in the singlet fission process,

echoing many of the same themes discussed in the literature for biological PPCs [2, 13–15, 20].

One approach which has been suggested to elucidate vibrational and electronic effects in biological systems is to further interrogate 2DES data using time-frequency analysis [21]. In this type of analysis, instead of working entirely in the time domain (by inspecting the time series) or entirely in the frequency domain (by taking a Fourier transform of the time series), it is possible to trade some time information for frequency information. In this way, as well as knowing the approximate frequencies at which the signal oscillates, we can also learn information about the times at which those different frequencies of oscillation occur. Whilst having complete information concerning the times at which different frequencies occur is never possible due to the Heisenberg uncertainty principle, partial information can still be extremely valuable. In the fourth chapter, I examine the advantages and limitations of applying a particular time-frequency analysis approach known as 'wavelet analysis' to experimental 2DES results from biological light harvesting systems. In particular, I discuss the difficulty of distinguishing two signals which might arise in the 2DES results: (1) signals from the regeneration of electronic coherences driven by vibrational modes and (2) signals from interference between vibrational modes with similar frequencies. The former, non-trivial signals are of significant interest to the quantum biology community, as described above, whilst the latter are an inevitable consequence of the number of closely spaced vibrational modes which exist in biological light harvesting complexes. Although these signals are in principle indistinguishable, additional information can be extracted from their context in the 2DES data. As an example of the challenges involved in wavelet analysis of biological data, I present work applying these ideas to 2DES data from the plant reaction centre photosystem II, building on the work by Romero et al. [11] mentioned above.

In the future, more work on the molecular origins of the vibrations themselves is required to build a deeper understanding of the complex interplay between vibrations and electronic states in organic and biological systems. For example, in pentacene the role of specific vibrations in driving singlet fission could be studied at an electronic structure level by considering dimer systems, in which the molecules are more constrained than in thin films. Meanwhile, in PPCs collective protein modes have been suggested to play an important role in the electron and energy transfer processes [22–24]. One promising approach to studying these proteins is to treat them as networks, in which each node represents an atom or a group of atoms and connections are made between atoms which interact. Molecular dynamics simulations can then be used to analyse the modes of the system and are able to capture a surprising amount of the underlying physics, as seen by comparison to NMR experiments [25]. Interestingly, when anharmonic terms are included these models often exhibit novel vibrational dynamics known as 'discrete breather modes' [26]. Surprisingly, the nonlinear nature of these modes enables them to harvest energy from their surroundings and localise energy in specific parts of the pigment protein complex. Hence they represent a fruitful avenue for further research into energy transfer in PPCs.

Therefore, in the final chapter of this dissertation I use a nonlinear network model to study the dynamics and optical spectra of FMO. I calculate the normal modes

of the system and show that discrete breather modes can arise in the dynamics. Remarkably, these discrete breather modes are able to transfer energy to biologically important parts of the protein- near to key pigments which have been shown to transfer energy from the FMO complex into the reaction centre. The formation of the discrete breathers also introduces low frequency (picosecond timescale), high amplitude oscillations into the pigment energies, which could provide interesting alternative energy transfer pathways. Finally, I show that optical spectra calculations based on *ab initio* calculations of the site energies and interpigment couplings from Cole et al. [27] can be brought significantly closer to experimental results by incorporating a mode which approximates the discrete breather dynamics. This work suggests promising new avenues for using network methods to discover functional vibrations which can significantly alter electronic dynamics. These effects may be even more important for biological systems where light induces conformation changes, for example catalysis, vision and DNA repair. In general, the ability of network methods to traverse temporal and spatial scales makes them a particularly powerful tool for studying complex biological systems, from protein structure networks to structural and functional networks in the human brain.

In conclusion, studying analogous organic and biological systems simultaneously can give significant insights into the ultrafast processes in both at the molecular level. Expertise from across physics and biology is required to understand how complex functional systems and networks emerge from the intricate interactions between excitons and vibrations of multiple origins. Ultimately, organic materials can inform biological studies by providing an excellent testing ground to study quantum effects and their relevance to functional performance. Meanwhile, biological systems can inspire the next generation of advanced materials and devices, based on cheap, renewable components.

By the 22nd century, physics and biology could be indistinguishable.

References

1. Venter, C., Cohen, D.: The century of biology. New Perspect. Q. **21**, 73 (2004)
2. Chin, A., Prior, J., Rosenbach, R., Caycedo-Soler, F., Huelga, S., Plenio, M.: The role of non-equilibrium vibrational structures in electronic coherence and recoherence in pigment-protein complexes. Nat. Phys. **9**, 113–118 (2013)
3. Weiss, U.: Quantum Dissipative Systems. World Scientific (2012)
4. Schlau-Cohen, G., Ishizaki, A., Fleming, G.: Two-dimensional electronic spectroscopy and photosynthesis: fundamentals and applications to photosynthetic light-harvesting. Chem. Phys. **386**, 1–22 (2011)
5. Engel, G., Calhourn, T., Read, E., Ahn, T.-K., Mancal, T., Cheng, Y.-C., Blankenship, R., Fleming, G.: Evidence for wavelike energy transfer through quantum coherence in photosynthetic systems. Nature **446**, 782–786 (2007)
6. Collini, E., Wong, C., Wilk, K., Curmi, P., Brumer, P., Scholes, G.: Coherently wired light-harvesting in photosynthetic marine algae at ambient temperature. Nature **463**, 644–647 (2010)
7. Lewis, K., Ogilvie, J.: Probing photosynthetic energy and charge transfer with two-dimensional electronic spectroscopy. J. Phys. Chem. Lett. **3**, 503–510 (2012)

8. Mohseni, M., Omar, Y., Engel, G.S., Plenio, M.B.: Quantum Effects in Biology. Cambridge University Press (2014)
9. Blankenship, R.: Molecular Mechanisms of Photosynthesis, 2nd edn. Wiley-Blackwell, (2014)
10. Westenhoff, S., Palecek, D., Edlund, P., Smith, P., Zigmantas, D.: Coherent picosecond exciton dynamics in a photosynthetic reaction center. J. Am. Chem. Soc. **134**, 16484–16487 (2012)
11. Romero, E., Augulis, R., Novoderezhkin, V.I., Ferretti, M., Thieme, J., Zigmantas, D., van Grondelle, R.: Quantum coherence in photosynthesis for efficient solar-energy conversion. Nat. Phys. **10**, 676–682 (2014)
12. Fuller, F.D., Pan, J., Gelzinis, A., Butkus, V., Senlik, S.S., Wilcox, D.E., Yocum, C.F., Valkunas, L., Abramavicius, D., Ogilvie, J.P.: Vibronic coherence in oxygenic photosynthesis. Nat. Chem. **6**, 706–711 (2014)
13. Christensson, N., Kauffmann, H.F., Pullerits, T., Mančal, T.: Origin of long-lived coherences in light-harvesting complexes. J. Phys. Chem. B **116**, 7449–7454 (2012)
14. Tiwari, V., Peters, W.K., Jonas, D.M.: Electronic resonance with anticorrelated pigment vibrations drives photosynthetic energy transfer outside the adiabatic framework. Proc. Natl. Acad. Sci. **110**, 1203–1208 (2013)
15. Butkus, V., Zigmantas, D., Abramavicius, D., Valkunas, L.: Distinctive character of electronic and vibrational coherences in disordered molecular aggregates. Chem. Phys. Lett. **587**, 93–98 (2013)
16. Kolli, A.: O Reilly, E. J., Scholes, G. D. & Olaya-Castro, A. The fundamental role of quantized vibrations in coherent light harvesting by cryptophyte algae. J. Chem. Phys. **137**, 174109 (2012)
17. Bakulin, A.A., Morgan, S.E., Kehoe, T.B., Wilson, M.W.B., Chin, A.W., Zigmantas, D., Egorova, D., Rao, A.: Real-time observation of multiexcitonic states in ultrafast singlet fission using coherent 2D electronic spectroscopy. Nat. Chem. **8**, 16–23 (2016)
18. Smith, M.B., Michl, J.: Singlet fission. Chem. Rev. **110**, 6891–6936 (2010)
19. Shockley, W., Queisser, H.J.: Detailed balance limit of efficiency of p-n junction solar cells. J. Appl. Phys. **32**, 510–519 (1961)
20. Fassioli, F., Nazir, A., Olaya-Castro, A.: Quantum state tuning of energy transfer in a correlated environment. J. Phys. Chem. Lett. **1**, 2139–2143 (2010)
21. Prior, J., Castro, E., Chin, A.W., Almeida, J., Huelga, S.F., Plenio, M.B.: Wavelet analysis of molecular dynamics: efficient extraction of time-frequency information in ultrafast optical processes. J. Chem. Phys. **139**, 224103 (2013)
22. Ishizaki, A., Calhoun, T.R., Schlau-Cohen, G.S., Fleming, G.R.: Quantum coherence and its interplay with protein environments in photosynthetic electronic energy transfer. Phys. Chem. Chem. Phys. **12**, 7319–7337 (2010)
23. O Reilly, E.J., Olaya-Castro, A.: Non-classicality of the molecular vibrations assisting exciton energy transfer at room temperature. Nat. Commun. **5**, 3012 (2014)
24. Vos, M.H., Rappaport, F., Lambry, J.-C., Breton, J., Martin, J.-L.: Visualization of coherent nuclear motion in a membrane protein by femtosecond spectroscopy. Nature **363**, 320–325 (1993)
25. Fuglebakk, E., Tiwari, S.P., Reuter, N.: Comparing the intrinsic dynamics of multiple protein structures using elastic network models. Biochim. Biophys. Acta **1850**, 911–922 (2015)
26. Juanico, B., Sanejouand, Y., Piazza, F., Rios, P.D.L.: Discrete breathers in nonlinear network models of proteins. Phys. Rev. Lett. **99**, 238104 (2007)
27. Cole, D.J., Chin, A.W., Hine, N.D.M., Haynes, P.D., Payne, M.C.: Toward ab initio optical spectroscopy of the Fenna-Matthews-Olson complex. J. Phys. Chem. Lett. **4**, 4206–4212 (2013)

Chapter 2
Methods

The history of scientific enquiry from the earliest times to the present day might be neatly summarized into three questions: what is the nature of light itself, of matter itself, and of the interaction agent?

John Weiner and Frederico Nunes [1]

The aim of this chapter is to build a toolbox of methods which can give insight into the functional mechanisms of both organic and biological systems. I will begin by reviewing some key ideas from solid state physics and the theory of open quantum systems. These approaches have a long history in the literature and provide a solid basis on which to build new methods for organic and biological systems. I will then introduce the recently developed experimental technique of 2D electronic spectroscopy, which can provide crucial information concerning ultrafast quantum and vibrational dynamics. Nonetheless, 2D spectroscopy results are difficult to interpret and I will discuss approaches to untangling the complex information contained in 2D spectra.

2.1 Excitonic Models

If a molecule absorbs a quantum of energy corresponding to a transition between two molecular orbitals, an electron can be transferred from the highest occupied molecular orbital (the HOMO) to the lowest unoccupied molecular orbital (the LUMO). This process leaves a hole in the HOMO and is illustrated in Fig. 2.1. The resulting bound electron-hole pair is known as an 'exciton' [2].

In a molecular dimer, interactions between the molecules cause the exciton to delocalise across both molecules. Note that the interactions between molecules which lead to excitons are often electrostatic [3]. In order to write down the interaction between two molecules, we consider their charge distributions, $\rho_1(\vec{r})$ and $\rho_2(\vec{r})$ and define the charge of molecule i as:

S.E. Morgan, *Ultrafast Quantum Effects and Vibrational Dynamics in Organic and Biological Systems*, Springer Theses, DOI 10.1007/978-3-319-63399-2_2

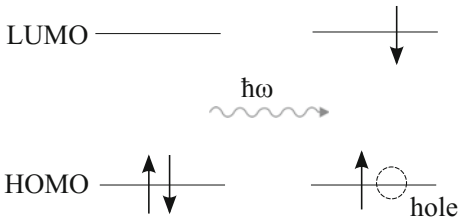

Fig. 2.1 Sketch of HOMO-LUMO transition: when energy is absorbed, an electron is transferred from the HOMO to the LUMO

$$q_i = \int d\vec{r}\,\rho_i(\vec{r}) \tag{2.1}$$

and its dipole moment as:

$$\vec{\mu}_i = \int d\vec{r}\,\rho_i(\vec{r})(\vec{r} - \vec{r}_i) \tag{2.2}$$

(the concept of dipole moment will be discussed in detail in Sect. 2.3.2).
Then the Coulomb interaction can be expanded in the multipole expansion [3]:

$$J_{12} = \frac{1}{4\pi\varepsilon}\left[\frac{q_1 q_2}{R} + \frac{q_1(\vec{\mu}_2 \cdot \hat{R}) - q_2(\vec{\mu}_1 \cdot \hat{R})}{R^2} + \frac{\vec{\mu}_1 \cdot \vec{\mu}_2 - 3(\vec{\mu}_1 \cdot \hat{R})(\vec{\mu}_2 \cdot \hat{R})}{R^3} + \ldots\right] \tag{2.3}$$

Here, $\vec{R} = \vec{r}_2 - \vec{r}_1$ where $\vec{r}_{1,2}$ is the position vector of molecule 1 or 2 and ε is the permittivity. In order for this expansion to be valid, the distance between molecules, R, must be larger than the charge distributions of individual molecules. Note that if the molecules are uncharged the third order term (the dipole-dipole interaction) dominates over the first and second order terms.

These molecular interactions mix the original states to form new states, which are superpositions of the original states. Formally, if the two molecules are identical and the excitation is initially on molecule 1: $\phi_1^*\phi_2$, or on molecule 2: $\phi_1\phi_2^*$, the new states become the superpositions $1/\sqrt{2}(\phi_1^*\phi_2 \pm \phi_1\phi_2^*)$, as shown in Fig. 2.2a [2]. In general, the degree of delocalisation of the excitons depends on the original site energies and couplings. Crucially, the mixing alters the energy spectrum of the system. In particular, the energies of the two new states become split (by an energy difference equal to twice the interaction between the molecules if they are identical). This effect is known as 'Davydov splitting' [4]. In order to calculate the effects of the new energy spectrum on the material's photophysics, the transition dipole moments of the new states can be written in terms of the original transition dipole moments [5]:

$$\vec{\mu}_{\alpha 0} = \sum_i V_{\alpha i}^{-1}\vec{\mu}_{i0} \tag{2.4}$$

Here, $\vec{\mu}_{i0}$ is the transition dipole moment of the original site i from the ground state (0), whilst $\vec{\mu}_{\alpha 0}$ is the transition dipole moment of the eigenstate α from the ground

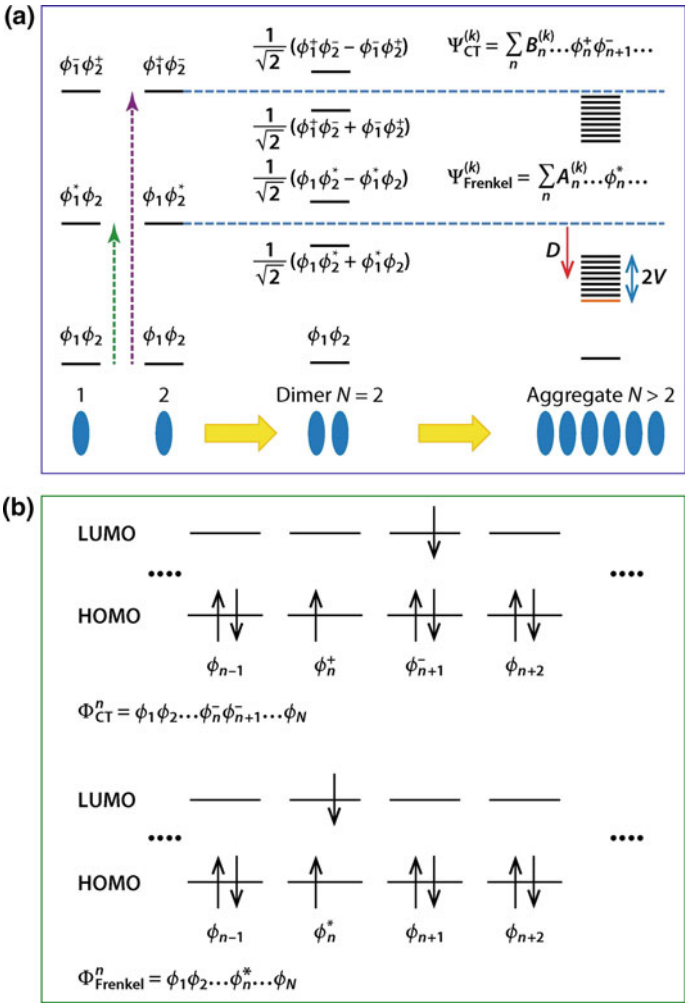

Fig. 2.2 Sketches of the energy spectrum and HOMO and LUMO bands in Frenkel and charge transfer excitons. **a** As isolated molecules are brought closer to each other to form a dimer, they begin to interact and their energy levels split. In an aggregate, a band of states forms. **b** The HOMO and LUMO in a Frenkel exciton (*lower panel*), showing the electron and hole on the same molecule. In a charge transfer exciton (*upper panel*), the electron and hole are on adjacent molecules. Figure adapted from [2]

state. V is the operator which diagonalises the site Hamiltonian (which is defined by the individual molecules' energies and couplings) in order to obtain the excitonic Hamiltonian:

$$H_{\text{exciton}} \equiv V^{-1} H_{\text{site}} V \tag{2.5}$$

In a molecular aggregate the exciton becomes delocalised across multiple molecules, leading to a band of exciton states. This was first shown by Frenkel in the 1930s [6, 7] and this type of exciton is therefore known as a Frenkel exciton. Crucially, the electron and hole remain localised on the same molecule, as shown in Fig. 2.2b (lower panel). This type of exciton is often observed in organic and biological molecules and we will use it extensively in the following chapters. Note that excitons can also be classified as either singlet or triplet excitons, depending on the spin state of the electrons involved [2]. For example, if the electrons in the lower and upper states have opposite spins, as in the bottom panel of Fig. 2.2b and precess out of phase with each other, they are in an overall spin singlet state, $S = 0$. If they precess in phase or have the same spin orientations, the spin state is triplet, $S = 1$. Triplet excitons are stabilised with respect to singlets by the exchange energy (due to reduced electron-electron repulsions). However they are optically dark and the singlet to triplet transition is normally a slow process in molecules without heavy atoms because it requires spin-orbit coupling.

Whilst in Frenkel excitons the electron and hole are always localised on the same molecule, in other types of exciton they may lie further apart. For example, in charge transfer (CT) excitons the electron and the hole are localised on adjacent molecules, as shown in Fig. 2.2b (upper panel). Similar to Frenkel states, in molecular dimers and aggregates molecular interactions cause charge transfer states to mix and form new superposition states. Note that Frenkel and CT states can also mix (and this is the origin of the singlet-multiexciton state coupling in pentacene which will be discussed in Chap. 3).

For completeness, in Wannier-Mott excitons the electron and hole are separated by much larger distances (typically $\approx$100 Å) and are only loosely bound [8, 9]. This concept is useful in inorganic semiconductors, where large dielectric constants mean that electric field screening reduces the interaction between the hole and the electron. However, organic materials have much smaller dielectric constants, hence here we will only be concerned with Frenkel and charge-transfer excitons [2].

2.2 Energy Transfer and Dissipation

No physical system is completely isolated from its surroundings. In organic and biological systems there are normally a large number of vibrations including solvent modes, intramolecular vibrations, phonons and electromagnetic modes, which all contribute towards the environment. Over time, interactions between the system and its environment lead to decoherence.

In order to treat energy transfer in organic and biological systems, we need to take account of the environment. There are different approaches to doing this, which are valid in different regimes. Förster resonance energy transfer (FRET) is often used in the localised limit, where the coupling between molecules is weak and can be treated as a perturbation. Here, energy transfer occurs between molecules when there is a resonance between the energy gaps of the donor and acceptor states. The

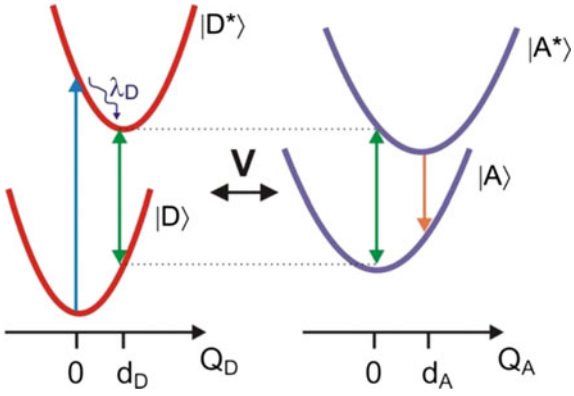

Fig. 2.3 Förster resonance energy transfer: The donor absorbs light, leading to an excited state, $|D^*\rangle$. The donor then relaxes, dissipating its reorganisation energy, λ_D. This creates a resonance between the energy gaps of the donor and acceptor, shown in green. Energy transfer to the acceptor (due to a dipole-dipole interaction) is then followed by further relaxation. Figure taken from [11]

energy transfer process is illustrated in Fig. 2.3 and scales as r^{-6}, where r is the intermolecular distance [10].

An excited donor may also transfer energy to an acceptor state via electron exchange, in a process known as Dexter energy transfer [12]. Unlike in FRET, in Dexter energy transfer the reaction rate decays exponentially with the distance between the donor and acceptor, hence this process is only important at short distances (normally within 10 Å) [13]. Dexter energy transfer is illustrated in Fig. 2.4, alongside FRET for comparison. As shown in the figure, both singlet-singlet and triplet-triplet Dexter energy transfer are possible and this type of interaction can also lead to triplet-triplet annihilation. In the latter case, two triplet excitations recombine to form a singlet excitation in a manner which is essentially the reverse of the singlet fission process which will be discussed in Chap. 3.

However, when molecules are close together, coupling between them may be strong and Förster theory is no longer valid. For example, this is true for the pigment protein complexes which carry out photosynthesis and will be discussed in detail in Chap. 4. Collective excitations between pigments are known as excitons, as discussed in the previous section, and an exciton coupling theory is required. Below, we describe how energy dissipation is taken into account in this case using one such theory, known as Bloch-Redfield theory. In Bloch-Redfield theory, instead of assuming that the coupling between molecules is weak, we assume that the coupling between the system and the environment is weak.

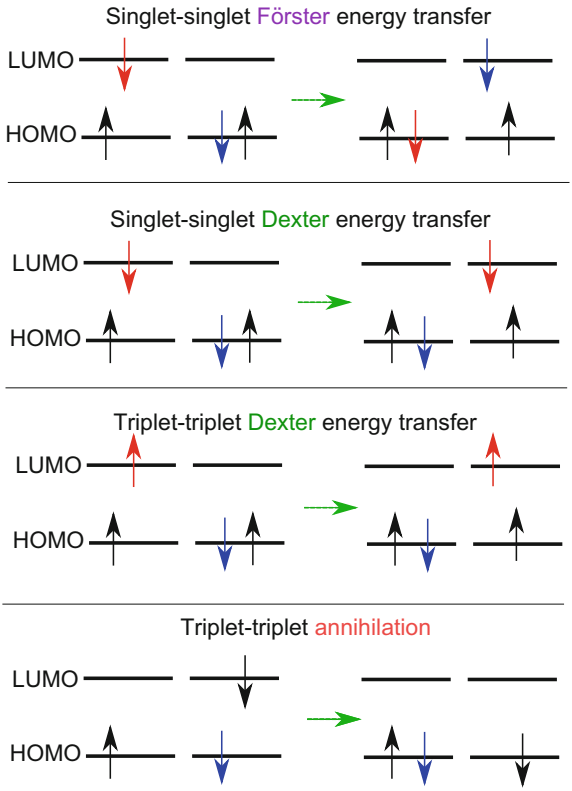

Fig. 2.4 Excitations in Dexter and Förster resonance energy transfer. Figure adapted from figures by Che-Wei Chang, taken from [14]

2.2.1 Description of the Bath

In order to treat dissipation, we first need to define our system and its environment. Here we consider the general case, where H is the Hamiltonian of a system with a number of states, indexed by i. Couplings, J, exist between the states (which might arise from electrostatic interactions, for example). The Hamiltonian can therefore be written as:

$$H = \sum_i \varepsilon_i \left|i\right\rangle \left\langle i\right| + \sum_{i \neq j} J_{ij} \left|i\right\rangle \left\langle j\right| \tag{2.6}$$

where ε_i is the energy of state i. We place this system in a bath of k harmonic oscillators, with frequencies ω_k, described by the bosonic annihilation and creation operators b_k and $b_k^\dagger$. The bath Hamiltonian takes the form:

$$H_B = \sum_k \omega_k b_k^\dagger b_k \tag{2.7}$$

where we have set the reduced Planck constant $\hbar = 1$. The sites interact with the bath, leading to decoherence over time. We assume that the interaction of the sites with the bath is linear, as follows:

$$H_{IB} = \sum_{i,k} g_{ik}|i\rangle\langle i|(b_{ik} + b_{ik}^{\dagger}) \tag{2.8}$$

Here g_{ik} are constants describing the coupling between the sites and the bath modes. These couplings are often difficult to determine experimentally and an alternative approach is to use the spectral function, defined by [15]:

$$J_s(\omega) = \sum_k g_k^2 \delta(\omega - \omega_k) \tag{2.9}$$

The form of the spectral function can be chosen depending on the problem at hand. One possible choice for irreversible relaxation is the over-damped Brownian oscillator spectral function, given by [16]:

$$J_s(\omega) = 2\lambda \frac{\omega\gamma}{\omega^2 + \gamma^2} \tag{2.10}$$

(here we assume that all sites have the same coupling to the bath). γ sets the dynamical response time of the bath. The reorganization energy of the bath, λ, is a measure of the strength of the coupling of the sites to the bath. This defines g in Eq. 2.8.

Overall, the total Hamiltonian for the system, the bath and the coupling between the system and the bath is given by:

$$H_{\text{total}} = H + H_B + H_{IB} \tag{2.11}$$

2.2.2 Bloch-Redfield Theory

As discussed above, Bloch-Redfield theory can be used to model the dissipation of energy over time. Here I present an overview of Bloch-Redfield theory, which follows that given in Blum [17]. I use the reduced density matrix and the interaction picture, which are described in more detail in appendices A and B respectively.

I start by writing the time evolution of the reduced density matrix in the interaction picture with respect to H_{total} (see Appendix B):

$$\dot{\rho}(t)_{SI} = -(i/\hbar)\text{Tr}_B[V(t)_I, \rho(0)_I] - (1/\hbar)^2 \int_0^t dt' \text{Tr}_B[V(t)_I, [V(t')_I, \rho(t')_I]] \tag{2.12}$$

where Tr_B represents taking the trace over the bath degrees of freedom, ρ_I is the density matrix in the interaction picture and ρ_{SI} is the reduced density matrix in

the interaction picture. $V(t)_I$ is the interaction term in the interaction picture, which describes the interaction between the system and the bath. Note that V(t) is given by H_{IB} in Eq. 2.11, which was defined in Eq. 2.8.

Bloch-Redfield theory makes two main approximations, which introduce irreversibility into the system, allowing energy to be dissipated. The first approximation is that while the bath changes the state of the system over time, the bath itself remains unchanged, hence the density matrix can be written as:

$$\rho(t)_I = \rho(t)_{SI}\rho(0)_B \tag{2.13}$$

where $\rho(0)_B$ represents the state of the bath, which is unchanged over time and is given by a Boltzmann distribution:

$$\rho(0)_B = \exp(-\beta H_B)/Z \tag{2.14}$$

Here Z is the partition function and $\beta = 1/(k_B T)$, where T is temperature. The second approximation is the Markov approximation, which states that the system has no memory of its past, i.e. $\dot{\rho}(t)_{SI}$ only depends on $\rho(t)$ and not on ρ at earlier times. Therefore in Eq. 2.12 we replace $\rho(t')_{SI}$ with $\rho(t)_{SI}$. Under these two approximations, we obtain:

$$\dot{\rho}(t)_{SI} = -(i/\hbar)Tr_B[V(t)_I, \rho(0)_S\rho(0)_B] - (1/\hbar)^2 \int_0^t dt' Tr_B[V(t)_I, [V(t')_I, \rho(t)_{SI}\rho(0)_B]] \tag{2.15}$$

We now split the interaction operator into operators which act on the system only, Q_i, and on the bath only, F_i:

$$V(t)_I = \sum_i F(t)_i Q(t)_i \tag{2.16}$$

with:

$$F(t)_i = \exp(iH_B t/\hbar)F_i \exp(-iH_B t/\hbar) \tag{2.17}$$

and

$$Q(t)_i = \exp(iHt/\hbar)Q_i \exp(-iHt/\hbar) \tag{2.18}$$

From comparison to Eq. 2.8, in our case:

$$Q_i = |i\rangle\langle i| \tag{2.19}$$

and

$$F_i = \sum_k g_{ik}\left(b_k + b_k^\dagger\right). \tag{2.20}$$

Using these expressions and the substitution $t'' = t - t'$, we can rewrite Eq. 2.15 as:

$$\dot{\rho}(t)_{SI} = -(1/\hbar)^2 \sum_{ij} \int_0^\infty dt'' [Q(t)_i, Q(t-t'')_j \rho(t)_{SI}] \left\langle F(t'')_i F_j \right\rangle - [Q(t)_i, \rho(t)_{SI} Q(t-t'')_j] \left\langle F_j F(t'')_i \right\rangle \quad (2.21)$$

Here, $\left\langle F(t'')_i F_j \right\rangle$ and $\left\langle F_j F(t'')_i \right\rangle$ are time correlation functions, which quantify the correlation between the state of the bath at different times. They can be expressed using the density matrix as:

$$\langle F(t)_i F(t')_j \rangle = \mathrm{Tr}_B (F(t)_i F(t')_j \rho(0)_B) \quad (2.22)$$

A final approximation, known as the secular approximation, can also be made. In this approximation, we average over terms which vary rapidly (compared to the relaxation time of the system). This approximation is popular because it guarantees that the diagonal elements of the density matrix are non-negative, which is not always the case for the density matrix obtained directly from the equations above [17]. It also enables more efficient numerical calculations, since the populations and coherences are no longer coupled. However, this loss of some of the interactions between the system and its environment is not always valid and can lead to inaccurate results [18–20].

If we apply the secular approximation, we obtain:

$$\left\langle m' \right| \dot{\rho}(t)_{SI} \left| m \right\rangle = \delta_{m'm} \sum_{n \neq m} \langle n| \rho(t)_{SI} |n\rangle W_{mn} - \gamma_{m'm} \left\langle m' \right| \rho(t)_{SI} \left| m \right\rangle \quad (2.23)$$

This is the Master equation, which is an equation of motion for the reduced density matrix, describing the irreversible behaviour of the system. Here, m are eigenstates of the system's Hamiltonian, H, (given by Eq. 2.6) and we have introduced the quantities:

$$W_{mn} = \Gamma^+_{nmmn} + \Gamma^-_{nmmn} \quad (2.24)$$

$$\gamma_{m'm} = \sum_k (\Gamma^+_{m'kkm'} + \Gamma^-_{mkkm}) - \Gamma^+_{mmm'm'} - \Gamma^-_{mmm'm'} \quad (2.25)$$

$$\Gamma^+_{mkln} = (1/\hbar)^2 \sum_{ij} \langle m| Q_i |k\rangle \langle l| Q_j |n\rangle \int_0^\infty dt'' \exp(-i\omega_{ln} t'') \left\langle F(t'')_i F_j \right\rangle \quad (2.26)$$

$$\Gamma^-_{mkln} = (1/\hbar)^2 \sum_{ij} \langle m| Q_j |k\rangle \langle l| Q_i |n\rangle \int_0^\infty dt'' \exp(-i\omega_{mk} t'') \left\langle F_j F(t'')_i \right\rangle \quad (2.27)$$

and

$$\omega_{mn} = (E_m - E_n)/\hbar \quad (2.28)$$

In order to understand the implications of the Master equation (Eq. 2.23), it is helpful to consider the rate of change of the diagonal and off-diagonal elements of the density matrix separately. From Eq. 2.23, the diagonal elements obey the equation:

$$\dot{\rho}(t)_{mm} = \sum_{n \neq m} \rho(t)_{nn} W_{mn} - \rho(t)_{mm} \sum_{n \neq m} W_{nm} \tag{2.29}$$

The diagonal elements, $\rho_{mm}(t)$, give the probability of state m being occupied as a function of time. This probability increases due to transitions from all other states (labelled as states n) to state m. The rate of change of $\rho_{mm}(t)$ due to these transitions is given by the population in each state n multiplied by the transition rate from state n to state m. Hence W_{mn} in Eq. 2.29 is interpreted as the transition rate from n to m. Similarly, $\rho_{mm}(t)$ decreases due to transitions from state m to other states and this leads to the second (negative) term in Eq. 2.29. The relaxation time of state m, T_1, is given by the inverse of the sum of the transition rates from m to all other states [11]:

$$T_{1m} = \frac{1}{\sum_{n \neq m} W_{nm}} \tag{2.30}$$

The rates W_{mn} are given by Eq. 2.24 in terms of the rates Γ^{+}_{nmmn} and Γ^{-}_{nmmn}, which include information about the bath obtained from the time correlation functions of the bath operators, $\langle F(t'')_i F_j \rangle$ and $\langle F_j F(t'')_i \rangle$. F_i depends on g_k, according to Eq. 2.20, and g_k determines the spectral density function, $J_s(\omega)$, as seen from Eq. 2.9. Hence we can also write the rates W_{mn} in terms of the spectral density function, $J_s(\omega)$. Putting everything together, we obtain:

$$W_{mn} = \begin{cases} 2\pi \left|V_{mn}\right|^2 J\left(E_m - E_n\right)\left[n\left(E_m - E_n\right) + 1\right] & \text{for } E_m > E_n \\ 2\pi \left|V_{mn}\right|^2 J\left(E_n - E_m\right) n\left(E_n - E_m\right) & \text{for } E_m < E_n \end{cases}$$

where $\left|V_{mn}\right|^2 = \sum_i \left|\langle e_m | i \rangle \langle i | e_n \rangle\right|^2$. Meanwhile, the factor $n(\omega) = \left(e^{\omega / k_B T} - 1\right)^{-1}$ ensures that if $E_n > E_m$, the transition rate from n to m is greater than the rate from m to n so that at equilibrium the population probabilities are given by a Boltzmann distribution.

It is also instructive to consider the off-diagonal density matrix elements, $\rho_{mn}(t)$. From Eq. 2.23, we have:

$$\langle m | \dot{\rho}(t)_{SI} | n \rangle = \left[\Gamma^{+}_{nnmm} + \Gamma^{-}_{nnmm} - \Gamma^{+}_{mmmm} - \Gamma^{-}_{nnnn} - \sum_{k \neq m} \Gamma^{+}_{mkkm} - \sum_{k \neq n} \Gamma^{-}_{nkkn} \right] \langle m | \rho(t)_{SI} | n \rangle \tag{2.31}$$

If we take the real part of the last two terms in Eq. 2.31, the expression we obtain looks very similar to the equation obeyed by the diagonal population elements, Eq. 2.29 [11]:

$$\mathrm{Re}\left(\sum_{k\neq m}\Gamma^{+}_{mkkm}+\sum_{k\neq n}\Gamma^{-}_{nkkn}\right)=\frac{1}{2}\sum_{k\neq m}W_{km}+\frac{1}{2}\sum_{k\neq n}W_{kn}$$
$$=\frac{1}{2}\left(\frac{1}{T_{1m}}+\frac{1}{T_{1n}}\right) \tag{2.32}$$

The only difference from Eq. 2.29 is the factor of $\frac{1}{2}$, which means that the off-diagonal coherences decay at half the rate of the population decay. Meanwhile, the real part of the first four terms in Eq. 2.31 can be written as:

$$\mathrm{Re}\left(\Gamma^{+}_{mmnn}+\Gamma^{-}_{mmnn}-\Gamma^{+}_{mmmm}-\Gamma^{-}_{nnnn}\right)=\int_0^\infty dt''\left\langle\left[V_{nn}(t'')-V_{mm}(t'')\right]\left[V_{nn}(0)-V_{mm}(0)\right]\right\rangle_B$$
$$=\int_0^\infty dt''\left\langle\Delta V(t'')\Delta V(0)\right\rangle_B$$
$$=\frac{1}{T_2^*} \tag{2.33}$$

This term involves a correlation function which accounts for fluctuations in the energy gap between the states m and n. These fluctuations are caused by the energy gap interacting with the bath in a phenomenon known as 'pure dephasing'. The timescale for pure dephasing is conventionally called T_2^*.

Overall, the dephasing time for the coherences has two contributions; one from the relaxation of the states involved and one from the pure dephasing. It can be written as:

$$\frac{1}{T_2}=\frac{1}{T_2^*}+\frac{1}{2}\left(\frac{1}{T_{1m}}+\frac{1}{T_{1n}}\right) \tag{2.34}$$

As an illustration, we consider the two level system illustrated in Fig. 2.5, with an energy difference of 500 cm^{-1} and coupling of J = 100 cm^{-1} between the two states. The states are coupled to a bath, which is described by an over-damped Brownian oscillator spectral function as given in Eq. 2.10. We set $\gamma_j = 900\ \mathrm{cm}^{-1}$ and $\lambda_j = 35\ \mathrm{cm}^{-1}$ and choose the total population on the highest energy site as the initial condition. In Fig. 2.5, we plot the populations of the two eigenstates, which tend to a Boltzmann distribution at long times (the temperature is set to 300K). We also plot the evolution of the site populations, which oscillate due to the non-zero coherences between the two states. Also notice that the populations decay at twice the rate at which the coherences decay, as expected.

The Bloch-Redfield theory described in this section has been used extensively to model energy transfer in photosynthetic pigment protein complexes [21–23] and in Chap. 3 we will also take this approach to model dissipation in thin films of the organic molecule pentacene. Both of these systems exhibit strong interactions between molecules, hence these problems are well suited to the excitonic framework of Redfield theory (as opposed to Förster theory). Note that in Redfield theory we

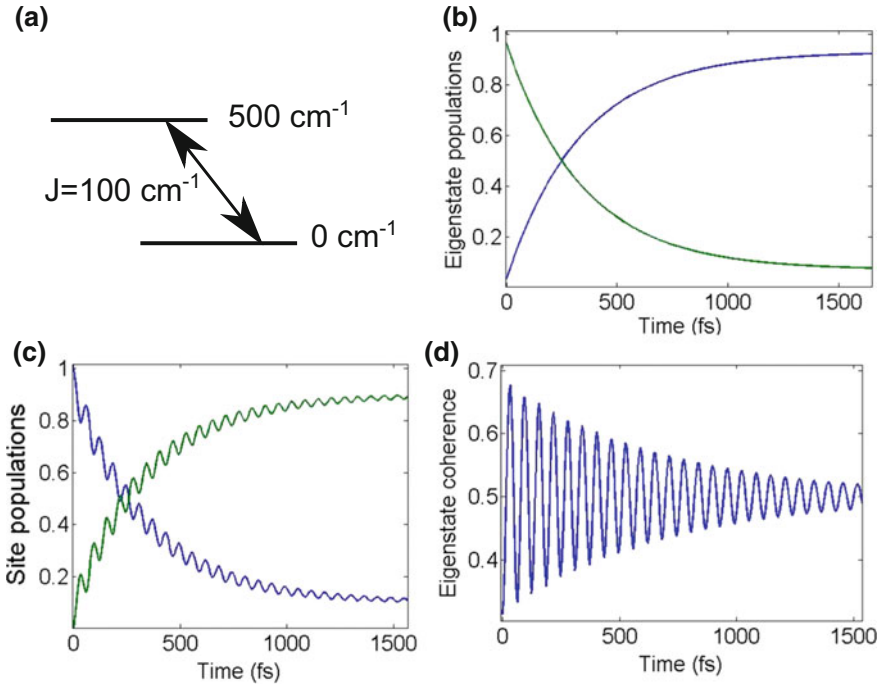

Fig. 2.5 Dynamics for a two level system with Bloch-Redfield dissipation. **a** Two level system. **b** Eigenstate populations as a function of time. **c** Site populations. **d** Coherence between the two eigenstates

assume that the coupling between the system and the bath is weak, which may not always be valid in these systems. One approach to circumventing this problem is to include certain strong vibrational modes in the system itself.

2.3 2D Electronic Spectroscopy

2D Fourier transform spectroscopy was originally applied to nuclear magnetic resonance (NMR) research, where it has proved invaluable in obtaining high resolution structures of complicated molecules. Following this success, 2D spectroscopy was extended to the optical regime in the late 1990s [24] and named 2D electronic or optical spectroscopy. 2D electronic spectroscopy (2DES) employs ultrafast laser pulses and is therefore able to interrogate biological and organic systems at the femtosecond and picosecond timescales on which many molecular processes occur. In conventional 1D spectroscopy the underlying structural and dynamical information is all projected onto a single time or frequency axis, giving congested spectra. By using

2DES, this information can be separated, allowing much greater insight into the system's electronic and vibrational degrees of freedom.

Here, I outline 2DES; much of this discussion is based on work by Mukamel [25] and Fleming [5] (see also Tokmakoff [11] and Hamm [26]). I begin by describing the experimental setup, before examining the underlying theory. 2DES is an example of third order nonlinear spectroscopy, which is the most popular class of nonlinear spectroscopic techniques and also includes transient absorption, photon echo and transient grating experiments. In all of these methods, the signals are determined by the third order polarisation, which I will show how to obtain using nonlinear response formalism. I then introduce the excitonic picture which describes organic and biological systems and explain how Feynman diagrams can be used to understand 2DES signals within this framework. Finally I briefly discuss some of the challenges involved in distinguishing different signals in 2DES spectra.

2.3.1 Experimental Setup

The 2DES experimental setup is shown in Fig. 2.6. There are three incident laser pulses and a signal pulse, centered at times t_1, t_2, t_3 and t_S respectively. The ultrafast pulses employed often have durations of less than 20 fs, leading to broadband excitation. In between the four pulses there are three time periods: the coherence time τ, the waiting time, T, and the detection time, t_d (see Fig. 2.7). Note that the waiting time is sometimes referred to as the population or evolution time in the literature, whilst the detection time is also called the rephasing time.

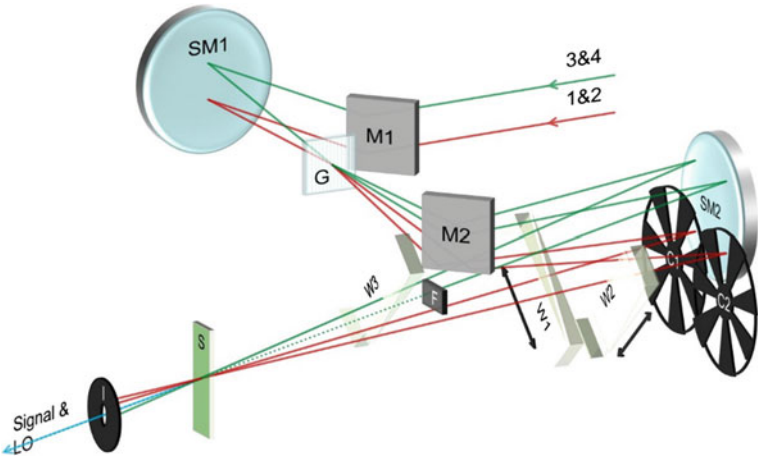

Fig. 2.6 2D spectroscopy experimental setup [27]

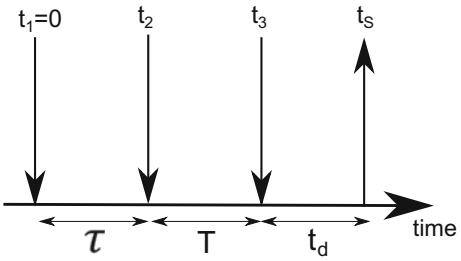

Fig. 2.7 Time intervals in third order non-linear spectroscopy

Spectral interference between the signal and a local oscillator pulse is recorded using a spectrometer, which performs a Fourier transform across the detection time. During the experiments, the coherence time is scanned incrementally (often in steps as short as 2 fs). A major challenge in 2DES is maintaining phase stability between pulses 1 and 2 during the coherence time and between pulse 3 and the local oscillator [28]. Full details of the experimental setup can be found in the literature, see for example [24, 28, 29].

2.3.2 Theory Behind 2D Electronic Spectroscopy

Spectroscopy is the study of the interaction between light and matter. Light is an example of an electromagnetic wave, which interacts with matter due to its electric field. When the electric field is incident on a material it becomes polarised, creating an induced dipole moment which depends on the particles' charges (q) and their displacements ($\vec{r}$):

$$\vec{\mu}_{ind} = q\vec{r} \tag{2.35}$$

If the frequency of the optical field is in resonance with a transition between two states of the material then energy can be exchanged between the optical field and the material and light is absorbed or emitted. The electric dipole moment associated with the transition between two states is known as the transition dipole moment. Its direction depends on the polarisation of the transition, whilst its magnitude depends on the material's charge distribution. The transition dipole moment between states ϕ_a and ϕ_b is an intrinsically quantum property of the material and can be written in Dirac notation as:

$$\vec{\mu}_{ab} = \langle\phi_a| \sum_i q_i \vec{r}_i \, |\phi_b\rangle \tag{2.36}$$

The macroscopic equivalent of the dipole moment is the polarisation, which is defined as a collective dipole moment per unit volume. The polarisation is created by the incident electric fields interacting with the material and it then emits a signal electric field (see Fig. 2.8). With i particles situated at $\vec{r}_i$, the polarisation is given by

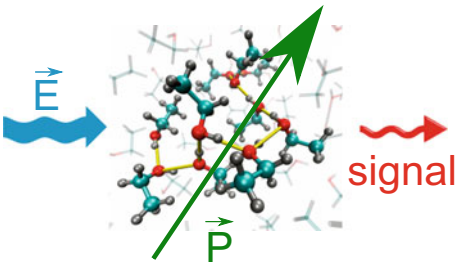

Fig. 2.8 An incident electric field polarises a material, creating a signal. Image of molecules adapted from [30]

[11]:

$$\vec{P}(\vec{r}) = \sum_i \vec{\mu}_i \delta(\vec{r} - \vec{r}_i) \tag{2.37}$$

where δ is the Dirac delta function. The polarisation is related to the electric field, $\vec{E}$, via the susceptibility, χ [26]. In weak electric fields, this relationship is linear:

$$\vec{P} = \varepsilon_0 \chi \vec{E} \tag{2.38}$$

where ε_0 is the permittivity of free space. However, when there are either several fields (as is the case in 2DES) or very strong fields, the polarisation depends nonlinearly on the electric field. Therefore we expand the polarisation as a power series with respect to $\vec{E}$:

$$\vec{P} = \varepsilon_0 \left(\chi^{(1)} \vec{E} + \chi^{(2)} \vec{E}^{(2)} + \chi^{(3)} \vec{E}^{(3)} + \cdots \right) \tag{2.39}$$

Note that even order susceptibilities vanish in materials with inversion symmetry (including isotropic media), hence the third order term is normally the lowest order nonlinear signal [26]. For nth order nonlinear spectroscopy we require the nth order polarisation, $\vec{P}^{(n)} = \varepsilon_0 \chi^{(n)} \vec{E}^{(n)}$, to calculate the signal. This can be calculated from the nth order density matrix, $\rho^{(n)}(t)$ [25]:

$$\vec{P}^{(n)}(t) = \mathrm{Tr}(\vec{\mu} \rho^{(n)}(t)) \tag{2.40}$$

To calculate $\rho^{(n)}(t)$, we take a semi-classical approach where the material part of the Hamiltonian, H_0, is treated quantum mechanically, whilst the electromagnetic field, V(t), is treated classically [25]. The total Hamiltonian is:

$$H = H_0 + V(t) \tag{2.41}$$

In the electric dipole approximation, the wavelength of the electromagnetic radiation is assumed to be much larger than the size of the molecules [11]. Then V(t) describes the interaction between the electric field and the transition dipole moment:

$$V(t) = -\vec{E}(t) \cdot \vec{\mu} \tag{2.42}$$

If the external electric field is weak compared to the internal electric fields, we can treat V(t) as a perturbation to the system. It is then convenient to work in the interaction picture, in which the density matrix is given by $\rho(t)_I = U_0^\dagger(t)\rho(t)U_0(t)$ (for further information concerning the interaction picture see appendix B). Here the time evolution operator $U_0(t) = e^{-(i/\hbar)H_0 t}$. The density matrix obeys the Liouville equation:

$$i\hbar\frac{\partial\rho(t)_I}{\partial t} = [V(t)_I, \rho(t)_I] \tag{2.43}$$

Following Hamm [26], we take a perturbative expansion in powers of the weak interaction V(t). We then return to the Schrödinger picture and substitute Eq. 2.42 to obtain:

$$\rho^{(n)}(t) = (-i/\hbar)^n \int_{-\infty}^{t} d\tau_n \int_{-\infty}^{\tau_n} d\tau_{n-1} \ldots \int_{-\infty}^{\tau_2} d\tau_1 \vec{E}(\tau_n)\vec{E}(\tau_{n-1})\ldots\vec{E}(\tau_1) \\ U_0(t)[\vec{\mu}_I(\tau_n), [\vec{\mu}_I(\tau_{n-1}), \ldots [\vec{\mu}_I(\tau_1), \\ \rho(-\infty)]\ldots]]U_0^\dagger(t) \tag{2.44}$$

Here the dipole operator in the interaction picture $\vec{\mu}_I(t) = U_0^\dagger(t)\vec{\mu}U_0(t)$. $\rho(-\infty)$ is the equilibrium density matrix and hence does not evolve over time. We have considered a series of time points τ_n at which the system interacts with a perturbation. Since 2DES is an example of third order nonlinear spectroscopy, we need to calculate the third order polarisation. To do this, again following Hamm [26], we substitute Eq. 2.44 into Eq. 2.40 and change the time variables to those discussed in Sect. 2.3.1 to obtain:

$$\vec{P}^{(3)}(t) = (-i/\hbar)^3 \int_0^\infty dt_d \int_0^\infty dT \int_0^\infty d\tau \vec{E}(t-t_d)\vec{E}(t-t_d-\tau)\vec{E}(t-t_d-T-\tau) \\ \mathrm{Tr}\left(\vec{\mu}(t_d+T+\tau)[\vec{\mu}(T+\tau), [\vec{\mu}(\tau), [\vec{\mu}(0), \rho(-\infty)]]]\right) \tag{2.45}$$

Equation 2.45 shows that the polarisation is created by the incident electric fields interacting with the material. In the semi-impulsive limit, we assume that the laser pulses are long with respect to the oscillation period of light, but short compared to the timescales of the system [26]. We can therefore write the electric fields as:

$$\vec{E}_1(t) = \vec{E}_{1,0}\,\delta(t)\exp(\pm i\omega_1 t \mp \vec{k}_1.\vec{r}) \tag{2.46}$$
$$\vec{E}_2(t) = \vec{E}_{2,0}\,\delta(t-\tau)\exp(\pm i\omega_2 t \mp \vec{k}_2.\vec{r}) \tag{2.47}$$
$$\vec{E}_3(t) = \vec{E}_{3,0}\,\delta(t-\tau-T)\exp(\pm i\omega_3 t \mp \vec{k}_3.\vec{r}) \tag{2.48}$$

where $\omega_{1,2,3}$ is the frequency of pulse 1, 2 or 3 and $\vec{k}_{1,2,3}$ is the wavevector of pulse 1, 2 or 3. Normally all pulses have the same frequencies, although different frequencies are possible. The wavevectors (and the direction in which the signal is detected)

can be chosen experimentally. Note that in practice the laser pulses are finite, which means that the electric fields can overlap at short waiting times, T. This leads to additional signals and produces the 'coherent artefact', which is often observed in 2D spectra at early T [26].

In the limit of infinitely short pulses, the third order response (the signal) is equal to the third order polarisation:

$$S(\tau, T, t_d) = P^{(3)}(t) \tag{2.49}$$

The polarisation acts as a source, generating electric fields in the directions $\vec{k}_s = \pm\vec{k}_1 \pm \vec{k}_2 \pm \vec{k}_3$. In 2DES, normally the rephasing (R) and non-rephasing (NR) signals are measured at $\vec{k}_{I/II} = \mp\vec{k}_1 \pm \vec{k}_2 + \vec{k}_3$. Conventional 2D spectra are obtained by taking Fourier transforms of the signal along both t_d and τ, to obtain $S_{R/NR}(\omega_\tau, T, \omega_{t_d})$:

$$S_{R/NR}(\omega_\tau, T, \omega_{t_d}) = \int_0^\infty \int_0^\infty d\tau dt_d S_{R/NR}(\tau, T, t_d) e^{\mp i\omega_\tau \tau} e^{+i\omega_{t_d} t_d} \tag{2.50}$$

ω_τ is called the absorption or excitation frequency, whilst ω_{t_d} is the emission or probe frequency. Note that the rephasing and non-rephasing spectra contain both absorptive and dispersive contributions. A pure absorptive spectrum can be produced by adding them together [5].

By obtaining spectra at different T we can observe the system's dynamics, as illustrated in Fig. 2.9. In addition, by taking a third Fourier transform over T we can obtain the frequencies at which 2D signals oscillate and hence study the vibrations or electronic coherences which play a role in the system's dynamics. Several papers have shown that it can be helpful to plot 'beating maps' from the 2D data (sometimes referred to as 'Fourier maps') [32–34]. These maps plot the signals which oscillate at a certain frequency during the waiting time. Specifically, instead of plotting $S_{R/NR}(\omega_\tau, T, \omega_{t_d})$, we plot [34]:

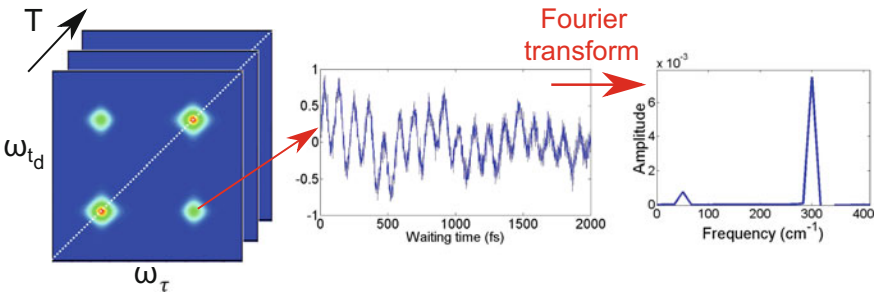

Fig. 2.9 2D spectra can be produced at different waiting times. Signals at specific points in the 2D spectrum can be plotted as a function of the waiting time and the oscillation frequencies can be obtained using a Fourier transform. Image of 2D spectrum adapted from [31]

$$\mathrm{A}_{R/NR}(\omega_\tau, \omega_T, \omega_{t_d}) = \int_0^\infty \mathrm{dT} \exp(i\omega_T T)\mathrm{Re}(\mathrm{S}_{R/NR}(\omega_\tau, T, \omega_{t_d})) \tag{2.51}$$

From the beating maps, we can learn more about the amplitude of the signals which oscillate at specific frequencies in different regions of the 2D spectrum. Notice that here the real part of the signal $\mathrm{S}_{R/NR}(\omega_\tau, T, \omega_{t_d})$ is taken; in Chap. 3 I will discuss the additional information which can be obtained from the signal's phase.

2.3.3 Interpreting 2D Spectra

2.3.3.1 Feynman Diagrams

Expanding the commutators in the expression for the third order polarisation (Eq. 2.45) we obtain eight terms which are the response functions: R_1, R_2, R_3, R_4 and their complex conjugates, for example:

$$R_3 = -\left(\frac{i}{\hbar}\right)^3 \mathrm{Tr}\left(\vec{\mu}(t_d + T + \tau)\vec{\mu}(T + \tau)\rho(-\infty)\vec{\mu}(0)\vec{\mu}(\tau)\right) \tag{2.52}$$

The third order response functions can be visualised using Feynman diagrams [11, 25, 26]. In particular, they can be represented by four Feynman diagrams, whose structures are shown in Fig. 2.10. Time runs from the bottom to the top and the two vertical lines correspond to the ket and the bra of the density matrix. Arrows pointing towards/away from the diagram represent absorption/emission of light by the sample. Note that the final interaction, which produces the signal, must always emit light.

As an example, the term given by Eq. 2.52 is represented by the diagram labelled R_3 in Fig. 2.10. There are two interactions with the ket of the density matrix at times $T + \tau$ and $t_d + T + \tau$ and two interactions with the bra at times 0 and τ. The other terms in Eq. 2.45 correspond to the other diagrams and their complex conjugates. Note that R_2 and R_3 represent rephasing signals, whilst R_1 and R_4 correspond to non-rephasing signals. Experimentally, the rephasing and non-rephasing signals are

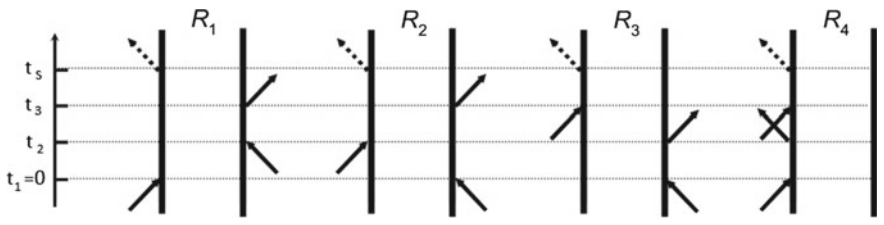

Fig. 2.10 Example Feynman diagrams [26]

observed at $\vec{k}_{\mathrm{I/II}} = \mp\vec{k}_1 \pm \vec{k}_2 + \vec{k}_3$, as discussed previously. The rephasing signals are so-named because the signal oscillates with opposite phases during the detection and coherence times. This flip in oscillation frequency allows the system to 'rephase' in an analogous way to spin vectors in magnetic resonance [26].

Each Feynman diagram represents a peak in the 2D spectrum. The axes of the 2D spectrum correspond to the excitation and probe frequencies, ω_τ and ω_{t_d}, represented by the first and the final arrow of each Feynman diagram respectively (as discussed previously, these axes are obtained by taking a Fourier transform across the coherence and detection times). If we neglect dissipation, the amplitude of a peak in the 2D spectrum is determined by the product of the transition dipole moments involved in the Feynman diagram (illustrated by arrows in Fig. 2.10). Including dissipation will change the magnitudes of the peaks and determine their shapes in the 2D spectra. One way to approximate the effects of dissipation is to assume Markovian dephasing, in which case the lineshapes can be modelled using Lorentzian functions (we will take this approach in Chap. 3). Further discussion of the lineshapes of 2D spectra can be found for example in Cho [29].

2.3.3.2 Assigning Peaks in 2D Spectra

As discussed in Sect. 2.1, organic and biological systems are composed of a large number of interacting molecules and hence need to be described using an excitonic framework. Once the excitations of the system are known, the Feynman diagram approach described above can be applied to examine the light-induced transitions which occur between them. The system's eigenstates form three distinct manifolds: the ground state manifold, g, the excited state manifold, e, and a higher excited manifold, f. Transitions between these manifolds result in three types of signals which can contribute to the peaks observed in 2D spectra: ground state bleach (GSB), stimulated emission (SE) and excited state absorption (ESA). Generic rephasing and non-rephasing Feynman diagrams for each of these signals are shown in Fig. 2.11. GSB diagrams involve dynamical evolution in the ground state manifold during the waiting time. SE and ESA diagrams evolve in the excited state manifold during the waiting time, but in SE the final transition involves emission back to the ground state manifold, whilst in ESA the final transition involves the higher excited manifold.

To illustrate how the peaks in the 2D spectra arise from the Feynman diagrams, consider an electronic dimer composed of a ground state and two excited states, e_1 and e_2, which are eigenstates of the system (see Fig. 2.12b). Two example Feynman diagrams for this system are shown in Fig. 2.13; others also exist. Diagram a leads to a diagonal peak in the 2D spectrum (i.e. one where $\omega_{t_d} = \omega_\tau$), since both the first and last light interactions involve a transition between g and e_1. Furthermore, the system evolves in the population state $|g\rangle\langle g|$ during the waiting time, so the corresponding peak does not oscillate as a function of the waiting time. In general, diagonal peaks are expected in the spectra at energies corresponding to exciton absorption energies.

Meanwhile, Feynman diagram b leads to an off-diagonal peak, because the initial excitation is from g to e_1, whilst the emission of light is from e_2 to g. When off-

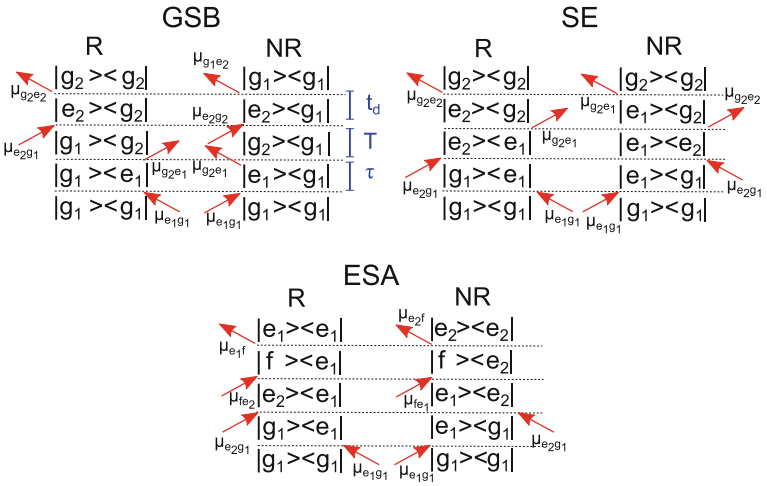

Fig. 2.11 Generic Feynman diagrams for the third-order nonlinear optical response functions [27]

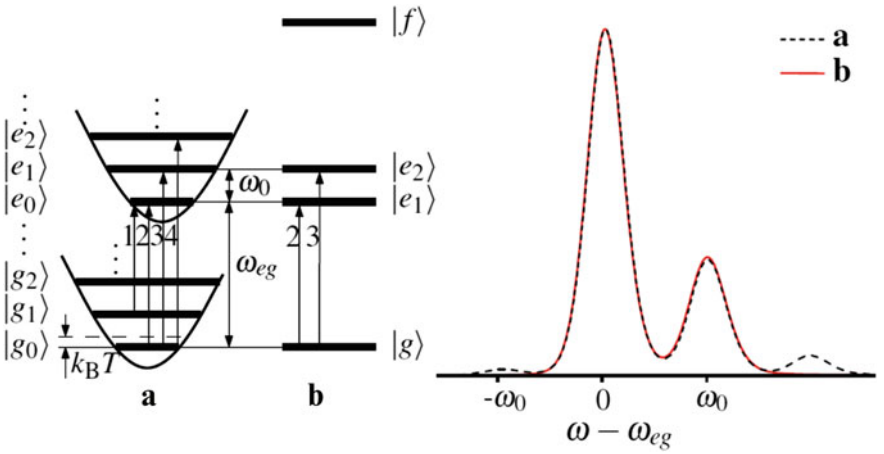

Fig. 2.12 Energy level structure of the displaced oscillator (**a**) and electronic dimer (**b**) and corresponding linear absorption spectra. Figure reprinted from [35], with permission from Elsevier

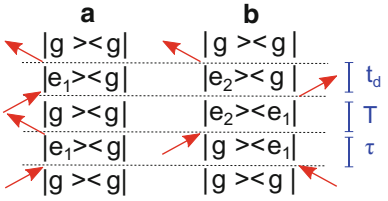

Fig. 2.13 Feynman diagrams for two peaks in the 2D spectrum of an electronic dimer system

diagonal peaks such as this one occur at short waiting times, they provide evidence for the existence of electronic couplings between pigments [5] (at longer waiting times, the picture may be complicated by energy transfer processes). Furthermore, if quantum coherences exist between the excitons, cross-peaks oscillate as a function of the waiting time with a frequency equal to the energy difference between the excitons involved [5] and this signal can be observed in the beating maps. For example, the peak from diagram b oscillates at a frequency corresponding to the energy difference between e_2 and e_1 during the waiting time and will therefore be observed in the beating map with that frequency. This is because it evolves in the quantum coherent state $|e_2\rangle\langle e_1|$ during the waiting time and the evolution of this coherent state is given by:

$$|e_1(T)\rangle\langle e_2(T)| = e^{-iE_{12}T}|e_1\rangle\langle e_2| \tag{2.53}$$

Note also that Feynman diagrams a and b in Fig. 2.13 are examples of non-rephasing and rephasing signals respectively. Measuring only the rephasing or non-rephasing signal can help to distinguish which diagrams contribute to specific peaks.

2.3.3.3 Distinguishing Electronic and Vibrational Features

Often, linear absorption spectra cannot distinguish between electronic and vibrational features. Work by Butkus et al. [35] showed that this is possible using 2DES. They considered two systems with the same linear absorption spectra: a displaced harmonic oscillator (DO) and an electronic dimer (ED), shown in Fig. 2.12. They then plotted the different peak patterns which would be expected in the 2D spectra of these two systems, see Fig. 2.14, allowing them to be distinguished. Note that here open symbols correspond to oscillatory signals, which will be observed in the corresponding frequency beating map, whilst closed symbols represent non-oscillatory signals. The differences in the patterns obtained are extremely useful to interpret complicated 2D spectra, particularly when both rephasing and non-rephasing data is available.

The electronic dimer case was discussed above; Feynman diagram a now appears as a solid (non-oscillatory) diamond at $(\omega_{eg}, \omega_{eg})$ in the non-rephasing ED diagram (Fig. 2.14, bottom right) and Feynman diagram b appears as an open (oscillatory) square at $(\omega_{eg}, \omega_{eg} + J)$ in the rephasing ED diagram (Fig. 2.14, bottom left). Note that J is related to the coupling between the sites. Notice that this means that peak b will be present in the beating maps, but not peak a. Overall, the electronic dimer non-rephasing beating map has two diagonal peaks, whilst the rephasing beating map has two off-diagonal peaks (see the open symbols in Fig. 2.14).

The displaced oscillator case can be treated similarly and gives a different set of peaks. For example, the Feynman diagram in Fig. 2.15 leads to the off-diagonal peak represented by an open diamond at $(\omega_{eg}, \omega_{eg} - \omega_0)$ in the DO rephasing diagram. This peak will oscillate due to the difference in vibrational quanta between g_0 and g_1. Notice that unlike in the electronic dimer case, light can now be emitted at frequencies lower than ω_{eg}. This is because the final state may be the ground state

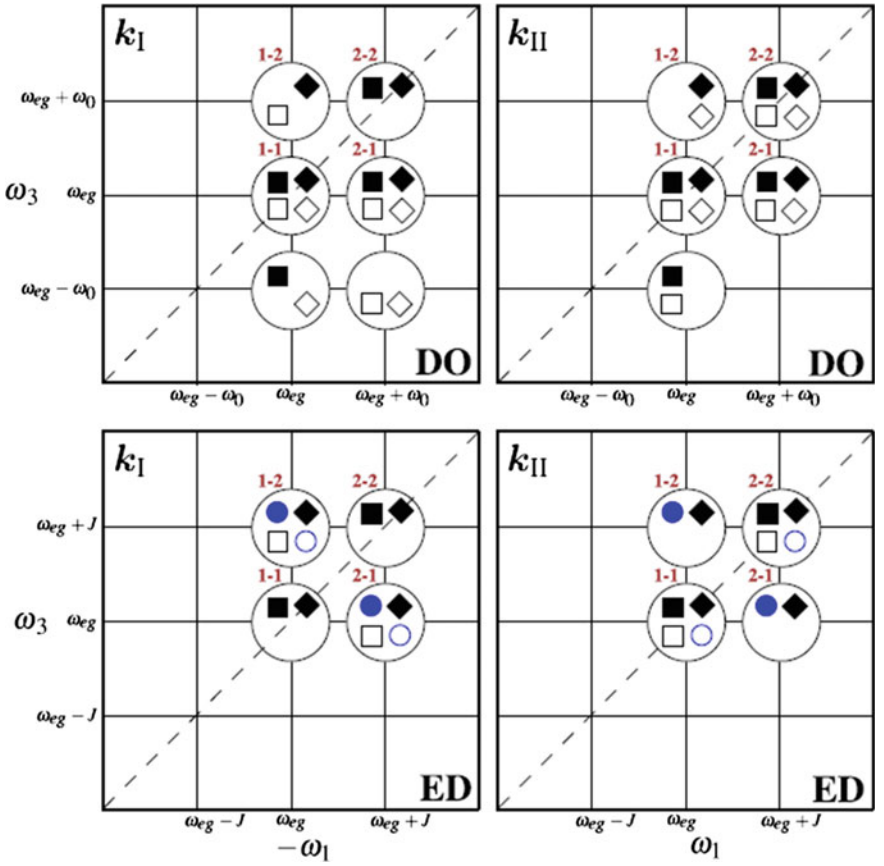

Fig. 2.14 Contributions to the 2D spectra of the rephasing (k_I) and non-rephasing (k_{II}) signals for the displaced oscillator (DO) and electronic dimer (ED) schemes. *Squares*, *diamonds* and *circles* indicate SE, GSB and ESA signals respectively. *Solid* (*open*) symbols denote non-oscillating (oscillating) contributions. Figure adapted from [35], with permission from Elsevier

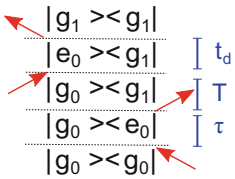

Fig. 2.15 Feynman diagram for the peak represented by an open diamond at $(\omega_{eg}, \omega_{eg}-\omega_0)$ in the DO rephasing diagram, see Fig. 2.14

with a vibrational quantum, giving a lower probe frequency, as in Stokes scattering in Raman spectroscopy. It is normally assumed that the system is initially in the ground state with no vibrational quanta, although this assumption breaks down for low frequency modes at high temperature. There are now five peaks in each of the

rephasing and non-rephasing beating maps, compared to only two in the electronic dimer beating maps.

The characteristic electronic dimer and vibrational peak patterns described above have now been observed multiple times in the literature and provide an easy way to identify the origins of 2D signals [22, 36–38]. Nonetheless, this simplified picture should be used with care because other effects (including limited laser spectrum width) can alter the peak patterns significantly. This point will be discussed in more detail in Chap. 3.

References

1. Weiner, J., Nunes, F.: Light-Matter Interaction: Physics and Engineering at the Nanoscale. Oxford University Press (2013)
2. Bardeen, C.: The structure and dynamics of molecular excitons. Annu. Rev. Phys. Chem. **65**, 127–148 (2014)
3. van Amerongen, H., Valkunas, L., van Grondelle, R.: Photosynthetic Excitons. World Scientific (2000)
4. Davydov, A.: Theory of absorption spectra of molecular crystals. Zh. Eksp. Teor. Fiz. **18**, 210–218 (1948)
5. Schlau-Cohen, G., Ishizaki, A., Fleming, G.: Two-dimensional electronic spectroscopy and photosynthesis: Fundamentals and applications to photosynthetic light-harvesting. Chem. Phys. **386**, 1–22 (2011)
6. Frenkel, Y.: On the transformation of light into heat in solids I. Phys. Rev. **37**, 17 (1931)
7. Frenkel, Y.: On the transformation of light into heat in solids II. Phys. Rev. **37**, 1276 (1931)
8. Wannier, G.H.: The structure of electronic excitation levels in insulating crystals. Phys. Rev. **52**, 191 (1937)
9. Mott, N.F.: Conduction in polar crystals. II. The conduction band and ultra-violet absorption of alkali-halide crystals. Trans. Farad. Soc. **34**, 500–506 (1938)
10. Blankenship, R.: Molecular Mechanisms of Photosynthesis, 2 edn. Wiley-Blackwell (2014)
11. Tokmakoff, A.: Time-Dependent Quantum Mechanics and Spectroscopy (2016). https://tdqms.uchicago.edu/
12. Dexter, D.L.: A theory of sensitized luminescence in solids. J. Chem. Phys. **21**, 836 (1953)
13. Vos, J.G., Forster, R.J. Keyes, T.E.: Interfacial Supramolecular Assemblies. John Wiley and Sons, Ltd (2003)
14. Larsen, P.D.: Dexter Energy Transfer (2016). http://chemwiki.ucdavis.edu/Theoretical_Chemistry/Fundamentals/Dexter_Energy_Transfer
15. Weiss, U.: Quantum Dissipative Systems. World Scientific (2012)
16. Chin, A., Huelga, S., Plenio, M.: Chain representations of open quantum systems and their numerical simulation with time-adapative density matrix renormalisation group methods. In: Wurfel, U., Thorwart, M., Weber, E. (eds.) Quantum Efficiency in Complex Systems, Part II. Academic Press (2011)
17. Blum, K.: Density Matrix Theory and Applications. Springer (1981)
18. Egorova, D., Kühl, A., Domcke, W.: Modeling of ultrafast electron-transfer dynamics: multi-level Redfield theory and validity of approximations. J. Chem. Phys. **268**, 105–120 (2001)
19. Egorova, D., Thoss, M., Domcke, W., Wang, H.: Modeling of ultrafast electron-transfer processes: validity of multilevel Redfield theory. J. Chem. Phys. **119**, 2761–2773 (2003)
20. Ishizaki, A., Fleming, G.R.: Unified treatment of quantum coherent and incoherent hopping dynamics in electronic energy transfer: reduced hierarchy equation approach. J. Chem. Phys. **130**, 234111 (2009)

21. Panitchayangkoon, G., Voronine, D.V., Abramavicius, D., Caram, J.R., Lewis, N.H.C., Mukamel, S., Engel, G.S.: Direct evidence of quantum transport in photosynthetic light-harvesting complexes. Proc. Natl. Acad. Sci. **108**, 20908–20912 (2011)
22. Romero, E., Augulis, R., Novoderezhkin, V.I., Ferretti, M., Thieme, J., Zigmantas, D., van Grondelle, R.: Quantum coherence in photosynthesis for efficient solar-energy conversion. Nat. Phys. **10**, 676–682 (2014)
23. Mohseni, M., Omar, Y., Engel, G.S., Plenio, M.B.: Quantum Effects in Biology. Cambridge University Press (2014)
24. Hybl, J., Albrecht, A., Faeder, S.G., Jonas, D.: Two-dimensional electronic spectroscopy. Chem. Phys. Lett. **297**, 307–313 (1998)
25. Mukamel, S.: Principles of Nonlinear Optical Spectroscopy. Oxford University Press (1995)
26. Hamm, P.: Principles of nonlinear optical spectroscopy: a practical approach (2005). http://www2.chemistry.msu.edu/faculty/beck/CEM987/downloads/Hamm.pdf
27. Bakulin, A.A., Morgan, S.E., Kehoe, T.B., Wilson, M.W.B., Chin, A.W., Zigmantas, D., Egorova, D., Rao, A.: Real-time observation of multiexcitonic states in ultrafast singlet fission using coherent 2D electronic spectroscopy. Nat. Chem. **8**, 16–23 (2016)
28. Fuller, F.D., Ogilvie, J.P.: Experimental implementations of two-dimensional Fourier transform electronic spectroscopy. Annu. Rev. Phys. Chem. **66**, 667–690 (2015)
29. Cho, M.: Coherent two-dimensional optical spectroscopy. Chem. Rev. **108**, 1331–1418 (2008)
30. Panman, M., Shaw, D., Ensing, B., Woutersen, S.: Local orientational order in liquids revealed by resonant vibrational energy transfer. Phys. Rev. Lett. **113**, 207801 (2014)
31. Huang, J. 2D coherent spectroscopy of energy harnessing materials (2016). http://www.jyhuang.idv.tw/2DCS_maters.aspx
32. Calhoun, T.R., Ginsberg, N.S., Schlau-Cohen, G.S., Cheng, Y.-C., Ballottari, M., Bassi, R., Fleming, G.R.: Quantum coherence enabled determination of the energy landscape in light-harvesting complex II. J. Phys. Chem. B **113**, 16291–16295 (2009)
33. Turner, D.B., Dinshaw, R., Lee, K.-K., Belsley, M.S., Wilk, K.E., Curmic, P.M.G., Scholes, G.D.: Quantitative investigations of quantum coherence for a light-harvesting protein at conditions simulating photosynthesis. Phys. Chem. Chem. Phys. **14**, 4857–4874 (2012)
34. Butkus, V., Zigmantas, D., Abramavicius, D., Valkunas, L.: Distinctive character of electronic and vibrational coherences in disordered molecular aggregates. Chem. Phys. Lett. **587**, 93–98 (2013)
35. Butkus, V., Zigmantas, D., Valkunas, L., Abramavicius, D.: Vibrational vs. electronic coherences in 2D spectrum of molecular systems. Chem. Phys. Lett. **545**, 40–43 (2012)
36. Caram, J.R., Fidler, A.F., Engel, G.S.: Excited and ground state vibrational dynamics revealed by two-dimensional electronic spectroscopy. J. Chem. Phys. **137**, 024507 (2012)
37. Westenhoff, S., Palecek, D., Edlund, P., Smith, P., Zigmantas, D.: Coherent picosecond exciton dynamics in a photosynthetic reaction center. J. Am. Chem. Soc. **134**, 16484–16487 (2012)
38. Fuller, F.D., Pan, J., Gelzinis, A., Butkus, V., Senlik, S.S., Wilcox, D.E., Yocum, C.F., Valkunas, L., Abramavicius, D., Ogilvie, J.P.: Vibronic coherence in oxygenic photosynthesis. Nat. Chem. **6**, 706–711 (2014)

Chapter 3
2D Spectroscopy of Pentacene Thin Films

Everything should be made as simple as possible, but not simpler.

Albert Einstein

As discussed in Chap. 2, 2DES offers unprecedented access to ultrafast quantum dynamics and can also give crucial information about relaxation, vibrational and dephasing processes. Nonetheless, it is a relatively new technique and to date it has proved difficult to develop theoretical models to explain 2D data, mainly due to the sheer volume of information contained in the spectra and the complexity of the biological systems which 2DES is often applied to. Organic materials, which are generally simpler than their biological counterparts, may thus provide an excellent 'testing ground' for 2DES. Moreover, organic materials have interesting applications for photovoltaics in their own rights. For example, in this chapter we apply 2DES to the organic material pentacene, which undergoes a novel process known as singlet fission. Singlet fission has been proposed as a solution to breaking the Shockley Queisser limit, which restricts the energy efficiency of solar cells to around 33% [1].

I begin by describing pentacene's structure and what is known about the singlet fission mechanism, which is still a subject of ongoing debate. In the rest of the chapter I present work applying 2DES to study fission in pentacene thin films [2]. I outline the experimental 2DES results, which were obtained by Artem Bakulin, Akshay Rao and Donatas Zigmantas, before presenting a full theoretical model which can reproduce the quantum dynamics and peak patterns observed in the 2D spectra. The sign of the experimental oscillation frequencies provides further validation of the model. Our results elucidate the importance of vibrations for detecting and characterising 'dark' entangled intermediate states in pentacene and for driving ultrafast fission. The theoretical work in this section was carried out in collaboration with Dassia Egorova, who calculated the ultrafast dynamics and contributed to creating the figures and determining the theoretical model (alongside myself and Alex Chin).

S.E. Morgan, *Ultrafast Quantum Effects and Vibrational Dynamics in Organic and Biological Systems*, Springer Theses, DOI 10.1007/978-3-319-63399-2_3

3.1 Structure of Pentacene

Pentacene is a polycyclic aromatic hydrocarbon, which consists of five fused benzene rings, as shown in Fig. 3.1. It can be studied in solution as well as in thin films. In thin films, the pentacene molecules form a triclinc structure with two molecules per unit cell and 'herringbone' packing in which the face of one molecule is close to the edge of the adjacent molecule [3], see Fig. 3.2. The existence of two molecules per unit cell leads to Davydov splitting, which can be observed in the absorption spectrum.

It is also possible to synthesise derivatives of pentacene in which hydrogen atoms are substituted for side-chains, for example 6,13-bis(triisopropyl-silylethynyl) pentacene (TIPS) and 6,13-di(2-thienyl) pentacene (DTP). The structures of these mole-

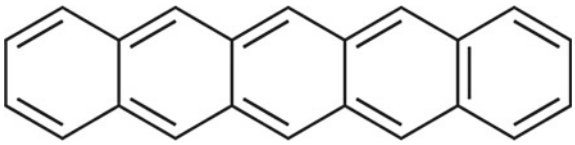

Fig. 3.1 Pentacene molecule. Figure adapted from [4] with permission of the Royal Society of Chemistry

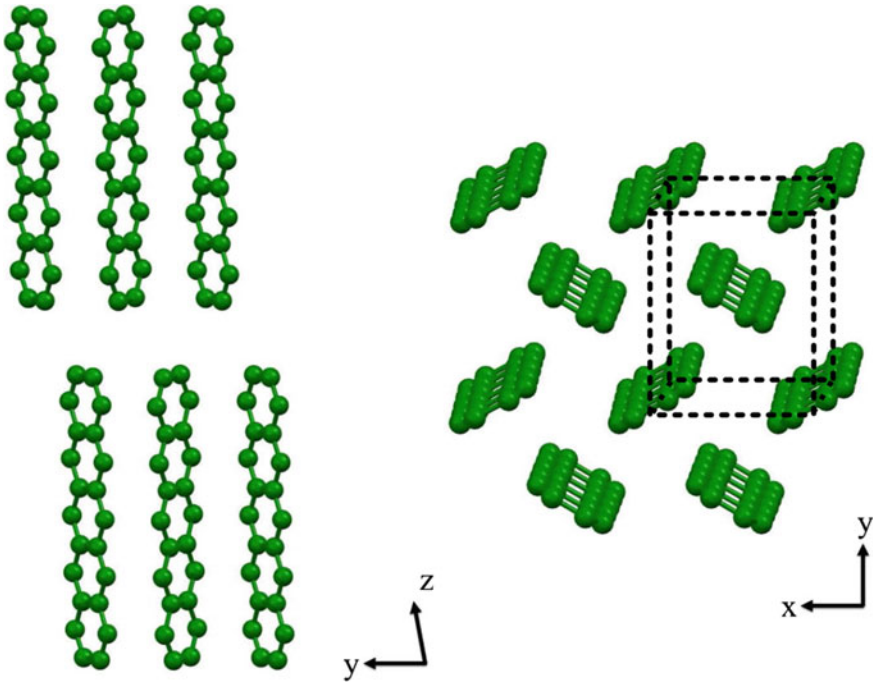

Fig. 3.2 Packing structure of pentacene, with unit cell indicated in *black*. Figure adapted from [5] with permission from Elsevier

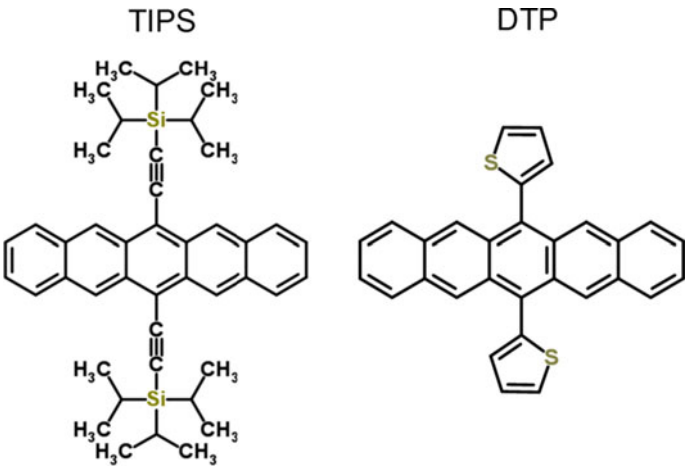

Fig. 3.3 Structures of pentacene derivatives TIPS [8] and DTP [9], reproduced by permission of The Royal Society of Chemistry

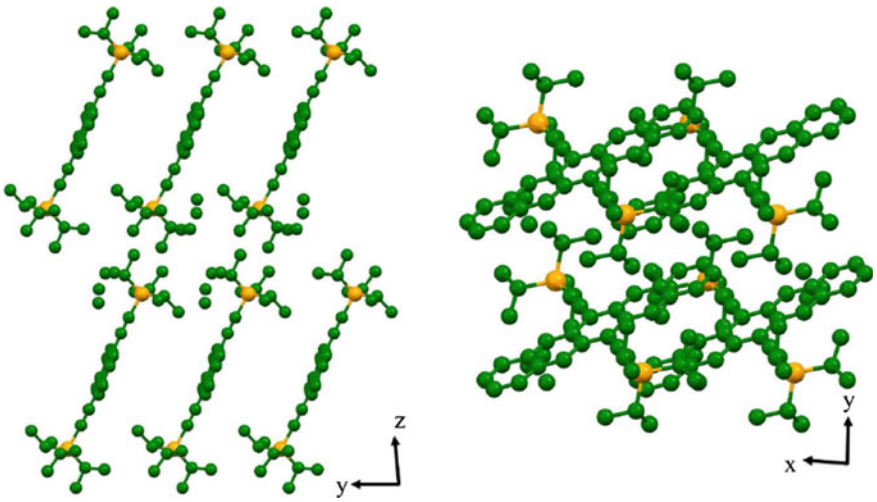

Fig. 3.4 Packing structure of TIPS pentacene. Figure adapted from [5] with permission from Elsevier

cules are shown in Fig. 3.3. Note that the side-chains lead to different molecular packing and alter the interactions between pentacene molecules. For example, TIPS pentacene packs in the 'brick-wall' formation [6] shown in Fig. 3.4, with a $\pi - \pi$ stacking distance of 3.3 Å [7]. This is closer than the intermolecular distance of 3.5 Åin the herringbone pentacene structure, leading to stronger electronic couplings between adjacent molecules [7].

3.2 Singlet Fission

Pentacene has attracted significant attention recently due to its ability to perform singlet fission, which is the spin-allowed conversion of one spin singlet excitation into two triplet excitations [10]. This process is of considerable interest because it offers the possibility of circumventing the Shockley-Queisser limit, by using high energy photons to generate two excitons [1]. More generally, multiple exciton generation can also occur via other mechanisms (e.g. Auger ionisation) and may be able to improve photovoltaic efficiencies in quantum dots and other semiconductor nanostructures, see for example [11].

However, the physical mechanism underlying singlet fission is still not well understood. This is partly due to its ultrafast speed, for example in pentacene singlet fission occurs within 100 fs [12] and easily outcompetes other singlet relaxation processes, including intersystem crossing. To date fission has mostly been observed in thin films and crystals [13], although a few examples have recently been found in solution and in covalent dimers [14, 15]. The similarities and differences between the fission mechanism in these materials remain unclear and a better understanding is needed to inform the design of more fission materials.

In 1969, Merrifield et al. [16] proposed a kinetic model for singlet fission, which is illustrated in Fig. 3.5 and can be written as:

$$S_1 \rightarrow TT \rightarrow T + T \tag{3.1}$$

where S_1 is the lowest singlet excited state, which is delocalised across at least two pentacene molecules. T is a single triplet excitation and TT represents a bound spin-correlated pair of triplet excitations, which together form a spin singlet state. This intermediate multiexciton state is expected to be optically dark, i.e. it cannot be populated directly from the ground state due to its doubly excited (two electron) character [10].

The nature of the coupling between S_1 and TT in pentacene thin films is a subject of ongoing debate [10] and suggested values for its strength vary from $0.02-0.11$ eV ($200-900$ cm^{-1}) [17–19], compared to an energy difference between the states of $\approx$900 cm^{-1}. Initially, direct Coulomb coupling was suggested [19, 20], however this is now believed to be insufficient to explain the fast fission rates observed [19]. More

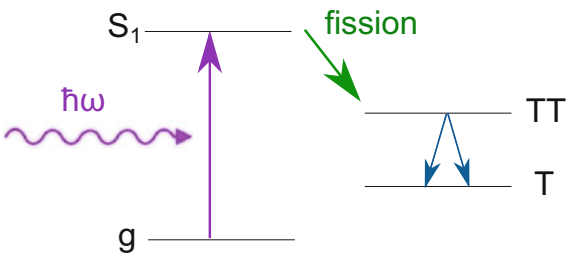

Fig. 3.5 Sketch of singlet fission mechanism

recently, Chan et al. proposed that the initial optical excitation creates a superposition of the singlet and multiexciton states and fission proceeds via the intermediate multiexciton state [13, 21]; we will return to this idea in Sect. 3.5. Meanwhile theoretical work by Beljonne et al. [17] suggested that charge-transfer states could mix with singlet and triplet excitations, leading to indirect coupling. This proposal has gained popularity [19], however, there is still debate over the energies of the charge-transfer states and whether they act as actual intermediate states or as virtual states which mediate the coupling between S_1 and TT via a type of 'super-exchange' [22]. Some recent theoretical work has also begun to evaluate the influence of molecular motion in modulating the coupling between S_1 and TT in acene derivatives which exhibit singlet fission [18, 23, 24]. Berkelbach et al. were the first to consider the impact of vibrational coupling on exciton dynamics in crystalline pentacene [18] and obtained qualitatively similar absorption spectra and singlet fission rates to experimental results. Calculations by Damrauer et al. [24] also suggest that certain modes in tetracene dimers make significant contributions to the coupling between S_1 and TT.

Certain pentacene derivatives can perform singlet fission and some work has focussed on these to elucidate the fission mechanism. Notably, Yost et al. [7] studied ten acene derivatives, including pentacene, TIPS and DTP. They measured the fission rates experimentally using ultrafast transient absorption spectroscopy and obtained timescales of 80, 100 and 160 fs for pentacene, TIPS and DTP respectively. They also used constrained density functional theory with configuration interaction to calculate couplings between S_1 and TT of 19, 56 and 10 meV for pentacene, TIPS and DTP respectively (without charge-transfer mixing). Ultimately, they propose a Bixon-Jortner type model, which predicts different fission rates depending on the coupling strength. In this model fission is non-adiabatic in weakly interacting systems, whereas in strongly interacting systems fission becomes adiabatic and independent of the coupling strength. In this regime the fission rate is determined by the speed of nuclear rearrangement [7].

3.3 Experimental Results

In order to study the fission mechanism further, 2DES was performed on thin films of pentacene, TIPS and DTP, which were introduced above and all undergo fission on a $<$200 fs timescale [7]. The films' absorption spectra are plotted in Fig. 3.6a and show that the bright singlet state has an energy of 1.83 eV in pentacene, which is altered to 1.75 eV and 1.86 eV in TIPS and DTP respectively. A single triplet excitation has an energy of 0.86 eV and the doubly excited TT state is therefore expected to lie at 1.72 eV [19]. As discussed above, the TT state represents a spin correlated pair of triplet excitations and is expected to be optically dark. The energy of the TT state is expected to remain the same in TIPS and DTP since the triplet is localized on a single pentacene molecule [25]. Figure 3.6b shows the energies of the key states.

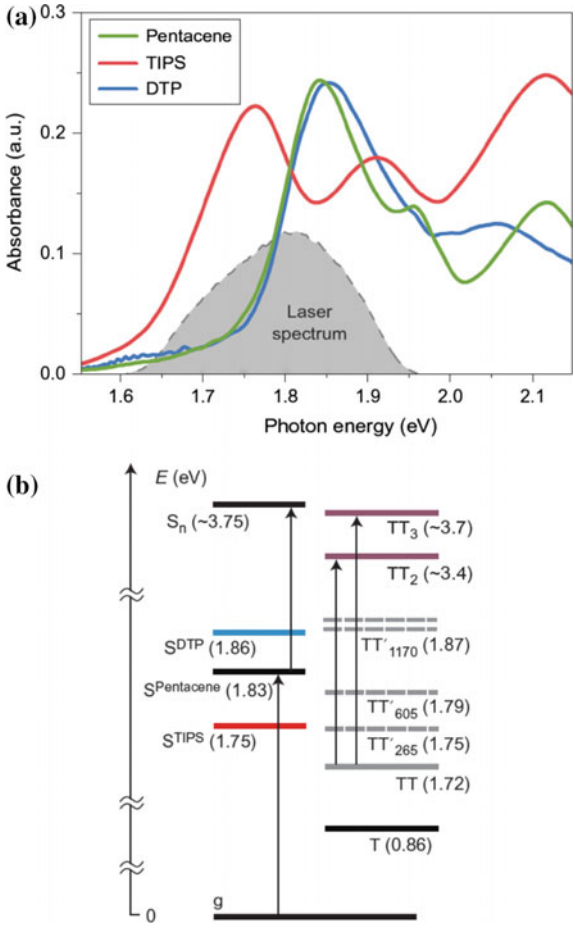

Fig. 3.6 **a** Absorption spectra for pentacene, TIPS and DTP, shown in green, red and blue respectively. The laser spectrum is highlighted in *grey*. **b** Energies of key states in pentacene and its derivatives TIPS and DTP [2]

The 2DES setup used 15 fs laser pulses. The laser spectrum was centred at $14,500\ \text{cm}^{-1}$, with a full-width at half-maximum of $1,800\ \text{cm}^{-1}$ and is shown in Fig. 3.6a. The laser spectrum was broad enough to cover the ground to singlet state transitions for all of the films as well as the region corresponding to the expected energy of TT. The samples were tilted by 50° with respect to the incident beam to enhance ESA from the triplet state to higher lying triplet states, as described in the literature [26].

3.3.1 2D Spectra

Figure 3.7 plots the real part of the 2DES spectra for pentacene at T = 30 fs, 150 fs and 1 ps. A strong peak is observed at the energy of S_1 (1.83 eV), which corresponds to SE and GSB of S_1. This is unsurprising since S_1 is observed in the linear absorption spectrum, see Fig. 3.6a. No peaks are observed at the energy of the multiexcitonic TT state (1.72 eV), which is also expected because the TT state is not observed in the linear absorption spectrum and is believed to be dark, as discussed above. Similar results were obtained for TIPS and DTP (not shown).

3.3.2 Waiting Time Dynamics

3.3.2.1 Decay-Associated Spectra

As discussed in Chap. 2, further insight can be obtained from the waiting time dynamics. Deconvoluting the three-dimensional data matrix for pentacene (ω_τ, T, ω_{t_d}) into 2D decay-associated spectra reveals three underlying components which decay on timescales of 14 fs, 83 fs and 1 ps; see Fig. 3.8. Kinetics for TIPS and DTP are similar, although the second timescale changes to 100 fs and 130 fs respectively. The fastest timescale (14 fs) is assigned to the coherent artefact, discussed in Sect. 2.3.2. The second timescale corresponds well to the singlet fission rates observed previously [7] and is therefore assigned to fission. The third timescale is expected to correspond to vibrational relaxation.

3.3.2.2 Comparison to Resonance Raman Spectra

Examples of the waiting time evolution of specific peaks in the 2D spectra are shown in Fig. 3.9a. In addition to the underlying decays, several oscillatory components are observed. In Fig. 3.9b we take the Fourier transform at each point of the 2D spectra for pentacene, TIPS and DTP and then sum over the complete 2D spectra to obtain the frequencies of the oscillations. The resonance Raman spectra are also shown for comparison. The frequencies of the oscillations in the 2D spectra are extremely similar to those in the Raman spectra, suggesting that they are largely dictated by the system's vibrational modes.

3.3.2.3 Beating Maps

Again as discussed in Chap. 2, beating maps provide a powerful way to extract additional information from 2DES data. Rephasing and non-rephasing experimental beating maps at three of the known vibrational frequencies from Fig. 3.9b are shown

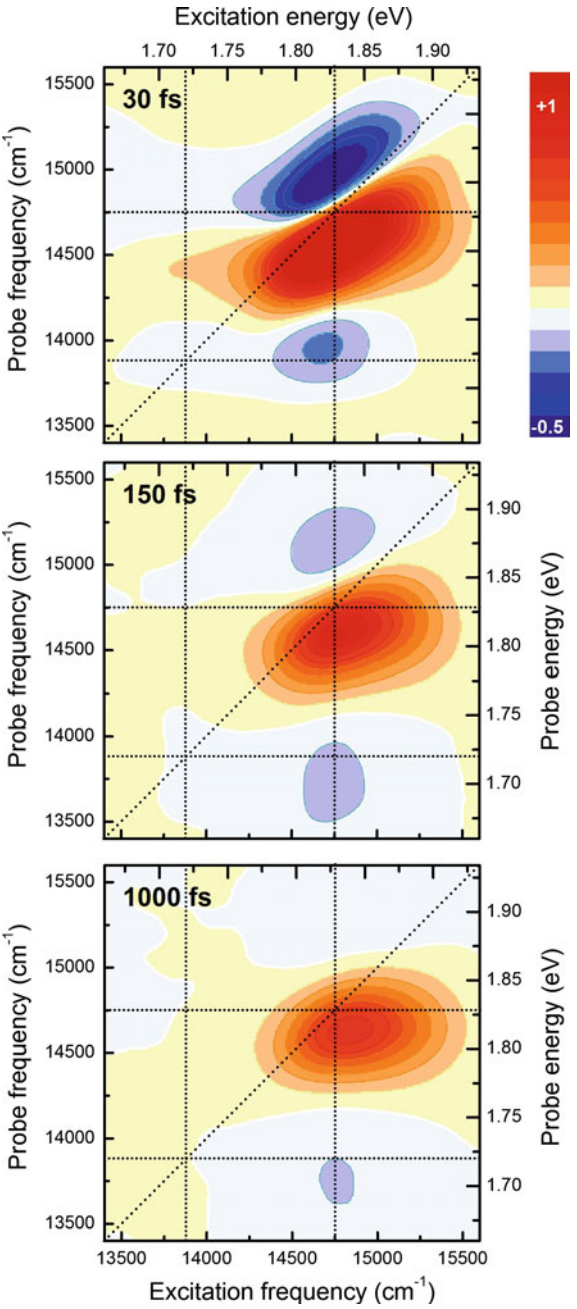

Fig. 3.7 2D spectra for pentacene at T=30 fs, 150 fs and 1 ps [2]

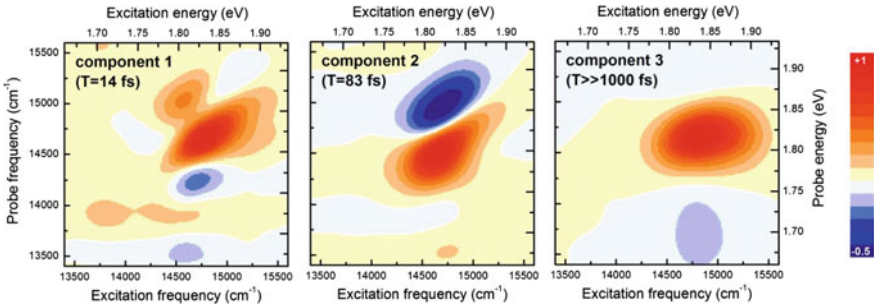

Fig. 3.8 Decay associated spectra for pentacene [2]

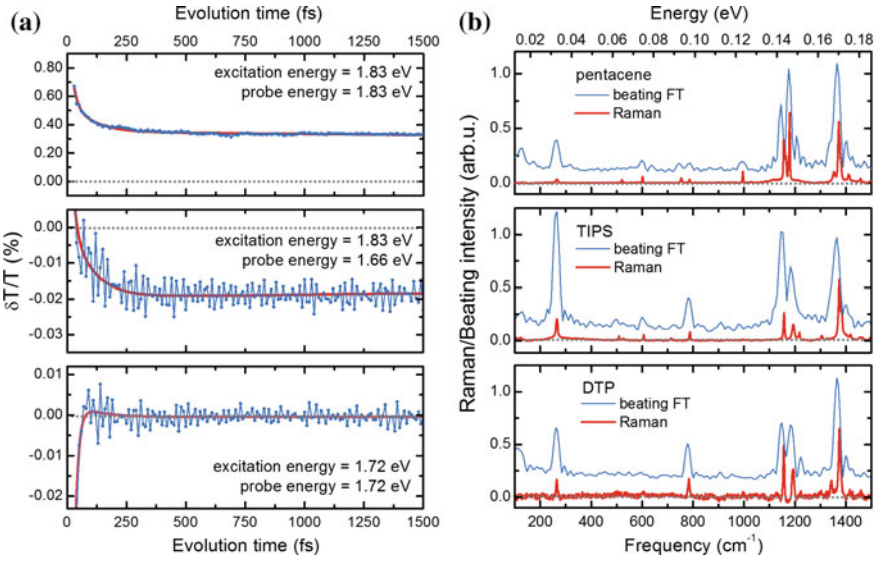

Fig. 3.9 **a** Time traces at specific points in pentacene's 2D spectrum. The red line plots the population dynamics from the decay-associated spectra. **b** *Blue line* Fourier transforms of the waiting time traces for the 2DES data, summed over all points in the 2D spectra, for pentacene and its derivatives. *Red line* resonance Raman spectra [2]

in Fig. 3.10. Total (rephasing plus non-rephasing) beating maps for TIPS and DTP at the same frequencies are shown in Fig. 3.11.

In several of the beating maps we observe peaks with excitation at $\omega_\tau = 1.83$ eV, which arise from GSB and SE of the singlet state. As discussed above, this is expected because S_1 is bright and is observed in both the linear absorption spectrum and the original 2D spectra, see Figs. 3.6 and 3.7. However, in the beating maps we also observe some peaks with excitation at $\omega_\tau = 1.72$ eV, which is the accepted value of the TT energy [19]. This is surprising because TT is expected to be dark due to its doubly excited nature and excitation at this energy is not observed in either the

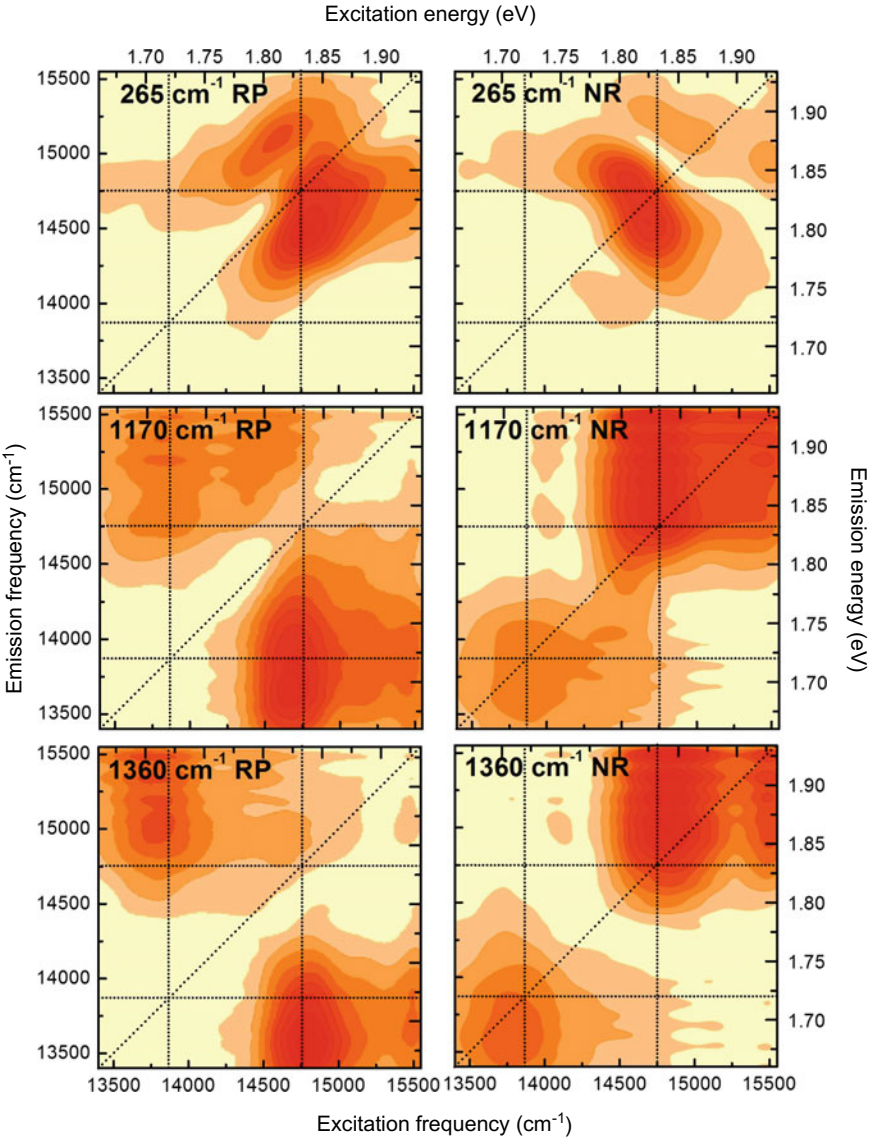

Fig. 3.10 Experimental rephasing and non-rephasing beating maps for pentacene [2]

linear absorption spectrum or in the original 2D spectra. Peaks with this excitation energy are also observed in beating maps for TIPS and DTP, where the energy of TT is expected to be the same, as discussed above. We therefore suggest that these peaks arise from initial excitation onto TT, followed by ESA to a higher lying triplet state. The first of these transitions is expected to be dark, but in the model proposed

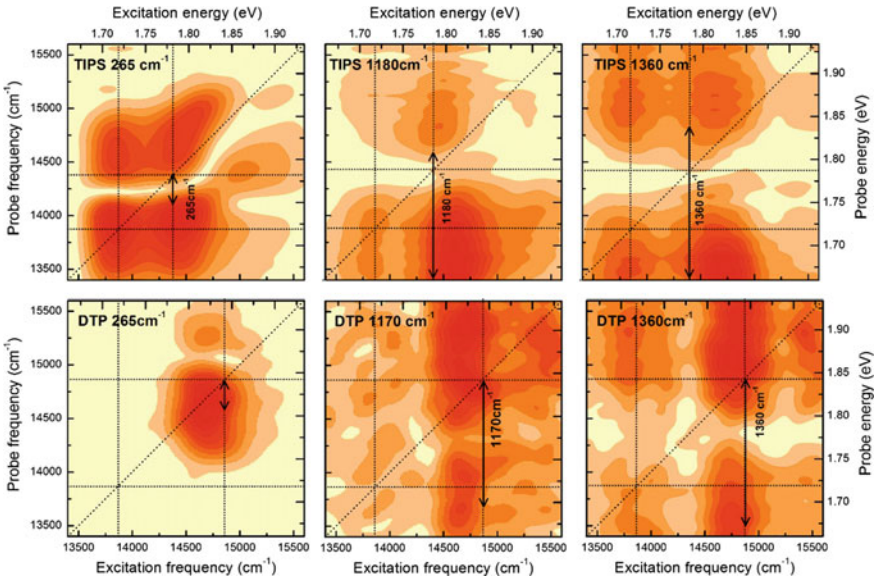

Fig. 3.11 Total beating maps for TIPS and DTP (R+NR) [2]

below we suggest that it can borrow a non-zero dipole moment from the bright singlet state. The second, ESA transition is known to have significant dipole moment from previous experimental studies [26].

In the following, to investigate these results further I introduce a theoretical model, which accounts for vibrational modes on an equal footing to the electronic states. The model's eigenstates are discussed and its ultrafast dynamics are shown to reproduce the known fission rate. The model also agrees with the experimental beating maps and I discuss the origins of the peaks in terms of the eigenstates involved. Finally, I analyse the signs of the 2D oscillation frequencies to provide further confirmation that these signals are caused by excited state coherences in the waiting time.

3.4 Vibronic Model

3.4.1 Model

We propose a model for pentacene where the vibrational modes are treated explicitly, on the same level as the electronic states. This allows us to investigate the role which vibrations play in the fission process. The model is kept as simple as possible, in order to elucidate the minimal requirements for fission and to allow simulation of

the 2DES experiments, which rapidly becomes prohibitively expensive for larger systems. Therefore, we limit our electronic description of the system to the singlet state, S_1, the multiexciton state, TT, a higher lying state, TT_n, discussed further below, and the ground state, g. A small coupling J is introduced between S_1 and TT, which enables a radiationless transition between them. Overall, the system Hamiltonian reads:

$$H_S = \sum_i E_i \left|i\right\rangle \left\langle i\right| + J \left(\left|S_1\right\rangle \left\langle TT\right| + h.c.\right) \tag{3.2}$$

where h.c. is the Hermitian conjugate and i corresponds to S_1, TT, TT_n or g. We choose $E_{S_1} = 15412\,\mathrm{cm}^{-1}$ and $E_{TT} = 13910\,\mathrm{cm}^{-1}$, which ensures that after diagonalisation the energy of the brightest eigenstate corresponds to the known energy of S_1 (1.83 eV) and the energy of the lowest energy eigenstate corresponds to the expected energy of TT (1.72 eV). As discussed in Sect. 3.2, the magnitude of the coupling between S_1 and TT (J) is a source of debate and suggested values range from $200 - 900\,\mathrm{cm}^{-1}$. Here we assume a highly conservative coupling of $J = 248\,\mathrm{cm}^{-1}$. This coupling could be mediated by charge transfer (CT) states via a type of 'super-exchange', although we will not consider CT states explicitly.

Pentacene is also known to have higher lying singlet and triplet states, as shown in Fig. 3.6b. Here we will be mainly concerned with the higher lying triplet states. In particular, we consider a superposition of a single triplet excitation (T) with a higher lying triplet excitation T_n, which we denote as TT_n. This state is necessary in order to explain the ESA transitions observed in the experimental results, as will be discussed later. We set $E_{TT_n} = 29478\,\mathrm{cm}^{-1}$, to fit the experimental spectra.

Overall, optical transitions are possible between the ground state, g, and the singlet state, S_1, as well as between the multiexciton state, TT, and the higher lying state TT_n. The dipole operator can thus be written as:

$$\mu = \left(\mu_{g,S_1} \left|S_1\right\rangle \left\langle g\right| + \mu_{TT,TT_n} \left|TT_n\right\rangle \left\langle TT\right|\right) + h.c. \tag{3.3}$$

where the transition dipole moments for $g \rightarrow S_1$ and $TT \rightarrow TT_n$ are denoted by μ_{g,S_1} and μ_{TT,TT_n} respectively. We take $\mu_{TT,TT_n} = 2.5 \times \mu_{g,S_1}$, following experimental and theoretical studies which suggest that transitions from TT to TT_n have strong dipole moments [26].

As discussed above, we include vibrational modes explicitly in our model, alongside the electronic states. Our choice of which modes to include is motivated by the experimental Raman spectra, shown in Fig. 3.9b, which exhibit strong oscillations at $\omega = 265$, 1170 and $1360\,\mathrm{cm}^{-1}$. The Hamiltonian for the modes reads:

$$H_M = \sum_k \omega_k \left(a_k^\dagger a_k + \frac{1}{2}\right) \tag{3.4}$$

where k is the mode index (k = 1, 2, 3 for $\omega = 265$, 1170 and 1360 cm^{-1} respectively), a_k and $a_k^\dagger$ are creation and annihilation operators for mode k and we have set $\hbar = 1$.

We write the interaction between the modes and the electronic states as:

$$H_I = \sum_i \sum_k g_{i,k} \left(a_k + a_k^\dagger \right) |i\rangle \langle i| \tag{3.5}$$

Here $g_{i,k}$ is the coupling between the kth mode and the ith electronic state, and is related to the Huang-Rhys factor S by $g = \sqrt{S}\omega$. Gisslen et al. [27] used density functional theory to obtain couplings to the singlet state of $g_{S_1,1} = \frac{0.7}{\sqrt{2}}$, $g_{S_1,2} = \frac{0.6}{\sqrt{2}}$ and $g_{S_1,3} = \frac{0.75}{\sqrt{2}}$. As far as we are aware, the equivalent mode couplings to the TT and TT_n states are not available in the literature. Therefore we set $g_{TT,k} = 0$ and $g_{TT_n,k} = g_{S_1,k}$, which fits well with the experimental results, although other values could also give a good fit. Overall, the total Hamiltonian is given by:

$$H = H_S + H_M + H_I \tag{3.6}$$

3.4.2 Eigenstates

Following the approach outlined in Chap. 2, we diagonalise the Hamiltonian to obtain the eigenstates. As described in Sect. 2.3.3, the eigenstates fall into three distinct manifolds: the ground state manifold, g, the excited state manifold, e, whose states are superpositions of S_1 and TT and the higher lying manifold, f, which represents the vibrational manifold of the higher lying TT_n state. The excited state manifold can be excited directly from the ground state, whereas the higher lying manifold can only be excited from the excited manifold via an ESA process. The eigenstates are illustrated in Fig. 3.12, which shows the bare electronic states with no electronic coupling (J = 0) on the left hand side. When a non-zero J is introduced, the states mix. The lowest eigenstates are still mainly composed of TT but now obtain a small singlet component, whilst the singlet state obtains some TT character.

The energies and dipole moments of the states are shown in Fig. 3.13. After electronic coupling is introduced, eigenstate 5 has the strongest dipole moment, with 86% singlet character and occurs at the energy of the main singlet transition in the linear absorption and 2D spectra (1.83 eV). The lowest energy eigenstate (eigenstate 1) has over 95% TT character; nonetheless its singlet state component allows it to obtain a small but significant dipole moment (approximately one third of eigenstate 5's dipole moment). Note that this dipole moment is still too small to enable it to be detected in the linear absorption spectrum. To illustrate this, in Fig. 3.14 we plot the experimental linear absorption spectrum alongside the dipole moments and oscillator strengths for the eigenstates calculated from our model. We also observe significant changes to the eigenstates above the main singlet energy when coupling between the

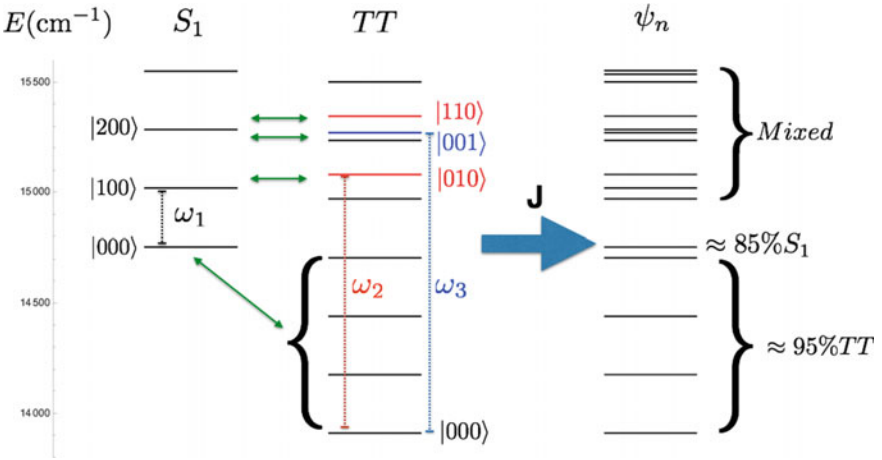

Fig. 3.12 *Left* The eigenstates of the excited state manifold for J= 0. The vibrational states are labelled by $|n_1, n_2, n_3\rangle$, where n_1, n_2 and n_3 refer to the number of quanta in the 265, 1170 and 1360 cm^{-1} modes, respectively. The vibrationally excited TT states are energetically close to the excited singlet states. *Right* The states mix when a non-zero electronic coupling is introduced [2]

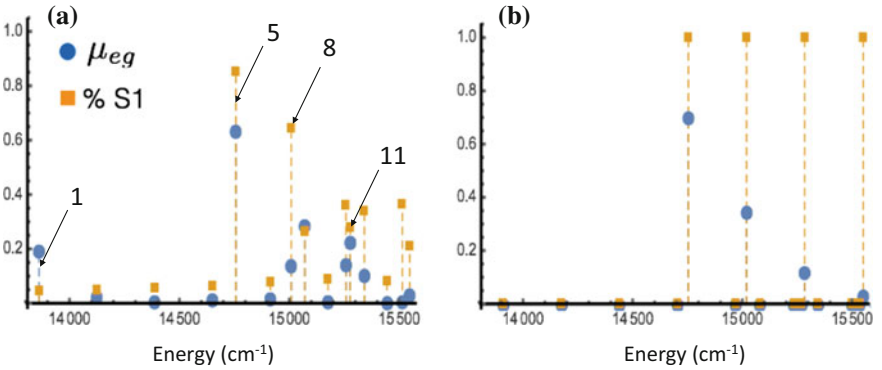

Fig. 3.13 **a** Dipole moments (*blue circles*) and fraction of S_1 (*yellow squares*) for the lowest energy eigenstates in our model. Certain important eigenstates are numbered. **b** The same as (**a**) for J= 0 [2]

states is introduced. Most importantly, eigenstates which are mainly composed of TT with one vibrational quantum of 1170 or 1360 cm^{-1} (eigenstates 8 and 11) gain significant dipole moments due to mixing with excited singlet states.

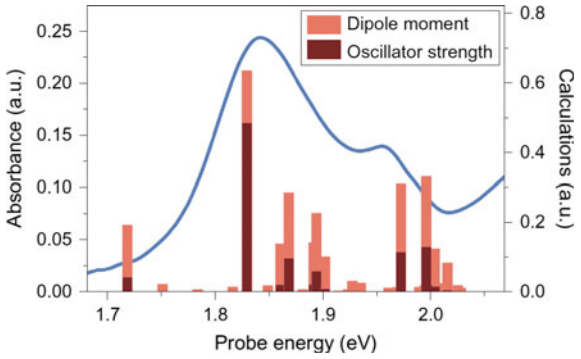

Fig. 3.14 Experimental linear absorption spectrum for pentacene (*blue line*), shown alongside the dipole moments and oscillator strengths of the eigenstates calculated from our model [2]

3.5 Ultrafast Dynamics

In order to calculate the ultrafast dynamics of our theoretical model we consider weak coupling to a harmonic bath described by multilevel Bloch-Redfield theory [28]. Here we do not make the secular approximation, since work has shown that this gives more accurate results [28, 29]. The bath is characterized by the Ohmic spectral function [28]:

$$J_s(\omega) = \eta\omega \exp(-\omega/\omega_c) \tag{3.7}$$

where $\eta = 0.3$ and the cut-off frequency $\omega_c = 800\ \text{cm}^{-1}$. The bath couples to the three vibrational modes in our model which were described above. The experiments were carried out at room temperature, hence in our simulations of the dynamics the system is initially in the ground state with a thermal distribution of vibrational states. The system is excited with a laser pulse with a Gaussian envelope of 13 fs duration and a carrier frequency of 1.8 eV.

Figure 3.15 plots the total populations of S_1 and TT over time. The relaxation parameters chosen above ensure that the singlet state decays on an 83 fs timescale, which matches the experimentally determined timescale for singlet fission. The populations of individual eigenstates over time are shown in Fig. 3.16.

The oscillations observed in Fig. 3.15 suggest that coherent motion has been created in the excited states. To investigate further, coherences between certain individual eigenstates are shown in Fig. 3.17. On the left, we plot coherences between eigenstates mainly on S_1 and TT. For example, eigenstate 1 is composed of 95% TT in the vibrational ground state whilst eigenstate 5 has 86% singlet character. The coherences between these eigenstates are short-lived due to the short lifetime of S_1 and hence oscillations at the energy difference between S_1 and TT are not observed experimentally. However, as shown on the right of Fig. 3.17, eigenstate 1 does form strong, long-lived coherences with eigenstates which are mainly composed of vibrationally excited TT states. Namely, eigenstates 2, 8 and 11 have strong contributions from vibrationally excited TT states, where the vibrational frequency is 265, 1170 and 1360 cm^{-1} respectively. Note that although the coherences all have strong ampli-

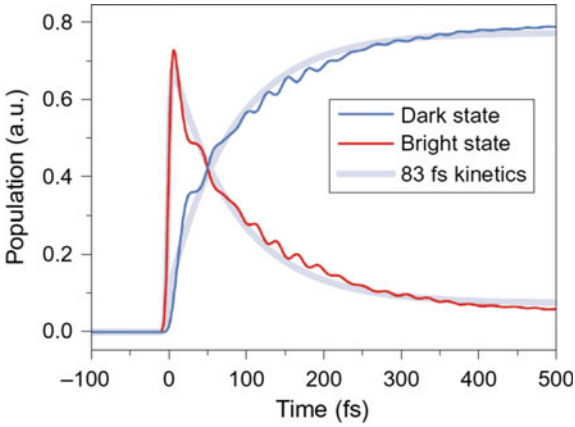

Fig. 3.15 Population kinetics for the dark (TT) state and the bright singlet state calculated from our model. *Grey curves* indicate a 83 fs decay for comparison [2]

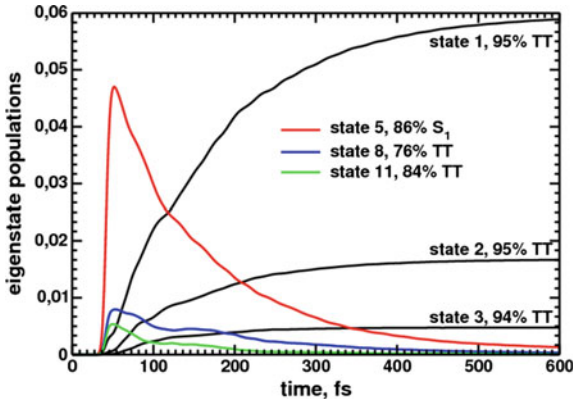

Fig. 3.16 Selected eigenstate populations over time [2]

tudes, the coherences involving vibrationally excited TT where the vibration has a high frequency (i.e. 1170 or 1360 cm^{-1}) are most likely to be observed in the 2D spectra. This is because the high frequency vibrationally excited TT states are energetically closer to the singlet state and thus couple more strongly and borrow stronger dipole moments.

In Fig. 3.15 we also observe that the TT state exhibits an initial fast rise. This offers an attractive alternative interpretation of the near instantaneous rise of a triplet feature observed by Chan et al. [21] using time-resolved two photon photoemission measurements and shown in Fig. 3.18a. Chan et al. proposed that this fast initial rise is due to strong electronic coupling between the singlet and a single degenerate dark multiexciton state. The signal then shifts to lower energies (by 0.11 eV) with a time constant of 200 fs, which Chan et al. attributed to dephasing and relaxation processes leading to the formation of free triplet pairs.

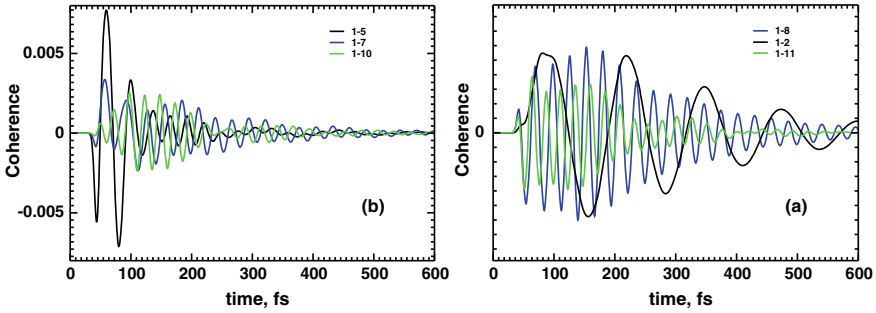

Fig. 3.17 *Left* Coherences between eigenstates involving the S_1 and TT states over time. *Right* Coherences between eigenstates involving vibrationally excited TT states over time [2]

In contrast, our simulations show that the TT state can rise quickly without needing to invoke strong electronic coupling with the singlet state. By inspecting the individual eigenstates' populations in Fig. 3.16, we observe that eigenstates 8 and 11 both grow at almost the same rate as the main singlet state (eigenstate 5). These eigenstates are composed of 76% and 84% TT respectively and have strong contributions from high frequency vibrations (see Fig. 3.13). Their energies lie close to the singlet state and vibrationally excited singlet states (where the vibration has a frequency of 265 cm^{-1}), allowing them to mix with the singlet state and borrow significant dipole moment. Nonetheless, they decay at a slower rate than the main singlet excitation, which could explain the 200 fs decay observed by Chan et al. Therefore we suggest that they might be observing the ultrafast excitation of vibrationally excited TT states which couple to the bright singlet state and then decay on slower timescales, as illustrate in Fig. 3.18b. This process occurs alongside excitation of the bright singlet state, in contrast to Chan et al.'s suggestion that an electronic coherence of the singlet and TT states is excited, which would require very strong electronic coupling between S_1 and TT.

3.6 Simulation of Beating Maps

As discussed in Chap. 2, in the limit of infinitely short laser pulses and within a perturbative description of the light-matter interaction, the 2DES signals can be expressed using the third-order response functions. We used this approach to simulate the experimental beating maps in Fig. 3.10, from the eigenstates described in Sect. 3.4.2. To do this, we computed the positions and dipole moments of all possible peaks which can arise from these eigenstates, including from the GSB, SE and ESA contributions (which were illustrated in Fig. 2.11). If dissipation is neglected, the magnitude of each peak is given by the product of the dipole moments of the transitions involved in the corresponding Feynman diagram. To account for dephasing and relaxation

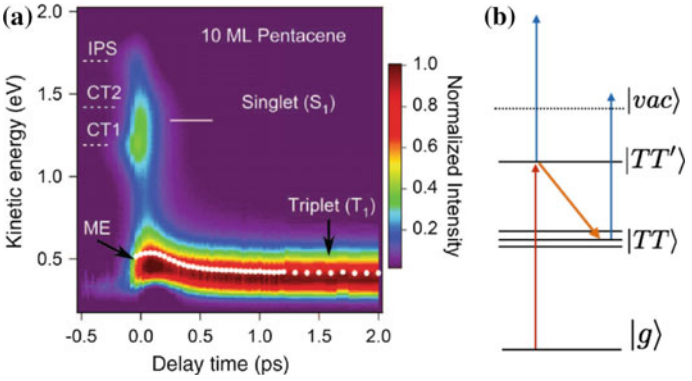

Fig. 3.18 **a** Time resolved two photon photoemission spectrum for a pentacene/C_{60} bilayer system. The *white circles* show the fast rise and subsequent decay of the multiexcitonic (ME)/triplet signal. This part of the figure is from [21], reprinted with permission from AAAS. **b** Proposed mechanism: Vibrationally excited TT states (TT') borrow significant dipole moment from the singlet and can therefore be excited on an ultrafast timescale. These states then decay to TT on a longer timescale [2]

in the waiting time assuming Markovian dephasing, we used Lorentzian lineshapes with dephasing rates estimated from the Redfield dynamics discussed in the previous section.

As will be discussed below, transitions between certain states lie outside of the laser spectrum (for example the transition between the ground state and vibrationally excited singlet states with high vibrational frequencies of 1170 or 1360 cm^{-1}). Therefore the dipole moments of peaks which contained transitions outside of the range $12950 - 15800\ cm^{-1}$ were set to zero. We consider the initial thermal population of vibrationally excited ground states to be negligible and we use 10, 5 and 5 harmonic oscillator levels for the vibrations with $\omega = 265$, 1170 and 1360 cm^{-1} respectively, which ensures convergence of the results. Finally, to approximate the effect of static disorder, a Gaussian convolution was applied to the beating maps with a standard deviation of 75 cm^{-1}. This is deliberately rather conservative so that the precise locations of the peaks are still visible. A better agreement with the experimental results could be obtained by taking a larger value.

3.7 Discussion of Beating Maps

Figure 3.19 shows the rephasing and non-rephasing beating maps obtained both experimentally (left) and from our simulations (right) (the experimental results were shown before in Fig. 3.10 but are reproduced here for convenience). The qualitative agreement between the experimental and simulated maps is very good. In this section I will discuss how the peaks in the maps arise from the eigenstates of our vibronic model.

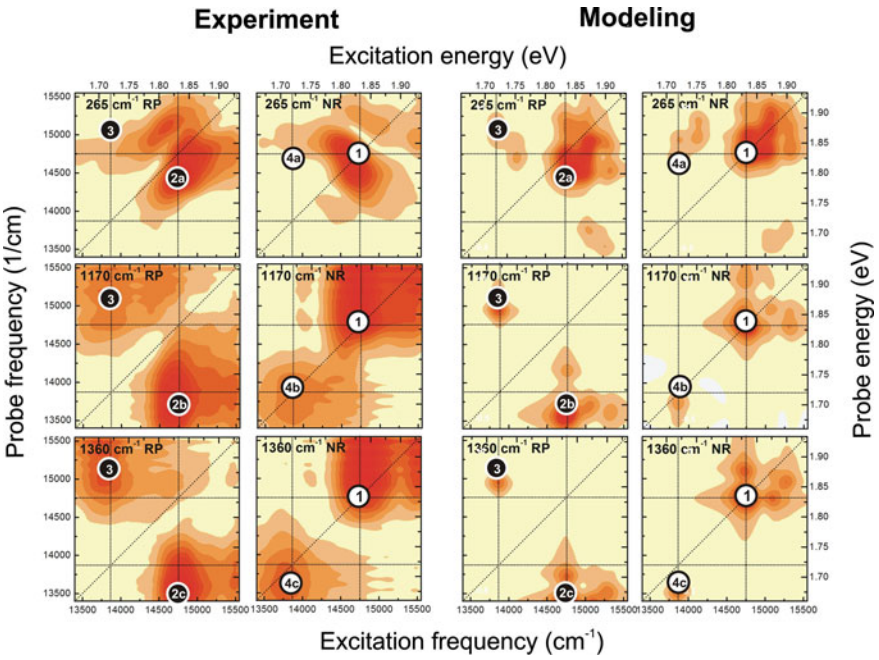

Fig. 3.19 Experimental and simulated beating maps [2]

Whilst all of the GSB, SE and ESA contributions are taken into account in the simulations, the peaks observed in the beating maps can be assigned to either GSB or ESA contributions. This is because SE contributions to the signal are weak, due to the fast (<100 fs) decay of the bright singlet eigenstates and the relatively weaker dipole moments of the states with predominantly TT character. In all of the beating maps, significant GSB of the bright singlet state (eigenstate 5) is observed at $\omega_\tau = 1.83$ eV. This is the origin of peaks 1, 2a, 2b and 2c and the Feynman diagrams for these peaks are shown in Fig. 3.20 (labelled 1 and 2 respectively). Note that the GSB peaks in the rephasing map (peaks 2a, 2b and 2c) have the same excitation frequency as their non-rephasing counterpart (peak 1), but are located at lower probe frequencies, with the shift equal to the beating map frequency. For example, peak 2c is shifted down from the singlet state energy by 1360 cm^{-1}. Meanwhile the position of peak 1 is the same in all of the beating maps and is given directly by the energy of the singlet state. These energy shifts can be understood by inspecting the energy differences between the final two states in the Feynman diagrams in Fig. 3.20. Specifically, in Feynman diagram 1, the final stimulated emission goes from S_1 to g, whilst in Feynman diagram 2 the final stimulated emission goes from S_1 to the vibrationally excited ground state, g'.

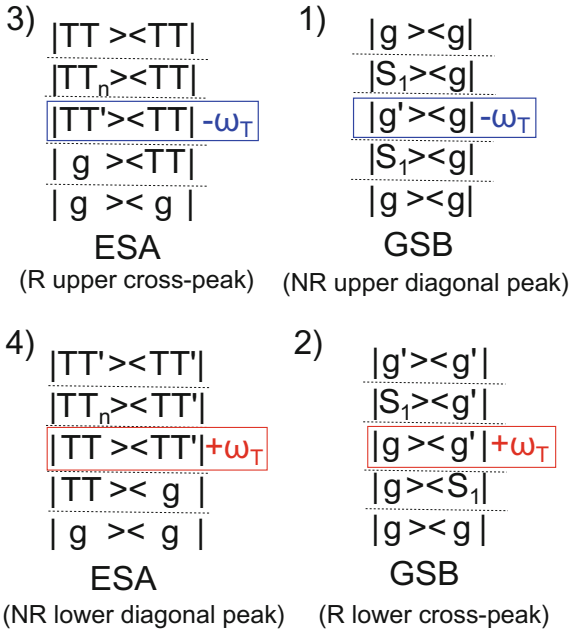

Fig. 3.20 Feynman diagrams corresponding to the peaks labelled in Fig. 3.22. The upper diagonal peak and upper cross-peak oscillate at $-\omega_T$, whilst the lower diagonal peak and lower cross-peak oscillate at $+\omega_T$, as observed in Fig. 3.23 [2]

Note that a diagonal GSB peak might be expected at the singlet state energy in the 1170 and 1360 cm^{-1} rephasing beating maps, originating from the Feynman diagram shown in Fig. 3.21a. However this signal requires a transition from the ground state to the vibrationally excited singlet state, which lies outside of the finite laser spectrum bandwidth when the vibrational frequency is 1170 or 1360 cm^{-1}, as illustrated in Fig. 3.21b. Therefore from our simulations we do not expect this peak to be observed, in agreement with the experimental results. In contrast, in the lower frequency 265 cm^{-1} beating map this GSB contribution is expected and lies 265 cm^{-1} above peak 2a (the proximity of these peaks makes them difficult to distinguish).

Peaks are also observed at the excitation frequency of the lowest energy eigenstate (eigenstate 1, which has 95% TT character), labelled 3, 4a, 4b and 4c in Fig. 3.19. These peaks are particularly strong in the 1170 and 1360 cm^{-1} beating maps. We assign them to ESA, with initial excitation from the ground state to TT, followed by ESA from TT to TT_n. The corresponding Feynman diagrams are shown in Fig. 3.20. We are able to resolve these signals despite the very weak initial excitation to the lowest energy eigenstate for three reasons. Firstly, the ESA transition from TT to TT_n is known from previous experimental studies to be strong, which balances out the weaker initial excitation of TT. Secondly, as discussed above, the laser spectrum does not cover the transition from g to S_1', which removes some singlet GSB contributions which would otherwise be present. This means that the strength of the ESA of TT is enhanced with respect to singlet GSB. Note that in this way the laser spectrum can be chosen to selectively excite specific transitions and to resolve otherwise weak signals in the beating maps. Finally, as discussed above, the vibrationally excited

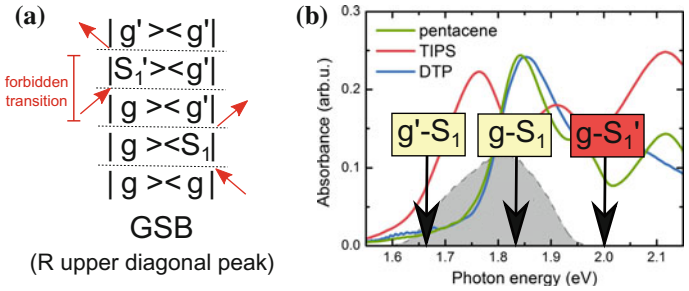

Fig. 3.21 **a** Additional singlet GSB Feynman diagram, not observed in the high frequency beating maps due to the forbidden g-S' transition. **b** Laser spectrum (*grey*) alongside the frequencies of the g-S, g'-S and g-S' transitions, where ' represents a vibrational quantum of 1360 cm^{-1}. The g-S' transition lies outside of the laser spectrum. Figure adapted from [2]

TT states are energetically close to the bright singlet state and are therefore able to borrow significant dipole moment. The last two of these points are only relevant for the high frequency vibrational modes, which explains why the peaks in the high frequency beating maps (peaks 4b and 4c) are stronger than the peak in the low frequency beating map (peak 4a).

Note that similarly to the GSB peak pattern described above, for ESA the Feynman diagrams in Fig. 3.20 also predict that the non-rephasing peak should be shifted down from the rephasing peak by the vibrational frequency of the beating map. We observe this pattern in the experimental results, where peak 3b appears 1170 cm^{-1} below peak 4, whilst peak 3c appears 1360 cm^{-1} below peak 4, further confirming our assignment of ESA.

3.8 Analysing the Oscillation Signs

During the waiting time, T, oscillations can occur with either positive or negative frequencies. Normally, the Fourier transform across the waiting time is applied to the real valued data only (as was done to obtain the beating maps discussed in the previous section, for example), which does not distinguish between oscillations with different signs. However, the sign of the oscillation frequency contains crucial information about whether the signals evolve on the ground or excited state during the waiting time [30–32].

In order to distinguish whether the sign of the oscillation frequency at a particular peak position is positive or negative, we take the Fourier transform of the complex valued data over the waiting time, T, according to:

$$\hat{f}(\omega_T) = \int_{-\infty}^{+\infty} dT f(T) e^{-i2\pi\omega_T T} \tag{3.8}$$

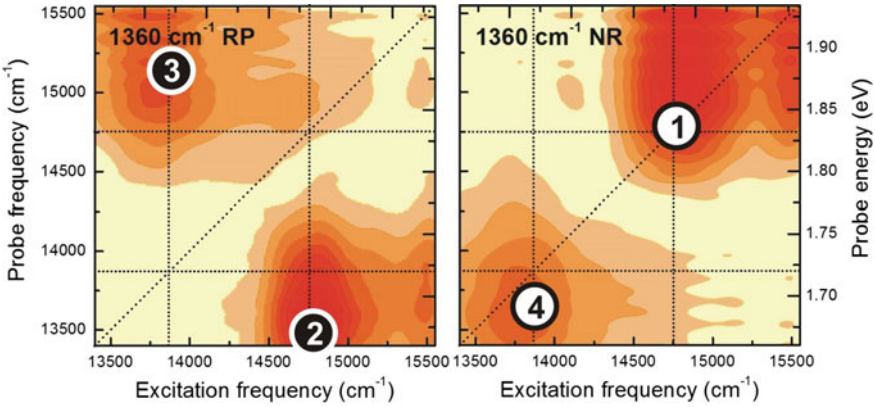

Fig. 3.22 Rephasing (*left*) and non-rephasing (*right*) beating maps at 1360 cm^{-1} [2]

where $f(T)$ is the complex valued signal at a specific point in the 2D spectrum (note that throughout the rest of this work the Fourier transform is taken over the real valued data). Using the complex valued data allows us to distinguish between positive and negative oscillation frequencies. In the Feynman diagrams, a positive frequency means that during the waiting time the state on the 'ket' side is at a lower energy than the state on the 'bra' side (e.g. $|g\rangle\langle g'|$, where $'$ denotes the vibration) and vice-versa for a negative frequency (e.g. $|g'\rangle\langle g|$) [30].

We consider four specific points in the 2D spectrum, which correspond to the positions of the four strongest peaks in the $\omega_T = 1360\,cm^{-1}$ beating maps, namely the points $(\omega_\tau, \omega_{t_d}) = (13870, 15015)\ cm^{-1}$ and $(14765, 13401)\ cm^{-1}$ in the rephasing spectrum and $(14765, 14762)\ cm^{-1}$ and $(13870, 13655)\ cm^{-1}$ in the non-rephasing spectrum. The 1360 cm^{-1} beating maps are shown for convenience in Fig. 3.22, with the points discussed above labelled from 1 to 4. The Fourier transforms of the complex valued 2D signal at these points over the waiting time are shown in Fig. 3.23.

From the Fourier transforms in Fig. 3.23, the rephasing upper cross-peak oscillates at $-1360\ cm^{-1}$, whilst the rephasing lower cross-peak oscillates at $+1360\ cm^{-1}$. The Feynman diagrams for the peaks were shown in Fig. 3.20. As observed experimentally, the sign of the oscillations is negative for the upper cross-peak (because the 'ket' state has a higher energy than the 'bra' state) and positive for the lower cross-peak. Note that if the upper cross-peak came from GSB, the sign of the oscillations would be positive and we would also observe a peak in the Fourier transform at $+1360cm^{-1}$. The absence of this peak means that we can unambiguously assign this signal to excited state coherences and rule out the possibility of significant GSB. Note that this does not exclude GSB if the system is initially in a vibrationally excited ground state, however for the high frequency modes at 1170 and 1360 cm^{-1} less than 0.3% of the signal is expected to lie in the first vibrationally excited ground state due to thermal fluctuations and so we neglect this contribution.

Similarly, from the Fourier transforms in Fig. 3.23 the non-rephasing upper diagonal peak oscillates at $-1360\ cm^{-1}$, whilst the non-rephasing lower (near) diagonal

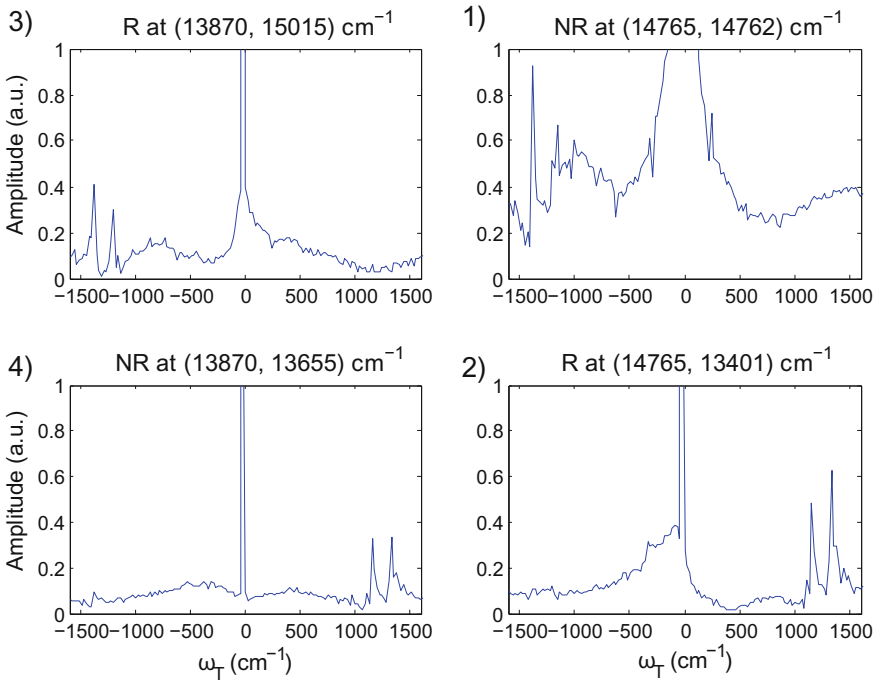

Fig. 3.23 Fourier transforms of the complex valued signals at the four points in the 2D spectrum labelled in Fig. 3.22. Points were chosen to match the experimental peak positions [2]

peak oscillates at $+1360$ cm^{-1}. Again, these signs match those predicted by the Feynman diagrams in Fig. 3.20, in agreement with our assignment that the upper diagonal peak arises from GSB, whereas the lower diagonal peak arises from excited state coherences.

Note that the Fourier transforms of the complex valued signals at the positions corresponding to the peaks in the 1170 cm^{-1} beating map show the same oscillation frequency signs as we observe in Fig. 3.23 for 1360 cm^{-1}. This is expected since the origins of the peaks (GSB and ESA) are the same in both the 1170 and 1360 cm^{-1} beating maps. In fact, peaks at 1170 cm^{-1} can also be observed in Fig. 3.23 due to the close proximity of the 1170 and 1360 cm^{-1} peaks in the beating maps.

3.9 Summary and Conclusions

In conclusion, we have applied 2DES to pentacene thin films and observed a manifold of mixed singlet and multiexcitonic states which mediate ultrafast singlet fission. This is the first direct evidence for the multiexcitonic TT state in pentacene, which

was previously believed to be 'dark' and is not observed in the linear absorption spectrum. A thorough analysis of the data confirms that we observe direct excitation of vibrational coherences on TT, followed by ESA to a higher lying triplet state. We observe the dark TT state due to the strength of the ESA transition from TT to TT_n, the width of the laser spectrum which reduces the magnitude of singlet GSB signals and mixing between vibrationally excited TT states and the bright singlet state. Inspired by this vibronic mixing, we propose a model of pentacene which incorporates vibrational and electronic states on an equal footing. By studying our model's eigenstates and computing the dynamics we reproduce both the ultrast fission timescale and the linear absorption spectrum. We also simulate the beating maps and obtain qualitatively similar peak positions to those observed experimentally (including the difference between rephasing and non-rephasing maps). All of these results are calculated from a single parameter set.

This work represents one of the most extensive analyses of 2DES data to date and contributes to a wider understanding of how to extract information from 2DES. In particular, we use the sign of the oscillation frequency to distinguish between ground and excited state coherences and to confirm that the signals with absorption at the low energy TT state evolve on the excited state during the waiting time. We also underline the importance of the laser spectrums width in determining which transitions can be excited and suggest that carefully selecting the laser spectrum's bandwidth offers a promising approach to resolving weak transitions. Both of the considerations above were essential in order to understand the origins of the peaks and to extract information about the underlying system's dynamics.

Most importantly however, this research highlights the role of vibrations in singlet fission. The mixed, vibrational states we observe can account for the ultrafast <100 fs fission dynamics without the need to invoke strong electronic coupling between the singlet and multiexciton states. Moreover, our model offers an alternative explanation for the fast initial rise of a triplet feature observed by Chan et al. [21], suggesting that the signal might originate from vibrationally excited TT states. The importance of vibrations is emerging as a key theme in a wide range of complex organic and biological systems and our work further strengthens this trend. For example, recently Musser et al. [33] proposed that conical intersection dynamics mediate fission in TIPS-pentacene. More detailed experimental and computational studies of the role of specific modes in fission are now required and our work suggests that 2DES could provide further insights. One promising avenue for future research is to apply 2DES to pentacene dimers in solution, where the slower fission rate means that the process can be followed with higher temporal resolution. In addition, the reduced size of this system means that ab initio methods can be used to explicitly assign modes which are involved in the fission process and to investigate their symmetry and couplings. Finally, the theoretical framework developed here could also be applied to study the appearance of quantum coherences in biological systems, where there is growing evidence that vibrations have non-trivial effects [34–38]. Untangling the

complex interplay between electronic and vibrational effects in these materials offers unique opportunities to understand their light harvesting mechanisms and ultimately to propose new molecules with superior properties.

References

1. Hanna, M.C., Nozik, A.J.: Solar conversion efficiency of photovoltaic and photoelectrolysis cells with carrier multiplication absorbers. J. Appl. Phys. **100**, 074510 (2006)
2. Bakulin, A.A., Morgan, S.E., Kehoe, T.B., Wilson, M.W.B., Chin, A.W., Zigmantas, D., Egorova, D., Rao, A.: Real-time observation of multiexcitonic states in ultrafast singlet fission using coherent 2D electronic spectroscopy. Nat. Chem. **8**, 16–23 (2016)
3. Wang, C., Dong, H., Hu, W., Liu, Y., Zhu, D.: Semiconducting π-conjugated systems in field-effect transistors: a material odyssey of organic electronics. Chem. Rev. **112**, 2208–2267 (2012)
4. MacGillivray, L.: On substituents, steering, and stacking to control properties of the organic solid state. Cryst. Eng. Commun. **6**, 77–78 (2004)
5. Saeed, Y., Zhao, K., Singh, N., Li, R., Anthony, J., Amassian, A., Schwingenschlögl, U.: Influence of substitution on the optical properties of functionalized pentacene monomers and crystals: experiment and theory. Chem. Phys. Lett. **585**, 95–100 (2013)
6. Anthony, J.E., Eaton, D.L., Parkin, S.R.: A road map to stable, soluble, easily crystallized pentacene derivatives. Org. Lett. **4**, 15–18 (2001)
7. Yost, S.R., Lee, J., Wilson, M.W.B., Wu, T., McMahon, D.P., Parkhurst, R.R., Thompson, N.J., Congreve, D.N., Rao, A., Johnson, K., Sfeir, M.Y., Bawendi, M.G., Swager, T.M., Friend, R.H., Baldo, M.A., Voorhis, T.V.: A transferable model for singlet-fission kinetics. Nat. Chem. **6**, 492–497 (2014)
8. ChemSpider. CSID:10814431 (2015). http://www.chemspider.com/Chemical-Structure.10814431.html
9. ChemSpider. CSID:28580083 (2015). http://www.chemspider.com/Chemical-Structure.28580083.html
10. Smith, M.B., Michl, J.: Singlet fission. Chem. Rev. **110**, 6891–6936 (2010)
11. Nozik, A.J. Multiple exciton generation in semiconductor quantum dots. Chem. Phys. Lett. **457**, 3–11 (2008)
12. Wilson, M., Rao, A., Clark, J., Sai Santosh Kumar, R., Brida, D., Cerullo, G., Friend, R.: Ultrafast dynamics of exciton fission in polycrystalline pentacene. J. Am. Chem. Soc. **133**, 11830–11833 (2011)
13. Chan, W.-L., Ligges, M., Zhu, X.-Y. The energy barrier in singlet fission can be overcome through coherent coupling and entropic gain. Nat. Chem. **4**, 840–845 (2012)
14. Walker, B.J., Musser, A.J., Beljonne, D., Friend, R.H.: Singlet exciton fission in solution. Nat. Chem. **5**, 1019–1024 (2013)
15. Zirzlmeier, J., Lehnherr, D., Coto, P.B., Chernick, E.T., Casillas, R., Basel, B.S., Thoss, M., Tykwinski, R.R., Guldi, D.M.: Singlet fission in pentacene dimers. Proc. Natl. Acad. Sci. **112**, 5325–5330 (2015)
16. Merrifield, R.E., Avakian, P., Groff, R.P.: Fission of singlet excitons into pairs of triplet excitons in tetracene crystals. Chem. Phys. Lett. **3**, 386–388 (1969)
17. Beljonne, D., Yamagata, H., Brédas, J.L., Spano, F.C., Olivier, Y.: Charge-transfer excitations steer the Davydov splitting and mediate singlet exciton fission in pentacene. Phys. Rev. Lett. **110**, 226402 (2013)
18. Berkelbach, T.C., Hybertsen, M.S., Reichman, D.R.: Microscopic theory of singlet exciton fission. III. Crystalline pentacene. J. Chem. Phys. **141**, 074705 (2014)
19. Smith, M.B., Michl, J.: Recent advances in singlet fission. Annu. Rev. Phys. Chem. **64**, 361–386 (2013)

20. Král, K.: A note on triplet-triplet fission of singlet excitons in molecular crystals. J. Phys. B **22**, 566 (1972)
21. Chan, W.-L., Ligges, M., Jailaubekov, A., Kaake, L., Miaja-Avila, L., Zhu, X.-Y. Observing the multiexciton state in singlet fission and ensuing ultrafast multielectron transfer. Science **334**, 1541–1545 (2011)
22. Johnson, J.C., Nozik, A.J., Michl, J.: The role of chromophore coupling in singlet fission. Acc. Chem. Res. **46**, 1290–1299 (2013)
23. Zimmerman, P.M., Zhang, Z., Musgrave, C.B.: Singlet fission in pentacene through multi-exciton quantum states. Nat. Chem. **2**, 648–652 (2010)
24. Alguire, E.C., Subotnik, J.E., Damrauer, N.H.: Exploring non-Condon effects in a covalent tetracene dimer: How important are vibrations in determining the electronic coupling for singlet fission? J. Phys. Chem. A **119**, 299–311 (2015)
25. Bayliss, S.L., Chepelianskii, A.D., Sepe, A., Walker, B.J., Ehrler, B., Bruzek, M.J., Anthony, J.E., Greenham, N.C.: Geminate and nongeminate recombination of triplet excitons formed by singlet fission. Phys. Rev. Lett. **112**, 238701 (2014)
26. Wilson, M.W.B., Rao, A., Ehrler, B., Friend, R.H.: Singlet exciton fission in polycrystalline pentacene: from photophysics toward devices. Acc. Chem. Res. **46**, 1330–1338 (2013)
27. Gisslen, L.: Influence of Frenkel excitons and charge transfer states on the spectroscopic properties of organic molecular crystals. Ph.D. thesis, Technische Universität München (2009)
28. Egorova, D., Thoss, M., Domcke, W., Wang, H.: Modeling of ultrafast electron-transfer processes: validity of multilevel Redfield theory. J. Chem. Phys. **119**, 2761–2773 (2003)
29. Egorova, D., Kühl, A., Domcke, W.: Modeling of ultrafast electron-transfer dynamics: multi-level Redfield theory and validity of approximations. J. Chem. Phys. **268**, 105–120 (2001)
30. Seibt, J., Pullerits, T.: Beating signals in 2D spectroscopy: electronic or nuclear coherences? Application to a quantum dot model system. J. Phys. Chem. C **117**, 18728–18737 (2013)
31. Li, H., Bristow, A.D., Siemens, M.E., Moody, G., Cundiff, S.T.: Unraveling quantum pathways using optical 3D Fourier-transform spectroscopy. Nat. Commun. **4**, 1390 (2013)
32. Song, Y., Hellmann, C., Stingelin, N., Scholes, G.D.: The separation of vibrational coherence from ground- and excited-electronic states in P3HT film. J. Chem. Phys. **142**, 212410 (2015)
33. Musser, A.J., Liebel, M., Schnedermann, C., Wende, T., Kehoe, T.B., Rao, A., Kukura, P.: Evidence for conical intersection dynamics mediating ultrafast singlet exciton fission. Nat. Phys. **11**, 352–357 (2015)
34. Fassioli, F., Nazir, A., Olaya-Castro, A.: Quantum state tuning of energy transfer in a correlated environment. J. Phys. Chem. Lett. **1**, 2139–2143 (2010)
35. Christensson, N., Kauffmann, H.F., Pullerits, T., Mančal, T.: Origin of long-lived coherences in light-harvesting complexes. J. Phys. Chem. B **116**, 7449–7454 (2012)
36. Tiwari, V., Peters, W.K., Jonas, D.M.: Electronic resonance with anticorrelated pigment vibrations drives photosynthetic energy transfer outside the adiabatic framework. Proc. Natl. Acad. Sci. **110**, 1203–1208 (2013)
37. Chin, A., Prior, J., Rosenbach, R., Caycedo-Soler, F., Huelga, S., Plenio, M.: The role of non-equilibrium vibrational structures in electronic coherence and recoherence in pigment-protein complexes. Nat. Phys. **9**, 113–118 (2013)
38. Butkus, V., Zigmantas, D., Abramavicius, D., Valkunas, L.: Distinctive character of electronic and vibrational coherences in disordered molecular aggregates. Chem. Phys. Lett. **587**, 93–98 (2013)

Chapter 4
Time-Frequency Analysis for 2D Spectroscopy of PSII

What we observe is not nature itself, but nature exposed to our method of questioning.

Werner Heisenberg

Having shown the power of applying 2DES to pentacene, I now turn to biological light harvesting complexes. As discussed previously, recent 2DES experiments on a variety of light harvesting pigment protein complexes show long-lived oscillations (lasting for hundreds of femtoseconds), which have been suggested to arise from a mixture of electronic and vibrational origins [1–5]. Theoretical mechanisms for long-lasting, vibrationally enhanced electronic coherence have been proposed [2, 6, 7], including the suggestion that electronic coherences may be regenerated by the environment [7], as discussed in Chap. 1. One way to probe the 2DES data further and test these proposals is by using time-frequency analysis to obtain temporal information about the different frequency components of the signals. If electronic coherences are regenerated by the environment then a time-frequency analysis might be expected to show amplitude modulations of the 2DES signal over time [7]. However, modulations might also arise from interference between the multiple oscillation frequencies normally observed in 2DES of organic and biological systems. In this chapter I discuss the challenge of distinguishing between these two different types of signals, using 2DES experimental results for the biological light-harvesting system photosystem II (PSII) as an example.

I begin by describing the structure and function of PSII. I then introduce the technique of wavelet analysis, before showing that amplitude modulation and interference effects can produce identical time signals and hence identical wavelet analysis results. I examine how these signals might be distinguished by using additional information from the 2D spectra. Finally, in Sect. 4.3 I apply these ideas to 2DES data from PSII. The experimental results outlined in this section were obtained by Elisabet Romero and Rienk van Grondelle at VU University, Amsterdam and were published in 2014 [4]. Wavelet analysis of the PSII experimental data was originally

S.E. Morgan, *Ultrafast Quantum Effects and Vibrational Dynamics in Organic and Biological Systems*, Springer Theses, DOI 10.1007/978-3-319-63399-2_4

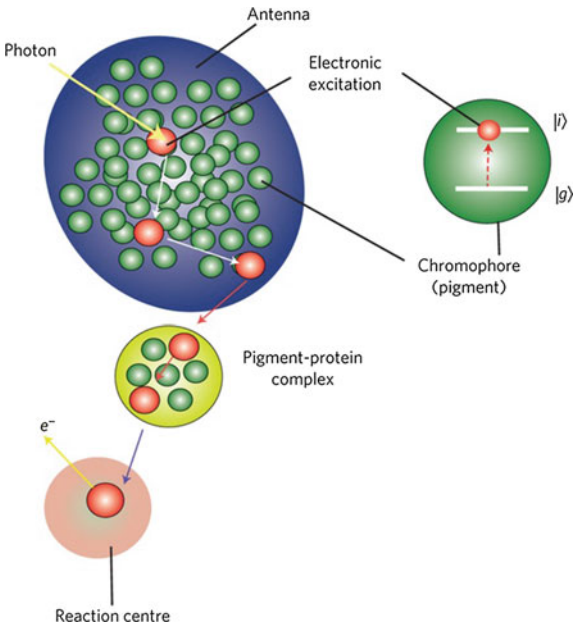

Fig. 4.1 The photosynthetic light reactions [7]

performed by Javier Prior and Alex Chin, although the plots shown here are from my own analysis. Some of the work in this chapter has been published as part of [35] .

4.1 Photosystem II

During photosynthesis, organisms use light from the sun to initiate charge separation. Firstly, photons are absorbed by molecules at the surface of the organism, creating an energy excitation (an exciton, as described in Chap. 2). This excitation then travels through a series of antenna complexes to the reaction centre (RC), which performs charge separation. Both the antenna complexes and the RC are examples of pigment-protein complexes (PPCs), which are large protein structures surrounding a number of optically active pigments. The RC separates the exciton into an electron and a hole before the electron is rapidly transferred away from the RC to avoid recombination. The processes described so far are called the light reactions and are illustrated in Fig. 4.1. Subsequent processes are called the dark reactions and use the resulting electrochemical gradient to produce stable high-energy molecules, which can power cellular processes [8].

Hence RCs play a crucial role in photosynthesis. Oxygenic photosynthesis requires two RCs: photosystem I (PSI), which reduces the organic molecule $NADP^+$ (Nicotinamide Adenine Dinucleotide Phosphate) and photosystem II (PSII), which oxidises water to form molecular oxygen [8]. Both of these complexes are found in the thakyloid membrane, which occurs in the chloroplast stroma in plants. Here I will focus on PSII rather than PSI. For completeness, I note that bacterial RCs (bRCs) also exist, which are evolutionary precursors to plant RCs and perform anoxygenic photosynthesis. The RCs of purple bacteria exhibit distinct similarities to PSII and have been the focus of many experimental and theoretical studies [8–11].

4.1.1 Structure

The PSII supercomplex is illustrated in Fig. 4.2 and shows the antenna complexes and the core complex, which contains the RC. The PSII RC itself is shown in Fig. 4.3. It consists of a number of optically active cofactors (or 'pigments'), which are surrounded by a protein structure (not shown). The RC proteins are known as D1 and D2. The cofactors include two strongly interacting chlorophyll-a molecules, P_{D1} and P_{D2}, another two chlorophyll-a molecules, Chl_{D1} and Chl_{D2}, two pheophytin-a molecules, $Pheo_{D1}$ and $Pheo_{D2}$ and two ubiquinones, Q_A and Q_B. These molecules are illustrated in Fig. 4.4. Note that this is a highly symmetric structure and the pigments are arranged on two sub-branches. One sub-branch is close to protein D1, while the other is close to protein D2, hence the pigment subscripts D1 and D2.

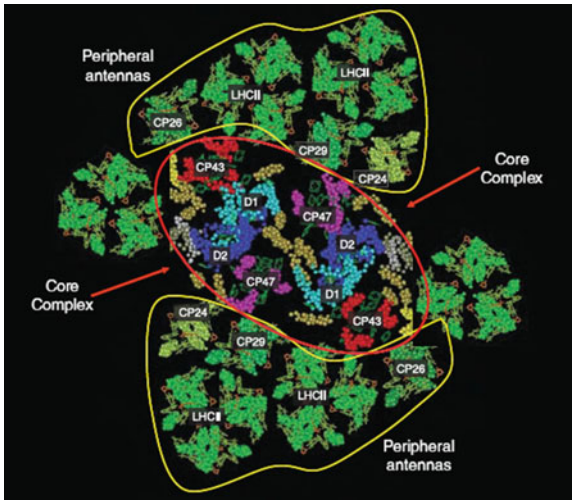

Fig. 4.2 Diagram of the PSII supercomplex, taken from [12]

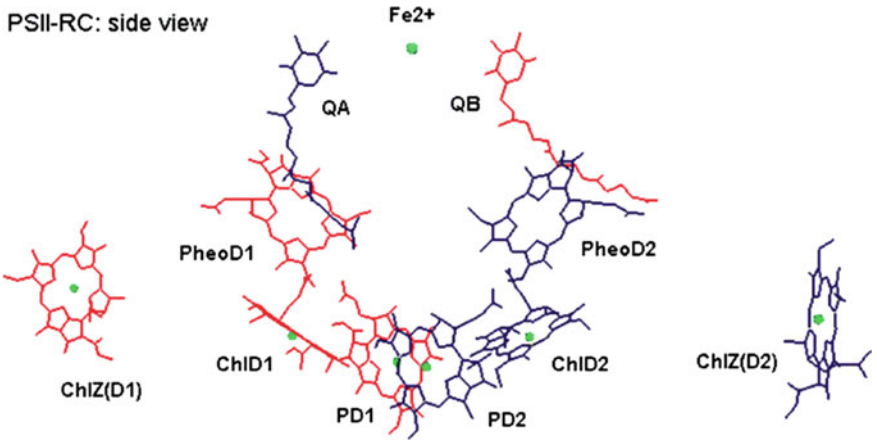

Fig. 4.3 PSII pigment arrangement. Adapted from [13] with permission of the PCCP Owner Societies

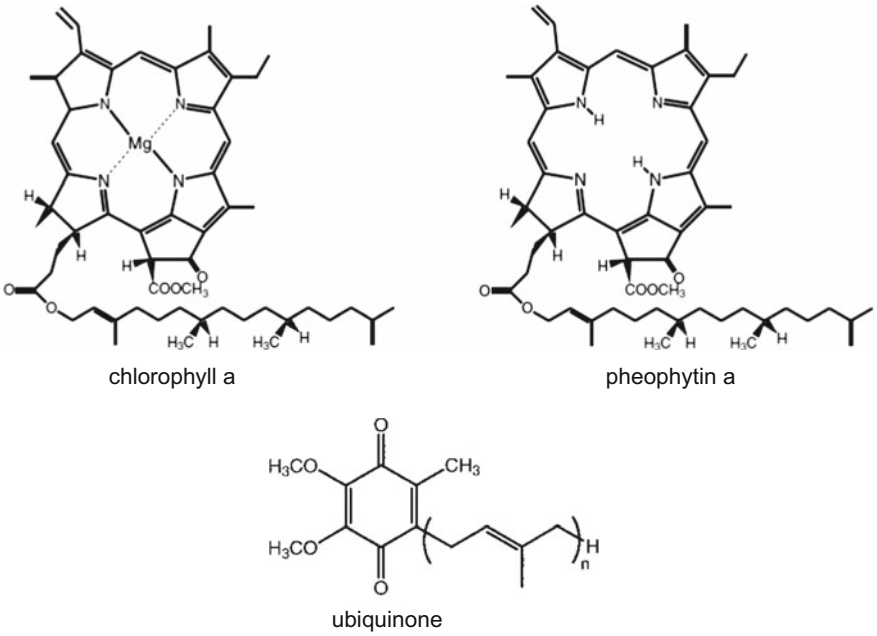

Fig. 4.4 Diagrams of the pigment molecules in the PSII reaction centre. Reproduced from [8] with permission from John Wiley & Sons, copyright 2014

4.1.2 Function

The function of RCs can be described in three phases: initial energy transfer to P_{D1} and P_{D2}, charge separation and subsequent electron transfer [8].

The P_{D1} and P_{D2} molecules exhibit electronic coupling of $\approx 85 - 140\ \text{cm}^{-1}$ [14] (unlike their counterparts in bRCs, which are more strongly coupled). This is weak enough to be comparable to the couplings between the other pigments, leading to a system of coupled pigments which interact to form excitons with strongly mixed pigment character. The initial energy excitation and transfer is therefore governed by highly delocalised excitonic states [15, 16]. Previous work suggests that transfer between these delocalised states can occur within 500 fs [17]. Charge separation can also involve a number of different states and is believed to take place within a few picoseconds after the initial excitation [18].

Following charge separation, the electron transfer steps are complicated by mixing of the excitonic and charge transfer states [15]. In 2010, Romero et al. used transient absorption spectroscopy alongside global and target analysis to propose the existence of two charge separation pathways in PSII [19]. Both paths ultimately lead to the state $P_{D1}^{+}Phe_{D1}^{-}$, where the electron has been transferred to the pheophytin on branch 1. In other words, there is an asymmetry between the two branches, because electron transfer (via either of the two pathways) only occurs along the D1 branch, often referred to as the 'active' branch [8]. The two pathways, denoted the Chl_{D1} path and the P_{D1} path, are illustrated in Fig. 4.5 and can be written as follows:
Chl_{D1} path:

$$(Chl_{D1}Phe_{D1})^{*} \rightarrow Chl_{D1}^{+}Phe_{D1}^{-} \rightarrow P_{D1}^{+}Phe_{D1}^{-} \tag{4.1}$$

P_{D1} path:

$$(P_{D1}P_{D2}Chl_{D1})^{*} \rightarrow P_{D2}^{+}P_{D1}^{-} \rightarrow P_{D1}^{+}Chl_{D1}^{-} \rightarrow P_{D1}^{+}Phe_{D1}^{-} \tag{4.2}$$

where * represents an excitonic state.

Romero et al. suggested that different pathways are favoured by different realisations of the disorder caused by slow protein fluctuations. However, the mechanisms behind the pathways and the role of the environment remain unclear. Recent work has suggested that quantum mechanical effects could be important for both the energy and electron transfer steps and might increase the efficiency of these processes [4, 5]. We note that the quantum yield of PSII can be as high as 90% [20], for example Croce et al. measured quantum efficiencies of 80–90% for charge separation in the PSII supercomplex from thylakoid membranes of *Arabidopsis thalianav* [21]. The overall energy efficiency is much lower and must take into account the light-harvesting and energy conversion efficiencies. For example Messinger and Shevela estimate a maximum energy efficiency of 16% for PSII [20]. This number will depend on the amount of light available to the organism and under full light the efficiency is often reduced in order to limit light-induced damage.

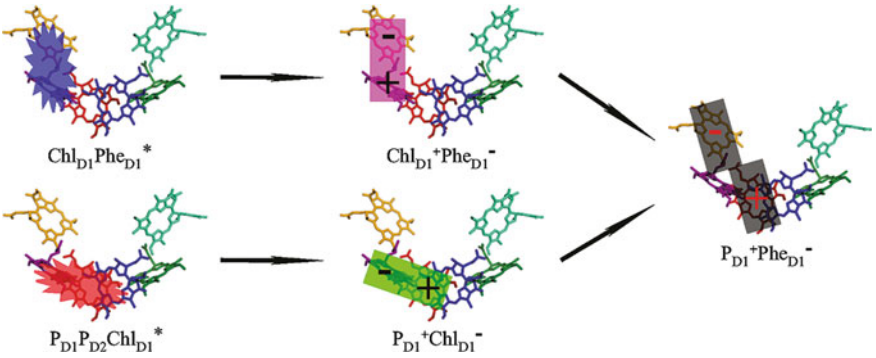

Fig. 4.5 Illustration of the two charge separation pathways in PSII. Reprinted with permission from [19]. Copyright 2010 American Chemical Society [19]

4.2 Wavelet Analysis

4.2.1 Wavelet Analysis Method

In many experimental techniques a signal is measured as a function of time. Often the Fourier transform of this signal is then taken in order to calculate the frequencies at which the signal oscillates. For example, in 2DES, the signal is normally recorded as a function of the waiting time, T. A final Fourier transform can then be taken to calculate the frequency at which the signal oscillates during the waiting time, leading to 'beating maps', as discussed in Sect. 2.3.2. These beating maps are extremely useful for identifying the origins of different 2D spectroscopy signals [3, 22, 23], as was shown in Chap. 3.

However, in taking the Fourier transform of the signal, information about the time dependence of the signal is lost in exchange for information about the frequency dependence. Ideally, it would be useful to not only know the frequencies at which the signal oscillates, but also the times at which those different frequencies of oscillation occur. Whilst it is never possible to have full information about both the time and frequency content of the signal due to Heisenberg's uncertainty principle, various time-frequency methods have been developed which enable a trade-off between the two components [24]. A full discussion of these methods is beyond the scope of this work and here I will focus on a particular type of time-frequency technique known as a continuous wavelet transform (CWT).

Prior et al. [25] suggested using a wavelet transform to extract time-frequency information from ultrafast optical spectroscopy and here I will outline how this method works. In brief, a small time-localised wave (a 'wavelet') is used to decompose a time signal into different frequency bands. Formally, the continuous wavelet

transform is defined as a convolution between the time signal f(t) and the wavelet functions, $\psi_{u,s}(t)$ [26]:

$$CWT_f(u,s) = \int_{-\infty}^{+\infty} f(t)\psi^*_{u,s}(t)dt \tag{4.3}$$

The wavelets are calculated from a 'mother wavelet function', by translating the mother wavelet by u and dilating it by the scale s, according to:

$$\psi_{u,s}(t) = \frac{1}{\sqrt{s}}\psi\left(\frac{t-u}{s}\right) \tag{4.4}$$

A number of mother wavelet functions can be used; popular choices include Gabor wavelets and Gaussian Morlet wavelets. Further details about the continuous wavelet transform method can be found in a number of textbooks, for example [26–28].

An illustration of the wavelet approach from Prior et al. [25] is shown in Fig. 4.6. Here time signals are calculated from the equation:

$$f(t) = \sum_{i=1}^{3} \sin(\omega_i t)\exp\left(-\frac{1}{2}\left(\frac{t-\mu_i}{\sigma_i}\right)^2\right) \tag{4.5}$$

with $\omega_1 = 20, \omega_2 = 50$ and $\omega_3 = 80$ (all times and frequencies are in arbitrary units). Plots on the left hand side of Fig. 4.6 are obtained using the parameters: $\mu_1 = 20$, $\mu_2 = 80$ and $\mu_3 = 170$, whilst for plots on the right hand side: $\mu_1 = 20$, $\mu_2 = 25$ and $\mu_3 = 170$. The two different time signals produce identical Fourier transforms. However, the wavelet approach is able to distinguish between the two time signals by providing additional information on the times at which oscillations with different frequencies occur.

Nonetheless, there are some known problems with the wavelet transform approach. In particular, even if oscillations at a certain frequency are present from the beginning of the time signal their magnitude may increase over an initial time period (giving the appearance that they 'grow in'). Also, artefacts may appear if the sampling rate of the signals is close to the Nyquist frequency. Finally, complications can arise in the wavelet results due to interference between oscillations at two different frequencies (related to 'beating' effects in the original time signals). This final point will be discussed further in the following section.

4.2.2 Distinguishing Amplitude Modulation from Interference Using Artificial Signals

2D spectra often contain contributions from vibrations and/or electronic coherences which oscillate with similar frequencies. Therefore it is important to be able to

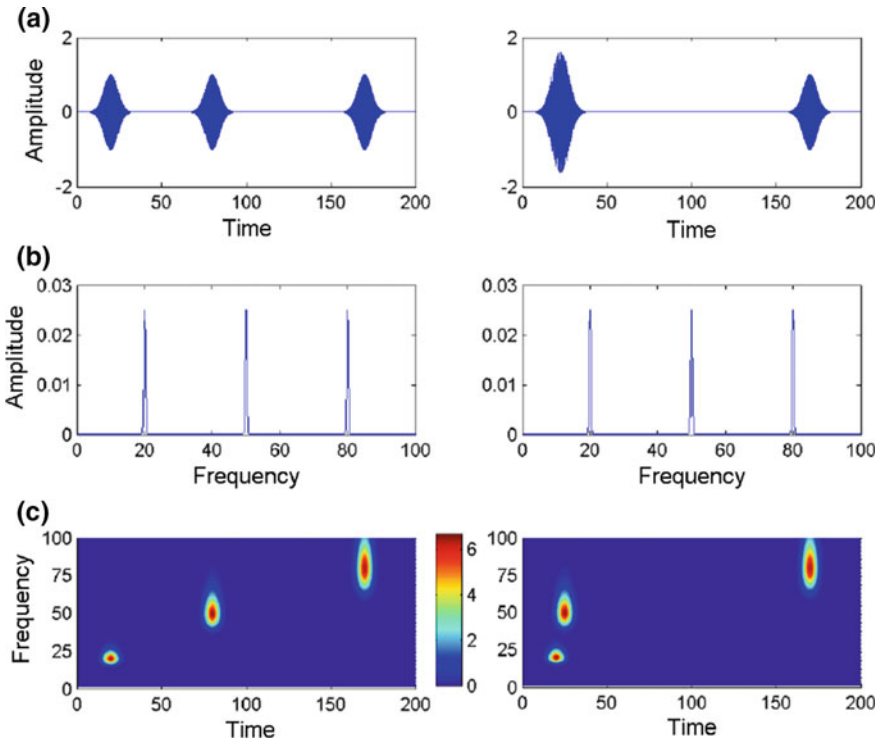

Fig. 4.6 Illustration of the wavelet method. *Top* Two different time signals, *Middle* Identical Fourier transforms, *Bottom* Wavelet transform results, which show the difference in the time at which the $\omega_2 = 50$ signal occurs in the two different signals. All times and frequencies are in arbitrary units. Figure reprinted from [25], with the permission of AIP publishing

distinguish signals which arise due to interference between multiple oscillations from signals where the amplitude is modulated due to some other effect, for example regeneration of electronic coherences. Here we investigate the differences between these two types of signals by considering two artificial signals, given by:

$$A_1(t) = \cos((\omega_c + \omega_m)t) + \cos((\omega_c - \omega_m)t) \tag{4.6}$$

$$A_2(t) = [A + \cos(\omega_m t)]\cos(\omega_c t) \tag{4.7}$$

where we take $\omega_c > \omega_m$. Equation 4.6 gives the superposition of two cosine oscillations at different frequencies, $\omega_c \pm \omega_m$ and represents the case where two oscillation frequencies interfere with each other. On the other hand, Eq. 4.7 simulates the effect of regeneration or transfer of a vibronic coherence: a cosine wave at frequency ω_c represents the vibronic coherence oscillation frequency, whose amplitude is modulated by a cosine wave with frequency ω_m.

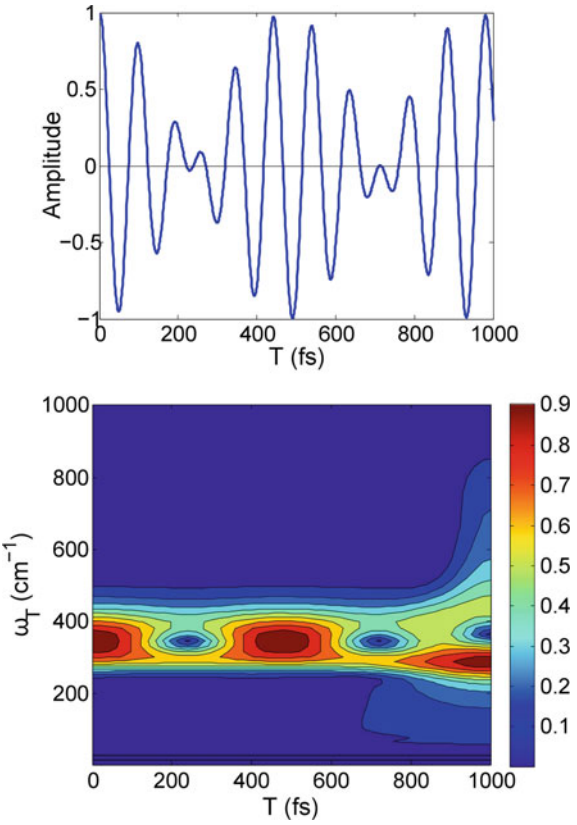

Fig. 4.7 *Top* $A_1(t)$ plotted for $\omega_c = 340\ \text{cm}^{-1}$ and $\omega_m = 35\ \text{cm}^{-1}$. *Bottom* Corresponding wavelet signal. Note that these plots are identical to those for $A_2(t)$ with A= 0

If A= 0, these signals are identical (up to a factor of two in the overall amplitude). They cannot therefore be distinguished from each other, including in a wavelet analysis. This underlines the heart of the problem, which is that the oscillation frequency amplitude modulation caused by regeneration of coherences over the waiting time, T, (Eq. 4.7) is in principle indistinguishable from the amplitude modulation caused by interference (or 'beating') between two closely spaced frequencies (Eq. 4.6). In Fig. 4.7 we show the time signal (analogous to the 2D spectral trace) and the wavelet pattern produced for either $A_1(t)$ or $A_2(t)$ (with A = 0), where $\omega_c = 340\ \text{cm}^{-1}$ and $\omega_m = 35\ \text{cm}^{-1}$, as an example of the type of pattern produced. To perform the wavelet analysis of the calculated time signals we use a Gabor wavelet of frequency 8, with 10 octaves and 15 voices per octave. The data is padded with reflections of the data to reduce boundary effects and the sample rate is 20 fs, which is similar to the sample rates used experimentally.

Note that for A= 0 we could also have written a more general, complex form of the equations above as follows:

$$A_3(t) = \exp(i(\omega_c + \omega_m)t) + \exp(i(\omega_c - \omega_m)t) \tag{4.8}$$

$$A_4(t) = \exp(i\omega_c t)\cos(\omega_m t) \tag{4.9}$$

Here both the real and imaginary parts of the signals are again identical (up to an arbitrary amplitude) and therefore cannot be distinguished. However, in practice it may be possible to distinguish between these types of signals by the context in which they occur, as will be explored below.

4.2.3 Waiting Time at Which the Oscillation Frequency Amplitude Modulation Occurs

For Eq. 4.6, the time at which the oscillation amplitude goes to zero due to interference effects is set by the difference between the two frequencies $\omega_c \pm \omega_m$, which is determined by ω_m in our case. Moreover, in practice the frequencies at which the amplitude of experimental 2D spectral signals oscillate are known (they are obtained by taking a Fourier transform of the 2D data over the waiting time). Therefore, the times at which recurrences due to interference between these frequencies are expected can be calculated. The fact that the observed period of amplitude modulation corresponds to the difference between two oscillation frequencies is therefore a strong indication that such modulation arises from interference effects.

For Eq. 4.7, the oscillation amplitude over the waiting time depends on both ω_m and A. Note that in the 2D beating maps the term A in Eq. 4.7 could be non-zero due to an additional long-lived vibrational coherence on the ground state (a GSB signal), which may occur at the same position in the 2D spectrum as a stimulated emission signal caused by a vibronic coherence. Due to the complexity of multichromophoric systems, the vibrational and vibronic features are expected to overlap in several positions in the 2D beating maps [29, 30]. As an aside we note that it may be possible to avoid this overlap if a specific polarisation sequence is applied in the 2DES experiment [31]. Figures 4.8 and 4.9 show the effect of changing the amplitude, A, on the time signals and the wavelet analysis, respectively. The results show that changing A determines whether the amplitude of oscillations falls to zero, the waiting times at which this occurs and the overall amplitude of the amplitude modulations. Overall, if the times at which the oscillation modulations occur correspond to the differences between known frequency values in the system then interference between those frequencies is the simplest explanation. If not, then an alternative explanation is required.

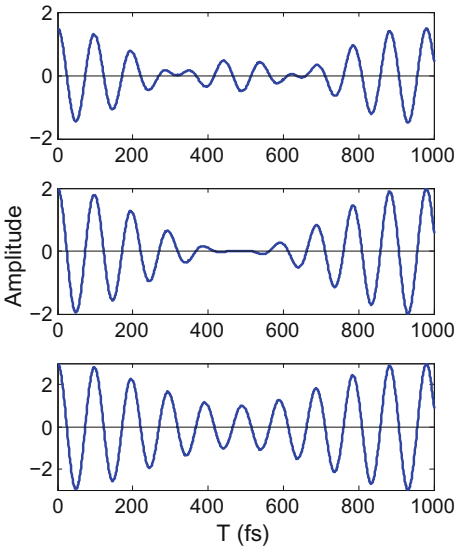

Fig. 4.8 $A_2(t)$ plotted for A= 0.5 (*top*), A= 1 (*centre*) and A= 2 (*bottom*)

4.2.4 Changing Position in the 2D Spectrum

Here we consider how the 2D wavelet traces vary as a function of the position $(\omega_\tau, \omega_{t_d})$ in the 2D beating maps. In the 2D spectra, the diagonal peaks are expected to contain a superposition of contributions which oscillate at different frequencies during the waiting time. However, the areas above and below the diagonal are less prone to spectral congestion. This creates a complicated pattern of interfering frequencies, which overlap with any additional dynamics due to energy transfer and modulations from the regeneration of vibronic coherences. For instance, the vibronic coherence between states A and B (absorbing at ω_A and ω_B, respectively, with $\omega_A > \omega_B$) appears in the $(\omega_A - \omega_B)$ beating map with a maximum amplitude at position (ω_A, ω_B). The weight of oscillations at this frequency will decrease when moving away from position (ω_A, ω_B). Using this rationale, here we investigate the effect of the varying contributions of different frequencies in the wavelet pattern (or wavelet traces) when moving away from a cross-peak maximum. For simplicity, we take a fixed ω_τ and vary ω_{t_d}.

Firstly, we consider signals arising from interference between two frequencies, as in Eq. 4.6, which can be generalised to:

$$A_1'(t) = \alpha \cos((\omega_c + \omega_m)t) + \beta \cos((\omega_c - \omega_m)t) \tag{4.10}$$

where we introduce α and β, which allow us to vary the weight of contributions from different oscillation frequencies. As the weighting of the two cosine waves changes, the amplitude of the pattern observed in the wavelets will shift to different ω_T, as shown in Fig. 4.10. However the waiting time at which the amplitude modulation

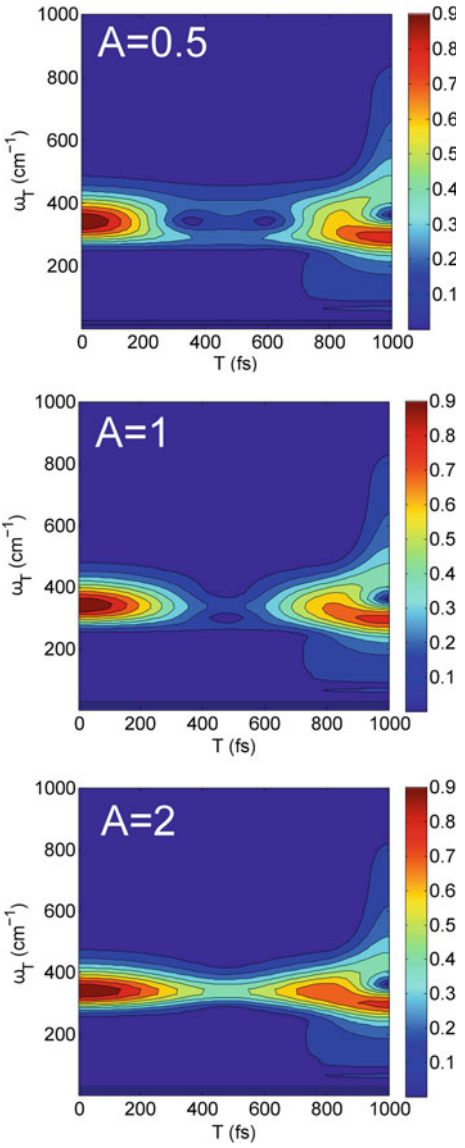

Fig. 4.9 Wavelet plots for $A_2(t)$, with A= 0.5 (*top*), A= 1 (*centre*) and A= 2 (*bottom*)

occurs remains the same (as determined by ω_m; see above). Therefore for signals caused by interference, the waiting time of the amplitude modulation is expected to remain the same for different ω_{t_d} values (which correspond to different relative contributions from oscillations with different frequencies). Also notice that interference between waves at two different frequencies can cause oscillations in the amplitude of the wavelet even if one of the amplitudes α or β is significantly larger than the other and it is not obvious from the wavelet results that two different frequencies

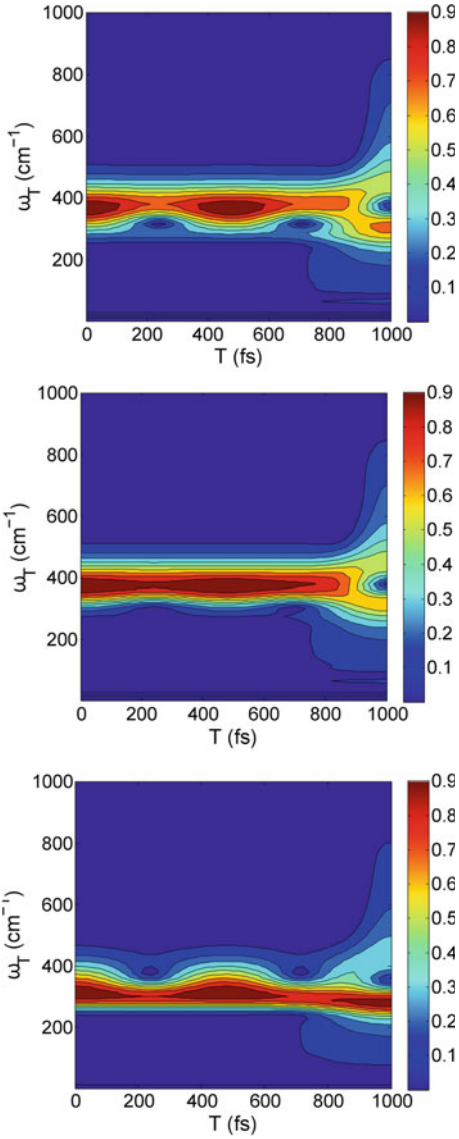

Fig. 4.10 Wavelet plots for $A_1'(t)$ with $\alpha = 0.9$ and $\beta = 0.1$ (*top*), $\alpha = 0.75$ and $\beta = 0.25$ (*centre*), $\alpha = 0.25$ and $\beta = 0.75$ (*bottom*). As before, $\omega_c = 340\text{cm}^{-1}$ and $\omega_m = 35\text{cm}^{-1}$

are involved. We note that for amplitude modulation of the type given by Eq. 4.7, changing ω_c will change the frequency (on the y axis) at which the pattern in the wavelets occurs but not the weighting of the pattern itself; see Fig. 4.11.

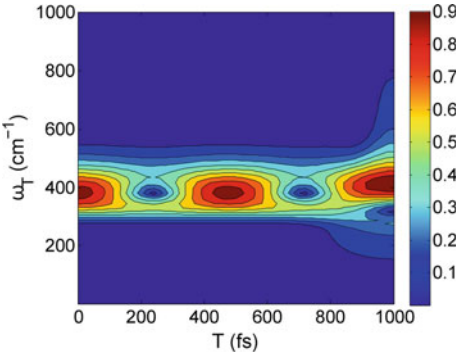

Fig. 4.11 Wavelet signal for Eq. 4.7 with $\omega_c = 380\,\mathrm{cm}^{-1}$, $\omega_m = 35\,\mathrm{cm}^{-1}$ and A= 0. The frequency on the y-axis shifts compared to Fig. 4.7, but the pattern over the waiting time is unchanged

4.3 Wavelet Analysis for PSII 2DES Data

4.3.1 Experimental Results

We will now apply some of the ideas above to wavelet results for PSII. As discussed in Sect. 4.1, PSII is one of the two reaction centres required for oxygenic photosynthesis. Recent 2DES experiments by both Romero et al. [4] and Fuller et al. [5] showed long-lived oscillations in PSII, lasting for at least 1 ps at 80K. Romero et al. also obtained similar results at room temperature, although in this chapter we will focus on the results at 80K. The Fourier transform of the real rephasing 2DES spectra obtained by Romero et al. [4] is shown in Fig. 4.12. Here the maximum amplitude of the Fourier transform across the whole 2D spectrum is plotted. Prominent oscillations

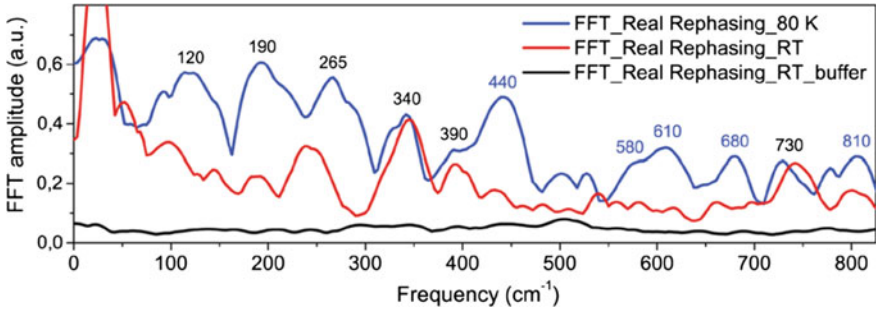

Fig. 4.12 Fourier transform of real rephasing 2DES spectra for PSII. At each frequency, the maximum amplitude across the 2DES spectra is plotted. Results are shown at 80K (*blue line*) and at room temperature (*red line*), alongside the results with only a buffer solution (*black line*). Figure taken from [4]

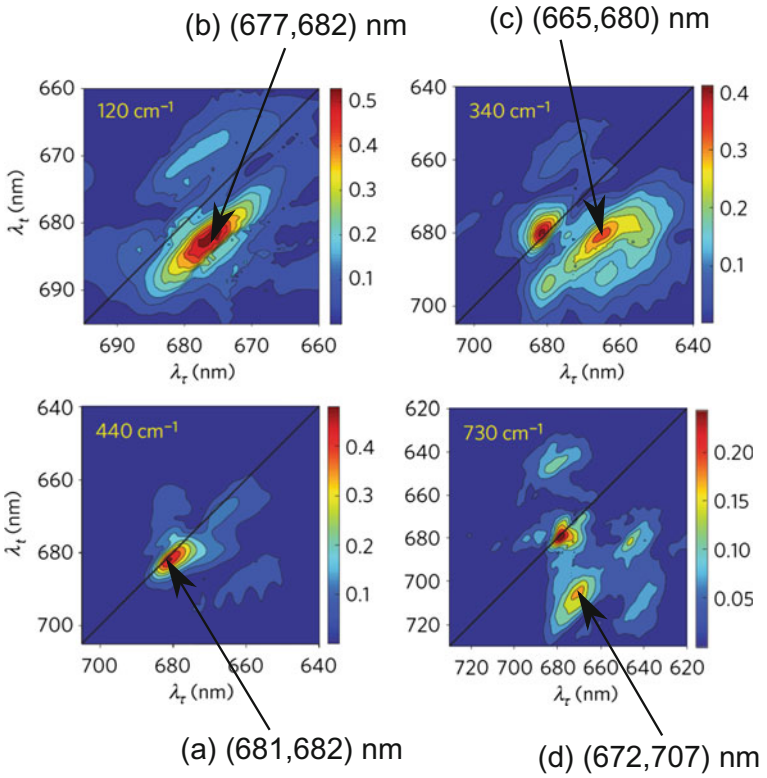

Fig. 4.13 PSII beating maps at four different frequencies, obtained at 80K. The positions shown in Fig. 4.14 are labelled. Figure adapted from [4]

are observed at 120, 340, 440 and 730 cm^{-1} and beating maps corresponding to those frequencies are shown in Fig. 4.13.

Plots of wavelets taken at the positions of the approximately diagonal peak at (681,682) nm, the cross-peak in the 120 cm^{-1} beating map at (677,682) nm, the cross-peak in the 340 cm^{-1} beating map at (665,680) nm and the cross-peak in the 730 cm^{-1} beating map at (672,707) nm are shown in Fig. 4.14. Again here only the real rephasing signals are considered.

4.3.2 Discussion

I begin by briefly reviewing the interpretation of the beating maps shown in Fig. 4.13 given by Romero et al. They assigned the oscillations at 120 cm^{-1} (observed in the 120 cm^{-1} beating map) as predominantly from electronic coherence between the $(P_{D2}^{\delta+}P_{D1}^{\delta-})^*$ state at $\approx$ 675nm and the $(Chl_{D1}^{\delta+}Phe_{D1}^{\delta-})^*$ state at $\approx$ 681nm. These

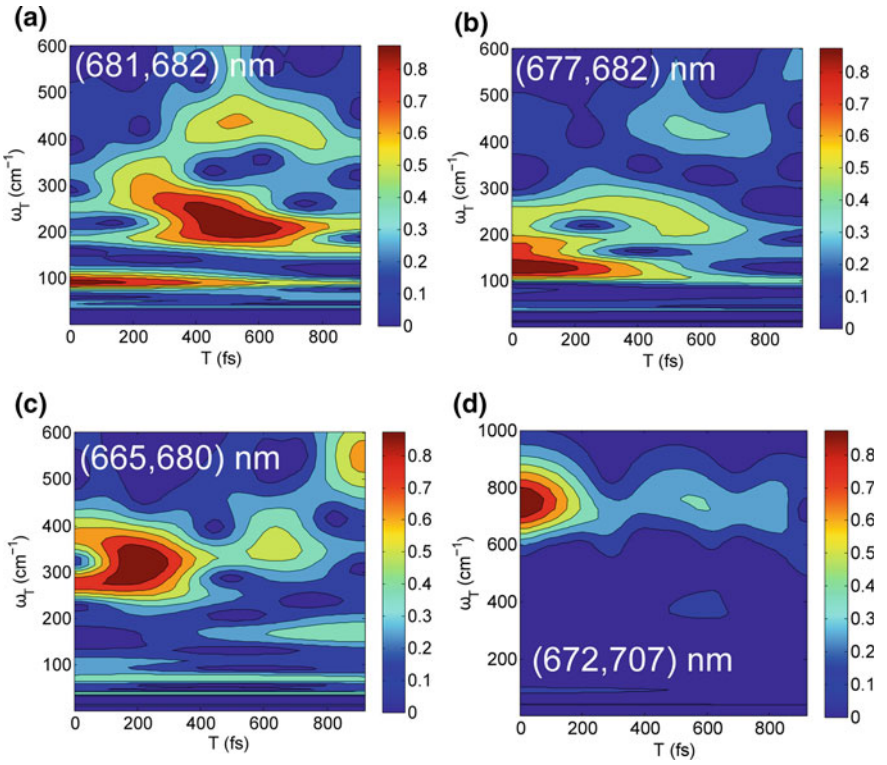

Fig. 4.14 **a** Wavelet plot for the main diagonal peak at (681,682) nm. **b** Wavelet plot for (677,682) nm, corresponding to the cross-peak in the 120 cm^{-1} beating map. **c** Wavelet plot for (665,680) nm, corresponding to the cross-peak in the 340 cm^{-1} beating map. **d** Wavelet plot for (672,707) nm, corresponding to the cross-peak in the 730 cm^{-1} beating map

mixed CT excitonic states belong to the P_{D1} and Chl_{D1} pathways respectively, which were discussed in Sect. 4.1 and are given by Eqs. 4.1 and 4.2. The energy difference between the two states is $\approx$ 120 cm^{-1}. There may also be some contribution to the 120 cm^{-1} oscillations from a resonant intra-molecular vibrational mode at the same frequency.

In the 440 cm^{-1} beating map the signal amplitude is mainly on the diagonal and the oscillations at this frequency are assigned to vibrational coherences. The 340 and 730 cm^{-1} beating maps exhibit patterns with five peaks, similar to those expected for vibrational signals [29], as was discussed in Chap. 2 and illustrated in Fig. 2.14. However, these frequencies are also close to energy differences between certain electronic states and Romero et al. propose that a full understanding of these beating maps requires electronic/vibrational mixing. For example, in the 340 cm^{-1} beating map the peak around (665,680) nm is brighter than would normally be expected for purely vibrational signals [29]. The first state in the P_{D1} pathway has both high and low energy components at around 660 and 673 nm (note that these energies are

subject to static disorder) and Romero et al. suggest that the (665,680) nm peak in the 340 cm^{-1} beating map is enhanced due to coherence between these states. This proposal is supported by simulations of the beating maps given in [32].

I now investigate the wavelet results for the 2DES data, in light of the difficulty of determining the origins of amplitude modulation, as discussed in Sect. 4.2. Firstly, it is important to note that the wavelet plot for the cross-peak in the 730 cm^{-1} beating map shows a pattern which arises from undersampling (the data is sampled at 20 fs intervals over the waiting time, compared to an oscillation period of 46 fs for the 730 cm^{-1} mode). Therefore these high frequency oscillations are excluded from any further analysis.

Interestingly, we do not observe any amplitude modulation of the oscillations which occur at a frequency of 120 cm^{-1} in any of the wavelet plots. This includes the wavelet analysis performed at (677,682) nm, which corresponds to the cross-peak in the 120 cm^{-1} beating map (see Fig. 4.14) and is believed to correspond to electronic coherence between the $(P_{D2}^{\delta+}P_{D1}^{\delta-})^*$ and $(Chl_{D1}^{\delta+}Phe_{D1}^{\delta-})^*$ states, as discussed above. Oscillations at this frequency have maximum amplitude at early waiting times and then decay over a long time period (taking over 600 fs to decay to half of the original amplitude).

A number of amplitude modulations can be observed at other frequencies in the wavelet plots. As discussed in Sect. 4.2.3, a good way to ascertain whether the amplitude modulations arise from interference between oscillations at two different frequencies is to check whether the period of the amplitude modulation matches the energy difference between those frequencies. For example, in both the (681,682) nm and (677,682) nm wavelet plots a peak is observed at around T= 500 fs, which could arise from interference between oscillations at 190 cm^{-1} and 265 cm^{-1}. The 75 cm^{-1} difference between these frequencies corresponds to a period of 445 fs. The way in which the peak at T = 500 fs separates into two components at 190 cm^{-1} and 265 cm^{-1} at early times also supports the suggestion that this amplitude modulation arises from interference between oscillations at 190 cm^{-1} and 265 cm^{-1}. Both of these frequencies match peaks in the fast Fourier transform of the real rephasing 2D spectral traces shown in Fig. 4.12. Similarly, the (681,682) nm and (677,682) nm wavelet plots both exhibit peaks at around T= 600 fs, which could arise from interference between oscillations at 390 cm^{-1} and 440 cm^{-1} since the 50 cm^{-1} difference between these two frequencies corresponds to a period of 667 fs (note that there may also be some contribution from oscillations at 340 cm^{-1}). In the (665,680) nm wavelet plot oscillations with a 400 fs period are observed, possibly due to interference between oscillations at 265 cm^{-1} and 340 cm^{-1}, which would be expected to exhibit a 445 fs period.

As discussed in Sect. 4.2.4, varying the position in the 2D spectrum can also help to determine whether amplitude modulations arise from interference between contributions which oscillate at different frequencies. In order to ascertain whether the amplitude modulation time, T, shifts with the emission frequency, ω_{t_d}, we therefore fix ω_τ and ω_T and plot ω_{t_d} against T. We take three different values of ω_τ: 681, 677 and 665 nm, corresponding to the absorption frequencies in Fig. 4.14 a, b and c. For ω_τ = 681 and 677 nm, we set ω_T = 225 and 440 cm^{-1}, since those are the waiting

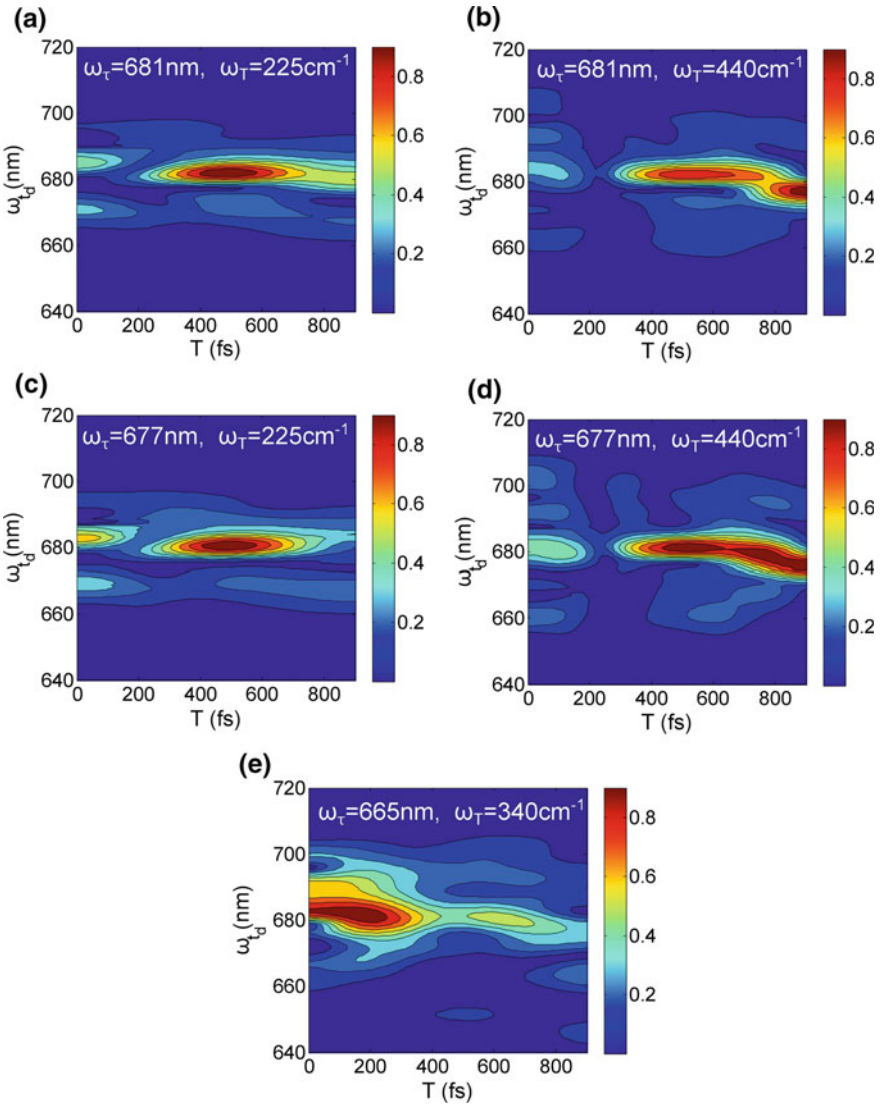

Fig. 4.15 Plot of ω_{t_d} against T for fixed ω_τ and ω_T for the PSII data

time frequencies at which the peaks occur in Fig. 4.14a and b. For $\omega_\tau = 665$ nm, we set $\omega_T = 340$ cm^{-1} for the same reason. The results are plotted in Fig. 4.15.

In parts a, c and e of Fig. 4.15, as ω_{t_d} changes, the waiting times at which the amplitude modulations occur remain fairly constant. For example, in Fig. 4.15a, the main peak in the amplitude occurs at around 500 fs, for both $\omega_{t_d} = 681$ nm and $\omega_{t_d} = 672$ nm. As discussed above, these modulations at constant waiting times are

as expected for interferences between oscillations of different frequencies. Note that peaks at different ω_{t_d} correspond to different peaks in the 2D spectra, i.e. diagonal and off-diagonal peaks.

However, in parts b and d of Fig. 4.15, we observe a shift in the emission frequency, ω_{t_d}, from about 682 to 675 nm as T changes from 500 to 1000 fs. From the arguments made in Sect. 4.2.4, this shift is not expected for amplitude modulations arising from interferences between oscillations of different frequencies. However, in practice at late T (T $\approx$ 1000 fs in our case) additional signals can be observed in the wavelets due to boundary effects [33]. These effects can be reduced by padding the signal before performing the wavelet transform. To explore the origins of the shift further, we consider the following synthetic signals:

$$A_5(t) = \sin(265t) + \sin(390t) + \sin(440t) \tag{4.11}$$

$$A_6(t) = \sin(265t) + \sin(440t) \tag{4.12}$$

Equation 4.12 is a superposition of sine waves at 265 and 440 cm^{-1} only, whilst Eq. 4.11 also includes a sine wave with a frequency of 390 cm^{-1}. All of these frequencies match peaks in the Fourier transform of the real rephasing 2DES spectra shown in Fig. 4.12. From the beating maps, contributions from all of these oscillation frequencies are present for the approximately diagonal peak at (681,682) nm in the 2D spectrum, therefore Eq. 4.11 approximates the signal at this point. However, oscillations at 390 cm^{-1} are less prominent at higher ω_{t_d} energies, hence Eq. 4.12 is an approximation to the signal around (681,675) nm.

We plot the wavelets for these synthetic signals in Fig. 4.16. In agreement with Fig. 4.15, we observe that the main peak in the amplitude at $\omega_T = 440$ cm^{-1} shifts from around 600 fs for Eq. 4.11 to 1000 fs for Eq. 4.12. In fact, the peak at 1000 fs arises from a boundary effect and its magnitude changes if the signal padding is altered. With fixed padding, the peak at 1000 fs disappears. The shifts in ω_{t_d} with T in parts b and d of Fig. 4.15 can be explained by this boundary effect. This result

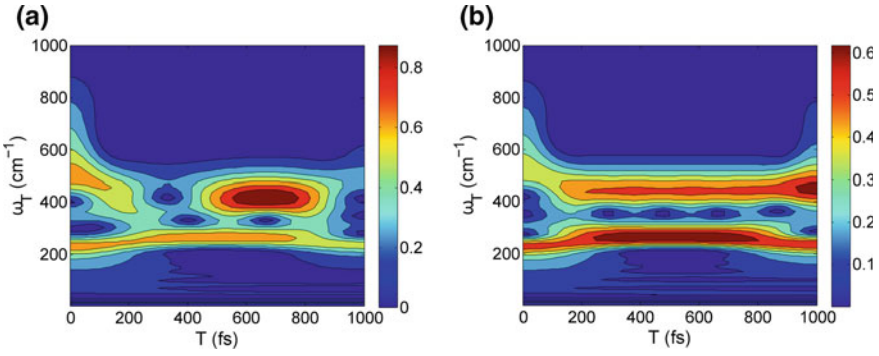

Fig. 4.16 Wavelet transforms of the signals given in Eqs. 4.11 (*left*) and 4.12 (*right*)

highlights the utility of simulating the 2D wavelet results using synthetic signals and the care needed when interpreting wavelet results from real data.

4.4 Conclusion

In conclusion, by considering artificial signals we have shown that the time signal from two interfering oscillations with different frequencies can be identical to the signal from amplitude modulation of an oscillation which might arise from regeneration of a vibronic coherence. Therefore in principle these two different signal origins cannot be distinguished, either by wavelet analysis or any other technique.

However, 2D spectroscopy provides a wealth of information beyond that which is contained in a single time trace and considering this additional information can give further insight into a signal's origins. In particular, in the case of interference between two oscillations with different frequencies, the period of the interfering envelope is determined by the frequency difference between the oscillations. This means that the period of the oscillations expected from this effect can be calculated and compared to the experimental results. We apply this approach to 2DES data for PSII and find that many of the amplitude modulations observed have periods which match the energy difference between oscillations of known frequencies.

In addition, we use synthetic signals to highlight the fact that interference between oscillations at two different frequencies can cause oscillations in the amplitude of the wavelet even if one of the oscillations has a significantly larger amplitude than the other. In this case it may be very difficult to tell from a visual inspection of the wavelet results that two different frequencies are interfering. Changing the position considered in the 2D spectrum is also expected to have different effects depending on the signal origin. Notably, as the position in the 2D spectrum changes, for interference effects the waiting time at which amplitude modulations occur is expected to remain constant. Again, we apply this approach to 2DES data for PSII and find that in general the waiting time at which the peak amplitude occurs is constant, as expected for interferences. However, this is not always the case at late waiting times. We show that this is due to additional boundary effects and care must be taken in these regions of the wavelet results.

Overall, this work shows that modelling the wavelet results with synthetic signals is extremely useful in determining their origins. This is because the signals are complicated by interferences between different frequencies and boundary effects, as discussed above. These additional effects mean that the wavelet transform of a specific point in the 2D spectrum needs to be examined in context. By simulating the signals it should be possible to establish which amplitude modulations arise from interference and boundary effects, and to identify any additional, unexpected amplitude modulations.

Although in this work we have focussed on wavelet analysis, another important question is whether wavelet transforms are the most effective type of time-frequency analysis to study the 2D spectra of biological systems. Recent work by Volpato and

Collini compared the abilities of several time-frequency approaches to analyse a synthetic signal [34]. They suggest that other types of time-frequency analysis (namely the smoothed-pseudo-Wigner Ville and smoothed Choi-Williams methods) may be able to overcome certain limitations of wavelet analysis, in particular the difficulties often encountered in resolving early time behaviour. Future time-frequency studies of 2DES data should carefully consider the most appropriate time-frequency method (which may depend on the characteristics of the dataset), whilst using simulations to maximise the information which can be obtained.

References

1. Ishizaki, A., Calhoun, T.R., Schlau-Cohen, G.S., Fleming, G.R.: Quantum coherence and its interplay with protein environments in photosynthetic electronic energy transfer. Phys. Chem. Chem. Phys. **12**, 7319–7337 (2010)
2. Christensson, N., Kauffmann, H.F., Pullerits, T., Mančal, T.: Origin of long-lived coherences in light-harvesting complexes. J. Phys. Chem. B **116**, 7449–7454 (2012)
3. Butkus, V., Zigmantas, D., Abramavicius, D., Valkunas, L.: Distinctive character of electronic and vibrational coherences in disordered molecular aggregates. Chem. Phys. Lett. **587**, 93–98 (2013)
4. Romero, E., Augulis, R., Novoderezhkin, V.I., Ferretti, M., Thieme, J., Zigmantas, D., van Grondelle, R.: Quantum coherence in photosynthesis for efficient solar-energy conversion. Nat. Phys. **10**, 676–682 (2014)
5. Fuller, F.D., Pan, J., Gelzinis, A., Butkus, V., Senlik, S.S., Wilcox, D.E., Yocum, C.F., Valkunas, L., Abramavicius, D., Ogilvie, J.P.: Vibronic coherence in oxygenic photosynthesis. Nat. Chem. **6**, 706–711 (2014)
6. Tiwari, V., Peters, W.K., Jonas, D.M.: Electronic resonance with anticorrelated pigment vibrations drives photosynthetic energy transfer outside the adiabatic framework. Proc. Natl. Acad. Sci. **110**, 1203–1208 (2013)
7. Chin, A., Prior, J., Rosenbach, R., Caycedo-Soler, F., Huelga, S., Plenio, M.: The role of non-equilibrium vibrational structures in electronic coherence and recoherence in pigment-protein complexes. Nat. Phys. **9**, 113–118 (2013)
8. Blankenship, R.: Molecular Mechanisms of Photosynthesis, 2 edn. Wiley-Blackwell (2014)
9. Jordanides, X., Scholes, G., Fleming, G.: The mechanism of energy transfer in the bacterial photosynthetic reaction center. J. Phys. Chem. B **105**, 1652–1669 (2001)
10. Schlau-Cohen, G., Re, E.D., Cogdell, R., Fleming, G.: Determination of excited-state energies and dynamics in the B band of the bacterial reaction center with 2D electronic spectroscopy. J. Phys. Chem. Lett. **3**, 2487–2492 (2012)
11. Westenhoff, S., Palecek, D., Edlund, P., Smith, P., Zigmantas, D.: Coherent picosecond exciton dynamics in a photosynthetic reaction center. J. Am. Chem. Soc. **134**, 16484–16487 (2012)
12. Bassi, R.: Berkeley Researchers Identify Photosynthetic Dimmer Switch (2008). http://www2.lbl.gov/Science-Articles/Archive/PBD-CP29.html
13. Viruvuru, V., Fragata, M.: Photochemical cooperativity in photosystem II. Characterization of oxygen evolution discontinuities in the light-response curves. Phys. Chem. Chem. Phys. **10**, 6607–6614 (2008)
14. Diner, B.A., Rappaport, F.: Structure, dynamics, and energetics of the primary photochemistry of Photosystem II of oxygenic photosynthesis. Annu. Rev. Plant Biol. **53**, 551–580 (2002)
15. Novoderezhkin, V.I., Dekker, J.P., van Grondelle, R.: Mixing of exciton and charge-transfer states in photosystem II reaction centers: modeling of Stark spectra with modified Redfield theory. Biophys. J. **93**, 1293–1311 (2007)

16. Abramavicius, D., Mukamel, S.: Energy-transfer and charge-separation pathways in the reaction center of photosystem II revealed by coherent two-dimensional optical spectroscopy. J. Chem. Phys. **133**, 184501 (2010)
17. Dekker, J.P., van Grondelle, R.: Primary charge separation in photosystem II. Photosynth. Res. **63**, 195–208 (2000)
18. Cardona, T., Sedouda, A., Cox, N., Rutherford, A.W.: Charge separation in Photosystem II: a comparative and evolutionary overview. Biochim. Biophys. Acta-Bioenergetics **1817**, 26–43 (2012)
19. Romero, E., van Stokkum, I.H.M., Novoderezhkin, V.I., Dekker, J.P., van Grondelle, R.: Two different charge separation pathways in photosystem II. Biochemistry **49**, 4300–4307 (2010)
20. Messinger, J., Shevela, D.: Principles of photosynthesis. In: Ginley, D.S., Cahen, D. (eds.) Fundamentals of Materials for Energy and Environmental Sustainability. Cambridge University Press (2012)
21. Wientjes, E., van Amerongen, H., Croce, R.: Quantum yield of charge separation in photosystem II: functional effect of changes in the antenna size upon light acclimation. J. Phys. Chem. B **117**, 11200–11208 (2013)
22. Calhoun, T.R., Ginsberg, N.S., Schlau-Cohen, G.S., Cheng, Y.-C., Ballottari, M., Bassi, R., Fleming, G.R.: Quantum coherence enabled determination of the energy landscape in light-harvesting complex II. J. Phys. Chem. B **113**, 16291–16295 (2009)
23. Turner, D.B., Dinshaw, R., Lee, K.-K., Belsley, M.S., Wilk, K.E., Curmic, P.M.G., Scholes, G.D.: Quantitative investigations of quantum coherence for a light-harvesting protein at conditions simulating photosynthesis. Phys. Chem. Chem. Phys. **14**, 4857–4874 (2012)
24. Flandrin, P.: Time-Frequency/Time-Scale Analysis, (Wavelet Analysis and Its Applications), vol. 10. Academic Press (1998)
25. Prior, J., Castro, E., Chin, A.W., Almeida, J., Huelga, S.F., Plenio, M.B.: Wavelet analysis of molecular dynamics: efficient extraction of time-frequency information in ultrafast optical processes. J. Chem. Phys. **139**, 224103 (2013)
26. Debnath, L.: Wavelet Transforms and their Applications. Birkhäuser, Boston (2002)
27. Mallat, S.: A theory for multiresolution signal decomposition: the wavelet representation. IEEE Trans. Pattern Anal. Mach. Intell. **11**, 674–693 (1989)
28. Burrus, C.S., Gopinath, R., Guo, H.: Introduction to Wavelets and Wavelet Transforms, a Primer. Prentice Hall, Upper Saddle River, NJ (USA) (1998)
29. Butkus, V., Zigmantas, D., Valkunas, L., Abramavicius, D.: Vibrational vs. electronic coherences in 2D spectrum of molecular systems. Chem. Phys. Lett. **545**, 40–43 (2012)
30. Ferretti, M., Novoderezhkin, V. I., Romero, E., Augulis, R., Pandit, A., Zigmantasc, D., van Grondelle, R.: The nature of coherences in the B820 bacteriochlorophyll dimer revealed by two-dimensional electronic spectroscopy. Phys. Chem. Chem. Phys. **16**, 9930–9939 (2014)
31. Schlau-Cohen, G.S., Ishizaki, A., Calhoun, T.R., Ginsberg, N.S., Ballottari, M., Bassi, R., Fleming, G.R. Elucidation of the timescales and origins of quantum electronic coherence in LHCII. Nat. Chem. **4**, 389–395 (2012)
32. Novoderezhkin, V.I., Romero, E., van Grondelle, R.: How exciton-vibrational coherences control charge separation in the photosystem II reaction center. Phys. Chem. Chem. Phys. **17**, 30828–30841 (2015)
33. Addison, P.S.: The Illustrated Wavelet Transform Handbook. Institute of Physics Publishing (2002)
34. Volpato, A., Collini, E.: Time-frequency methods for coherent spectroscopy. Opt. Express **23**, 20040–20050 (2015)
35. Romero, E., Prior, J., Chin, A. W., Morgan, S. E., Novoderezhkin, V. I., Plenio, M. B., van Grondelle, R.: Quantum-coherent dynamics in photosynthetic charge separation revealed by wavelet analysis. Sci. Rep. **7**, 2890 (2017)

Chapter 5
Nonlinear Network Model of Energy Transfer and Localisation in FMO

Using a term like nonlinear science is like referring to the bulk of zoology as the study of non-elephant animals.
Stanislaw Ulam, quoted in Campbell et al. [1]

In previous chapters I discussed the importance of molecular vibrations for singlet fission in pentacene, as well as the ubiquity of vibrations in biological light-harvesting complexes and the difficulties involved in distinguishing them from electronic coherences. However, to date little work has focussed on the microscopic details of these vibrations. One area in which the details of vibrational modes may be crucial is in describing the low frequency collective protein modes, which could play an important role in energy transfer in biological light harvesting complexes [2–4]. Protein vibrations can remain out of equilibrium over long time periods [5] and tend to be much less rigid than intramolecular pigment modes. Hence non-linear effects are often important [6, 7] and could provide alternative, intriguing energy transfer mechanisms.

In this final chapter I take the first steps towards building a microscopic description of these vibrations and clarifying their role in the archetypal light harvesting system, the Fenna-Matthews-Olson complex (FMO). To do this I use the nonlinear network model proposed by Juanico et al. [8], which offers a promising approach to studying nonlinear protein dynamics in a computationally inexpensive way. Interestingly, previous studies applying this model to a number of proteins have found the spontaneous localization of energy and formation of discrete breather modes (DBs) [9–11]. These localised modes are able to harvest energy from their surroundings and to transfer energy between different protein residues on picosecond timescales. If supported by light harvesting pigment protein complexes, DBs could therefore be functionally important for energy transfer and storage [12].

Firstly I review the structure of FMO and the use of network models to study protein dynamics. I then describe the high frequency normal modes (NMs) of FMO, a number of which are delocalised across the trimer and have strong components on

S.E. Morgan, *Ultrafast Quantum Effects and Vibrational Dynamics in Organic and Biological Systems*, Springer Theses, DOI 10.1007/978-3-319-63399-2_5

the pigments in the core of the FMO structure. Note that Renger et al. have previously considered the normal modes of FMO [13], however their work focussed on deriving the spectral function and did not discuss the spatial properties of individual modes. Moreover, because they used an all-atom model they were only able to study a single monomer. Whilst there is only weak excitonic coupling between the monomers, I will show that the trimeric structure can be important for mechanical effects. I then compute the dynamics which follow excitation of the highest frequency NM and find evidence for the existence of DBs in the structure. The DB which forms following excitation of the highest frequency NM is expected to modulate the energies of pigments 3, 4 and 7. Finally, I study the effect which this localised DB mode might have on the optical spectra; in particular the linear absorption (LA), linear dichroism (LD) and circular dichroism (CD) spectra. To do this, I use the pigment energies and couplings obtained by Cole et al. [14] from first principles using fully quantum-mechanical calculations. The DB is approximated by a mode of frequency $\omega = 100$ or $180\ \mathrm{cm}^{-1}$, which couples to pigments 3, 4 and 7. Including the mode can significantly improve the agreement between the calculated and experimental LA and LD spectra. Many of the results in this chapter have been published in [15]. The work was carried out in collaboration with Danny Cole, who provided the initial code for the molecular dynamics simulations (which I developed to incorporate NM analysis), helped with figures and contributed to the analysis of the results. The experimental linear absorption spectrum for comparison with theoretical results was supplied by Dugan Hayes, whilst Rienk van Grondelle and Markus Wendling supplied the experimental linear dichroism and circular dichroism spectra.

5.1 Structure of FMO

The Fenna-Matthews-Olson complex (FMO) is found in green sulfur bacteria, which perform anoxygenic photosynthesis and are able to survive deep underwater at very low light levels [16]. FMO acts as a funnel, transferring energy from the light harvesting antennae to the reaction centre. In 1975, FMO was the first light-harvesting pigment protein complex to have its structure characterised using X-ray spectroscopy [17]. FMO is a trimeric molecule, which consists of three monomers arranged in C_3 symmetry around the z-axis, as illustrated in Fig. 5.1a. Each monomer contains eight bacteriochlorophyll-a (BChl-a) pigments, whose structure is shown in Fig. 5.2. These pigments are able to absorb and then transfer energy between themselves. The eigth pigment lies outside of the protein envelope and here we will focus on the other 7 pigments, whose positions in the monomer are illustrated in Fig. 5.1b. It is thought that initial excitation mainly involves pigments 1 and 6 [18]. Energy is then transferred via the other pigments to pigments 3 and 4, which transfer the energy to the reaction centre [18, 19].

As early as 1997, Savikhin et al. observed oscillations in transient absorption measurements of FMO [22]. These oscillations were present in anisotropy measurements and hence could not be explained by simple vibrational wave packets. In 2007, Engel

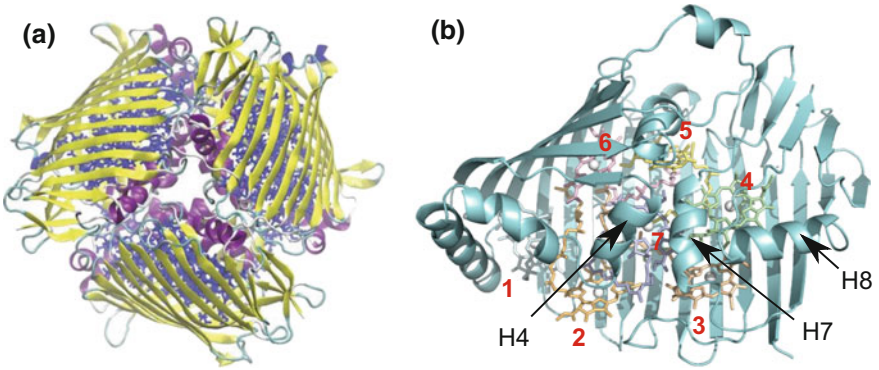

Fig. 5.1 **a** Trimeric structure of the FMO protein [20] and **b** the arrangement of the pigments within a single monomer. Helices 4, 7 and 8 are also highlighted (H4, H7 and H8)

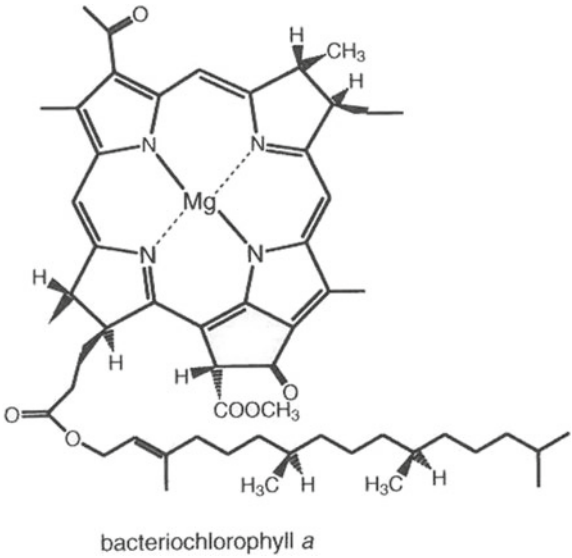

Fig. 5.2 Bacteriochlophyll-a molecule. Reproduced from [21] with permission from John Wiley & Sons, copyright 2014

et al. used 2DES to again observe long-lived (660 fs) oscillations in FMO at 77K [23], which they assigned to electronic coherences. Engel et al. suggested that these electronic coherences could be functionally important for efficient excitonic energy transfer since they existed on similar timescales. In 2010, the work was extended to show that similar oscillations can also be observed in FMO at room temperature [24].

Inspired by both these studies and similar observations in other light-harvesting pigment protein complexes, theoretical work has focussed on ways in which electronic coherences might be sustained in these systems. For example in 2013 Chin et al. used a numerically exact approach to model coherences in FMO and show that

underdamped oscillations can help to sustain electronic coherences [3], as discussed in Chap. 1. Jonas et al. also chose model parameters based on the FMO complex to study the role of anticorrelated pigment vibrations in energy transfer [25]. The wealth of information on the structure and dynamics of FMO, including work by Renger and Adolphs [18, 26] on energy transfer and protein dynamics, makes FMO an ideal archetypal system to study theoretically.

5.2 Network Models

Elastic network models (ENM) can be used to study protein dynamics by modelling the protein as a collection of particles connected by springs, as illustrated in Fig. 5.3. The ENM was first proposed in 1996 by Tirion [27], who modelled each atom in the protein as an individual particle and was able to reproduce the density of low frequency modes in the muscle protein, G-actin. In 1998, Hinsen proposed a simplified coarse-grained model with only the carbon alpha (C_α) atoms [28]. Over the last 20 years, the ENM has found a number of applications. These include predicting biologically relevant protein dynamics, for example one study showed significant agreement between the ENM and experimental results in cases where ligand binding induces collective conformational changes [29]. More details can be found in reviews of the ENM [30, 31].

However, low-frequency, collective protein vibrations exhibit significant anharmonicities [7] and there is growing experimental evidence for long lived nonlinear vibrations in proteins [33]. In order to approximate these effects, in 2007 Juanico et al. introduced the nonlinear network model (NNM) [8]. As in other network models,

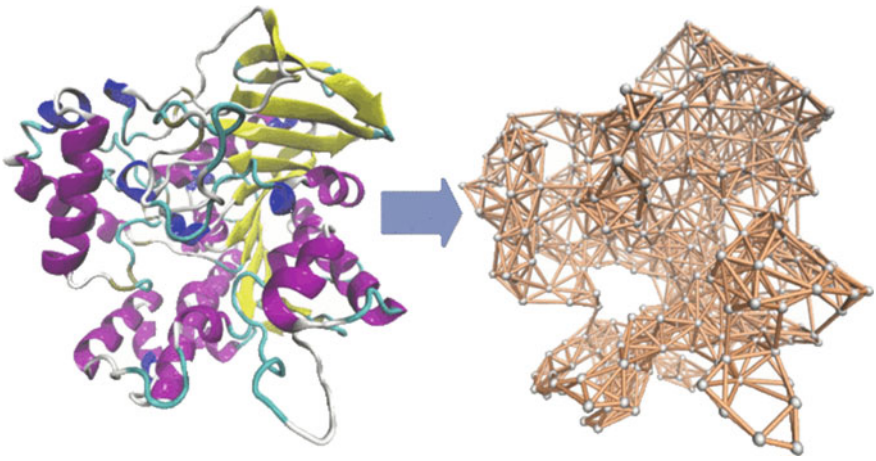

Fig. 5.3 Illustration of an elastic network model of a protein. Figure taken from [32], licensed under CC BY 3.0

each amino acid is represented by a point-like particle with mass m, which is placed at the position of the corresponding C_α atom. However, the NNM potential energy has both a linear and a nonlinear term and reads [8, 11, 34]:

$$E = \sum_{i>j} c_{ij} \left[\frac{k_2}{4} \left(r_{ij} - R_{ij} \right)^2 + \frac{k_4}{8} \left(r_{ij} - R_{ij} \right)^4 \right] \tag{5.1}$$

where the first term (with the coefficient k_2) is the linear term and the second term (with the coefficient k_4) is the nonlinear term. $r_{ij} = \left| \mathbf{r}_i - \mathbf{r}_j \right|$ is the instantaneous distance between nodes i and j and $R_{ij} = \left| \mathbf{R}_i - \mathbf{R}_j \right|$ is the distance between nodes i and j at equilibrium (t=0). Connections are made between nodes which are within a cut-off distance, R_c, by setting $c_{ij} = 1$ if $R_{ij} < R_c$ and $c_{ij} = 0$ otherwise.

Juanico et al. showed that NNMs of proteins can support discrete breather (DB) modes [8]. These are localised, nonlinear modes which can harvest energy from their surroundings and then transfer energy between different regions of the protein. Subsequent work has confirmed this result in a number of proteins [9, 11, 34]. For example, work by Caraglio and Imparato used the NNM to study energy transfer in kinesin and hemoglobin [11]. They excited individual residues and observed the formation of localized modes, with frequencies above the upper edge of the harmonic spectrum. They also observed vibrational energy transfer between different

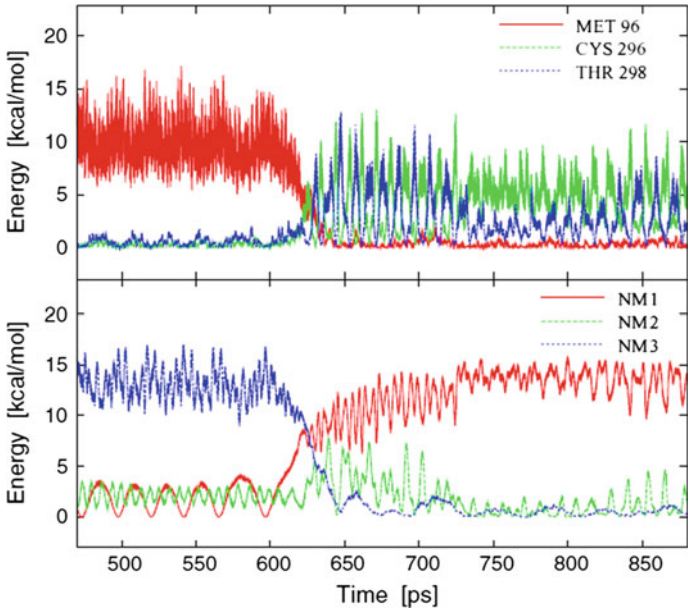

Fig. 5.4 Energy transfer in kinesin, after an initial kick of 30 kcal/mol at site MET 96. Both the energies of individual sites *(top)* and individual normal modes *(bottom)* are shown. Reprinted figure with permission from [11]. Copyright 2014 by the American Physical Society

residues, see for example Fig. 5.4. Although most work to date has been theoretical, a study by Piazza et al. on ubiquitin showed that correlated motions observed using NMR measurements match the calculated displacement patterns of DBs [34]. More experimental work is needed to test and inform theoretical studies.

Here we use the NNM to model FMO. The mass of each amino acid is approximated as 110 atomic mass units. Calculations were based on the *holo* (8 BChl-a per monomer) form of the trimeric 1.3 Å X-ray crystal structure of *Prosthecochloris aestuarii* (PDB: 3EOJ) [35], although as stated above we only consider 7 pigments. Based on their relative masses, the chlorin ring and phytol tail of the BChl-a pigment molecules are modelled by 5 nodes and 3 nodes, respectively. The nodes are placed at the positions of the MG, C2A, C2B, C2C, C2D, C2, C10 and C18 atoms (crystal structure atom labelling). We note that this treatment does not describe the intramolecular modes properly, however in this work we will focus on the low frequency intermolecular protein modes. Together the residues and pigment atoms make up the 1242 nodes of our model.

5.3 Normal Modes

Firstly we compute the NMs of our model by calculating the eigenvectors and eigenvalues of the Hessian matrix [36]. There are 3726 NMs in total, with the first six being trivial (with zero frequency, arising from translation and rotation). Note that in the following we will refer to the highest frequency NM as NM 3726 and the lowest frequency NM as NM 1. In order to characterise these vibrations we calculate the locality index of each NM, using the same metric as employed by Piazza et al. to measure the spatial patterns of DBs [9]:

$$L = \frac{\sum_{i\alpha} \zeta_{i\alpha}^4}{\left[\sum_{i\alpha} \zeta_{i\alpha}^2\right]^2} \tag{5.2}$$

where α refers to the (x,y,z) co-ordinates and $\zeta_{i\alpha}$ is the amplitude of the α co-ordinate of node i in NM ζ. The locality index for each normal mode is plotted in Fig. 5.5, as a function of mode frequency. The majority of modes have frequencies between approximately 35 cm^{-1} and 90 cm^{-1} and are relatively delocalised.

Many of the low frequency NMs are also delocalised, however counter-intuitively a few low frequency modes are very well localised. On closer inspection, these modes are localised on residues with low degree (i.e. a low number of connections) which are at the surface of the complex, for example residues ASN 334 and GLY 213. The degree of each node is plotted in Fig. 5.6a and residues ASN 334 and GLY 213 are higlighted. NM 45 has the highest locality index, a frequency of 12.5 cm^{-1} and is localised on residue ASN 334 in each monomer.

We now turn to the high frequency NMs, which will be the focus of this chapter. Again, several high frequency NMs exhibit above average localisation, however the

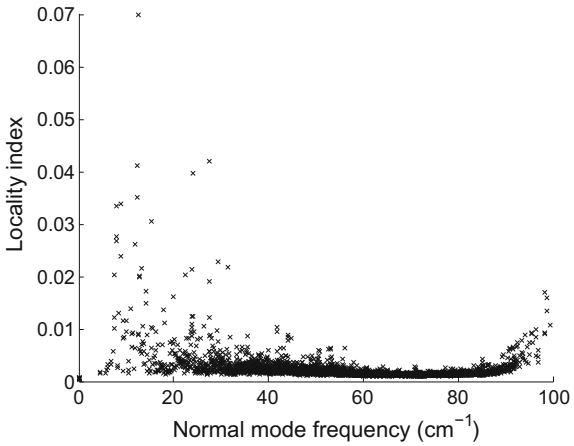

Fig. 5.5 The locality index of each normal mode plotted as a function of mode frequency

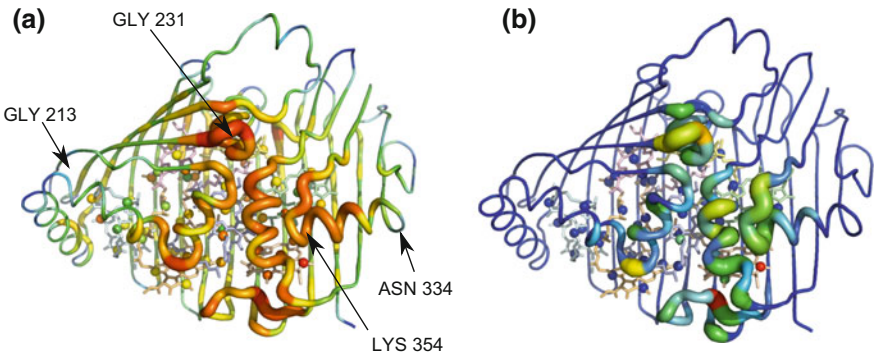

Fig. 5.6 FMO monomer coloured according to **a** the connectivity (degree) of each residue, **b** the amplitude of the NM squared on each node averaged over the 20 highest frequency NMs. Note that for **a** all monomers are identical, whilst for **b** monomer 1 is shown although monomers 2 and 3 are the same to within 0.025% of the total amplitude. Both parts are plotted using a rainbow colour spectrum. For **a** the degree ranges from 7 to 34 whilst for **b** values range from 0 to 1.3% of the total amplitude

NMs are now localised on nodes with high connectivity. To show this, the amplitude of the NM squared on each node averaged over the 20 highest frequency NMs is plotted in Fig. 5.6b. From a visual inspection, the amplitudes in Fig. 5.6b are very similar to those shown in Fig. 5.6a for the node degree. Figure 5.7 also plots the amplitude of the NM squared on a node averaged over the 20 highest frequency NMs as a function of the node's degree and shows that there is a correlation between the two. We note that the pigment atoms (highlighted in red) tend to have high connectivity. The total number of connections made by pigment atoms for pigments

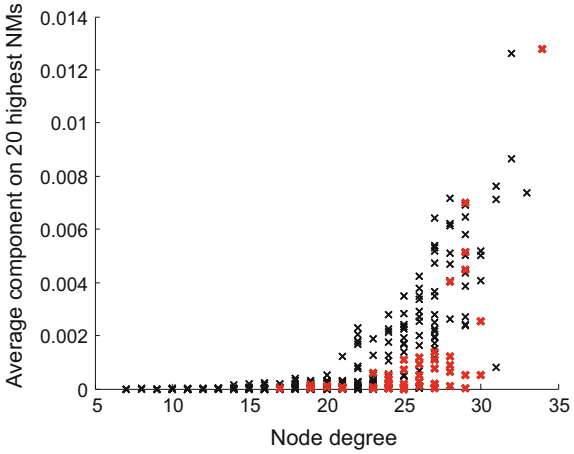

Fig. 5.7 The amplitude of the NM squared on a node averaged over the 20 highest frequency NMs as a function of the node's degree. The pigment nodes are higlighted in *red*

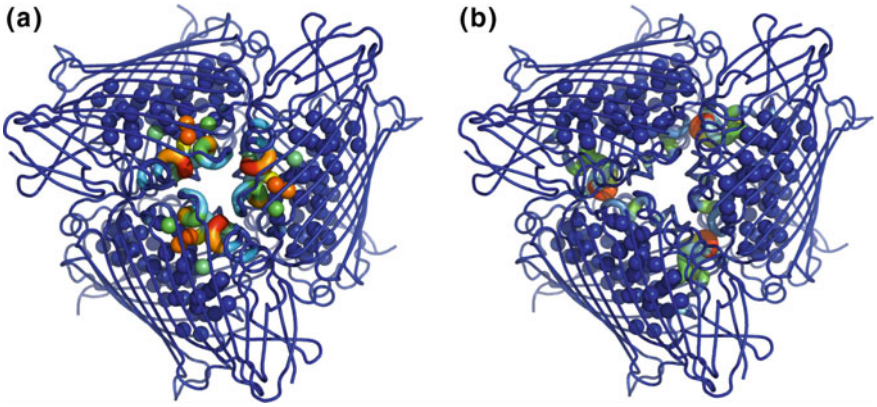

Fig. 5.8 FMO trimer coloured according to **a** the highest frequency NM, **b** the fourth highest frequency NM

found in the core of the complex (pigments 3, 4, 5, 6 and 7) are higher than those found near the surface of the protein (pigments 1 and 2).

Several of the high frequency NMs are delocalised across the trimer. As examples, in Fig. 5.8 we plot the highest frequency NM and the fourth highest frequency NM (the second and third highest frequency NMs are not delocalised across the whole trimer but have components on similar nodes within the monomer to the highest frequency NM, due to symmetry). These NMs have frequencies of 99.4 cm^{-1} and 98.4 cm^{-1} respectively. They are both split equally across the three monomers, with almost identical contributions on individual residues in each monomer (to within 0.03% of the total amplitude). 7.4% of the highest frequency NM is localised on

pigment 3 in each monomer, although the largest component on any single node is on the residue LYS 354 (3.6% of the total amplitude is found on LYS 354 in each monomer). LYS 354 lies on helix 8 and forms an inter-monomer salt bridge with ASP 306 and close hydrophobic contact with PHE 304, which is close to helix 7 on the neighbouring monomer. The largest component of the fourth highest frequency NM is localised on residue GLY 231 (3.5% of the total amplitude). Both LYS 354 and GLY 231 have high connectivity and are highlighted in Fig. 5.6.

5.4 Dynamics

In order to study the protein's dynamics we excite the highest frequency NM with a total energy of $E_0 = 40$ kcal/mol and then simulate the molecular dynamics (MD), using a Velocity Verlet algorithm [37] with a 1 fs time step. The network is excited with total energy E_0 in the direction of one of the NMs. We then record the total energy of every residue at each time step, given by a sum of the kinetic and potential energies.

Exciting the delocalised NMs is expected to lead to energy dissipation across the trimer complex over time. For example when NM 1206 (which has a frequency of 50.0 cm^{-1}) is excited with 40 kcal/mol, no individual node has more than 0.7% of the total energy after 1 ns. Exciting the localised, low frequency modes also leads to energy dissipation, for example when NM 45 is excited with 40 kcal/mol of energy, after 1 ns no individual node has more than 0.45% of the total energy.

We now turn to the highest frequency NM, which is chosen following work in the literature which suggests that localised DB modes can emerge from a subset of high frequency NMs [8, 10]. In nature, these modes might be excited by thermal fluctuations or from the energy dissipation resulting from light absorption and recombination processes. We set $k_2 = 10$ kcal/mol/Å^2 and $k_4 = 10$ kcal/mol/Å^4, following Piazza et al. [8, 34]. Although the highest frequency NM is split equally across the three monomers, as described above, after 100 ps of the molecular dynamics simulation 72.8% of the energy has become localised on monomer 3. In Fig. 5.9 we plot monomer 3 and the full FMO complex coloured according to the average displacement during the MD simulation from 100 ps to 1 ns. We observe significant localisation, in particular pigment 3 exhibits the largest displacement and we also observe substantial vibrational motion of helices 7 and 8.

To study the localisation process in more detail, in Fig. 5.10 we plot the total energy on pigment 3 on each monomer over time, for three different values of anharmonicity: $k_4 = 5$, 10 and 15 kcal/mol/Å^4. As the anharmonicity increases, the localisation of energy on pigment 3 occurs more quickly, and vice versa. For $k_4 = 5$ kcal/mol/Å^4, we observe vibrational energy transfer between pigment 3 molecules on the three monomers (note that this continues at later times, for example after 1300 ps the energy is transferred to pigment 3 on monomer 1). In Fig. 5.11, we plot the energy on pigment 3 when the initial energy is $E_0 = 20$, 25, 30, 35, 40 or 45 kcal/mol. Increasing/decreasing the excitation energy has a similar effect on the dynamics

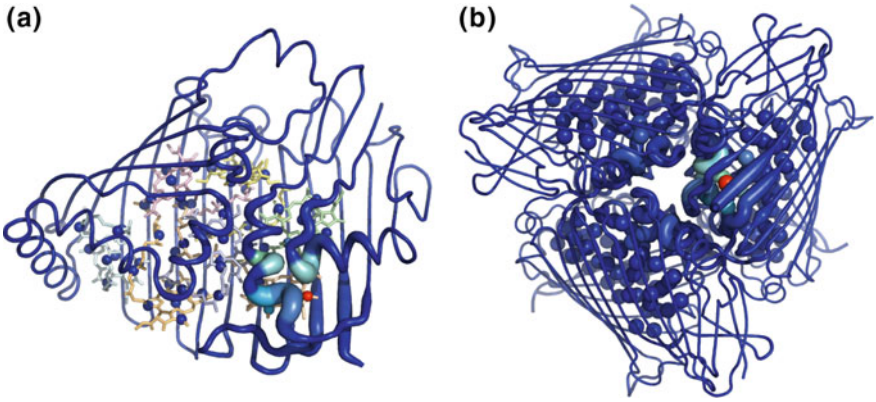

Fig. 5.9 The FMO complex coloured according to the average displacement during the MD simulation from 100 ps to 1 ns, shown as (**a**) monomer 3 only, (**b**) the full trimer

to increasing/decreasing the anharmonicity. Crucially, the localisation we observe around pigment 3 on a single monomer appears to be a fairly generic phenomenon, which occurs over a broad range of excitation energies and anharmonicity values. The energy remains localised for long times relative to excitation energy transfer in the FMO complex. Overall, the remarkable ability of the complex to harvest energy from multiple spatial locations and localise it on and around the core pigments could have important consequences for light harvesting processes. Notably, pigments 3 and 4 have been shown to act as the energy sink for FMO and funnel energy excitations to the reaction centre [18, 19], therefore vibrational energy transfer to this region is particularly interesting. Helices 7 and 8 have also been shown to be important in directing energy transport towards pigments 3 and 4 (the helix dipoles red shift the site energies) [19].

We calculate the power spectrum of the x displacement of the node in pigment 3 with the highest energy (on the monomer with the highest energy), taken over a 300 ps period beginning after 300 ps of the molecular dynamics, as shown in Fig. 5.12. For $k_4 = 10$ kcal/mol/Å^4, the main peak has a frequency of 104.8 cm^{-1}, which is approximately 5.4 cm^{-1} higher than the frequency of the highest energy normal mode at 99.4 cm^{-1}. Similar results were obtained for displacements in the y and z directions. From work by Juanico and Piazza [8, 9], this gap between the top of the harmonic spectrum and the frequency of the oscillations suggests the presence of a DB. The significant localisation of energy discussed above is also typical of DBs. For $k_4 = 5$ kcal/mol/Å^4 the main peak in the power spectrum shifts down to 100.1 cm^{-1}. When $k_4 = 15$ kcal/mol/Å^4, we find the main peak is at the higher frequency of 106.7 cm^{-1} (in this case we take the x-displacement between 100 ps and 400 ps).

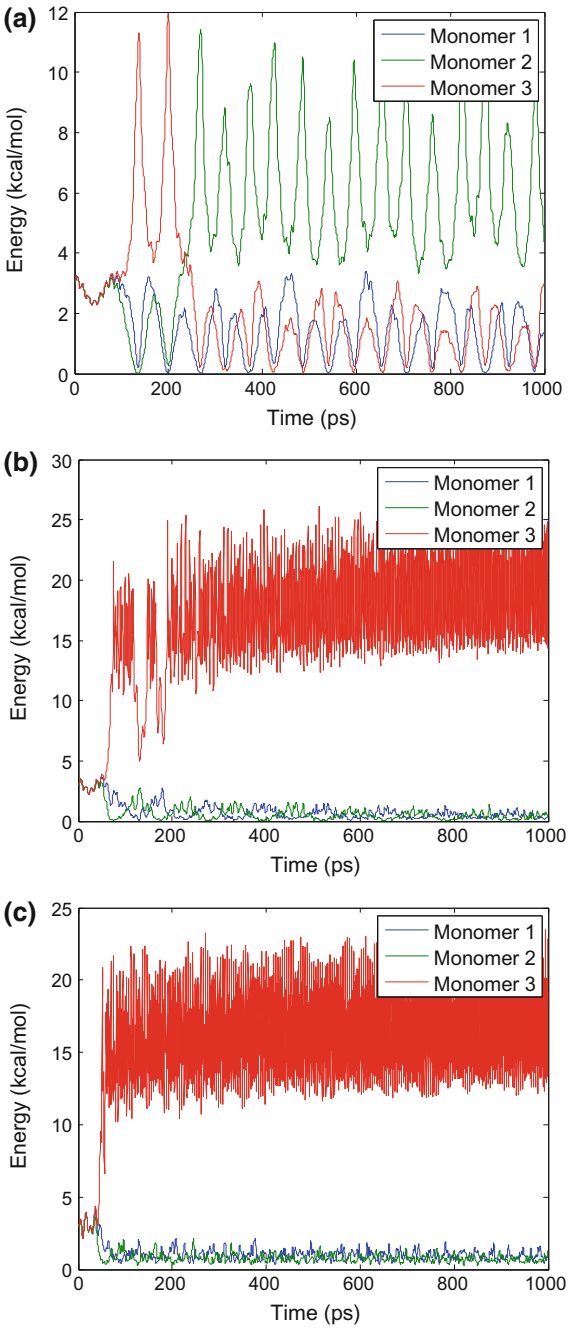

Fig. 5.10 The total energy on pigment 3 on each monomer over the first 1 ns following excitation of the highest frequency NM, with $E_0 = 40$ kcal/mol. Results are shown for $k_4 = 5$, 10 and 15 kcal/mol/Å^4 in a, b and c, respectively

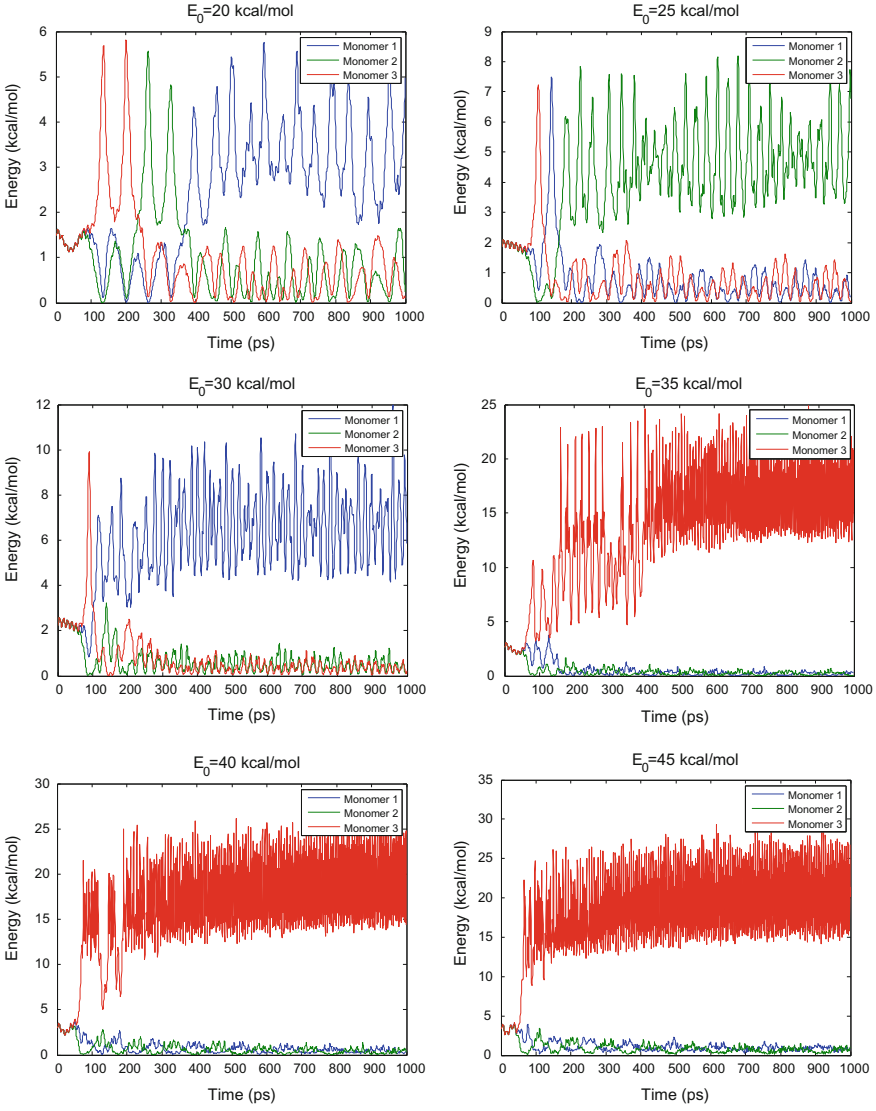

Fig. 5.11 The total energy on pigment 3 on each monomer over the first 1 ns following excitation of the highest frequency NM with $k_2 = 10\,\text{kcal/mol/Å}^2$, $k_4 = 10\,\text{kcal/mol/Å}^4$ and initial energies of $E_0 = 20, 25, 30, 35, 40$ and 45 kcal/mol

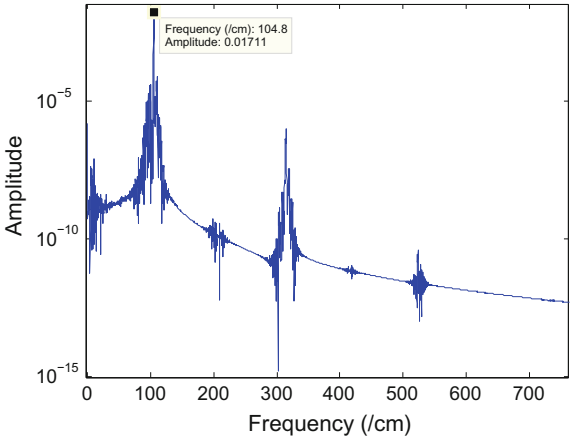

Fig. 5.12 The power spectrum of the x displacement of the node in pigment 3 with the highest energy, taken over a 300 ps period, beginning 300 ps after excitation of the highest frequency NM, for $k_4 = 10$ kcal/mol/Å^4

In Fig. 5.10 we observe both high and low frequency oscillations in the energy on pigment 3 over time. By taking the Fourier transform of the total energy on pigment 3 between 300 and 1300 ps, we find that the main high frequency peaks lie at 200.3, 210.9 and 215.4 cm^{-1} for $k_4 = 5$, 10 and 15 kcal/mol/Å^4 respectively. In each case this is approximately twice the frequency of the main peak in the power spectrum of the trajectory. We also observe low frequency oscillations, corresponding to peaks in the Fourier transform of the total energy on pigment 3 at 0.6, 6.3 and 7.1 cm^{-1} for $k_4 = 5$, 10 and 15 kcal/mol/Å^4 respectively. These low frequency oscillations are a result of the nonlinear term in Eq. 5.1, however their exact origin remains unclear and requires further investigation. Picosecond timescales are known to be important for energy transfer in FMO, for example Zigmantas et al. recently proposed a 17 ps timescale for excitonic energy transfer between the lowest energy FMO state and the reaction centre from experimental observations [38]. Low frequency oscillations such as those observed prominently in Fig. 5.10a could provide alternative energy transfer pathways, perhaps enabling 'trapped' energy to be redistributed.

Similar results are obtained when other high frequency NMs are excited, namely the energy becomes localised on a specific pigment or residue with high connectivity and a DB forms with a frequency which lies above the top of the harmonic spectrum. For example, when the fourth highest frequency NM is excited the energy becomes localised on residue GLY 231, which is found in the core of the complex near to helix 4. Note that in this case we excite the complex with $E_0 = 50$ kcal/mol since $E_0 = 40$ kcal/mol does not lead to significant localisation on any single node within the first 2 ns. Figure 5.13 plots the energy on GLY 213 of monomer 1 and the FMO trimer coloured according to the average displacement during 1.1 ns to 2 ns of the MD simulation following excitation of the fourth highest frequency NM.

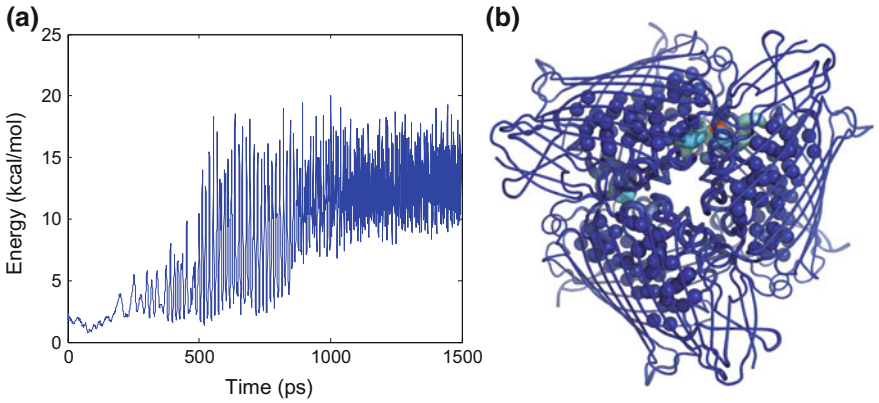

Fig. 5.13 **a** Energy on residue GLY 231 of monomer 1 over time, **b** the FMO trimer coloured according to the average displacement during 1.1 to 2 ns of the MD simulation following excitation of NM 3723

5.5 Optical Spectra

As seen in previous chapters, optical spectra can be extremely useful in providing information about molecular systems and the linear absorption (LA), linear dichrosim (LD) and circular dichroism spectra (CD) are frequently used to characterise materials. The nonlinear vibrational dynamics described in the previous sections might be expected to alter these optical spectra. Therefore in this section we calculate the LA, LD and CD obtained when incorporating a single vibrational mode on the same footing as the electronic states, as a first approximation to the DB dynamics described previously. Crucially, the DB is expected to couple to different pigments with different strengths. Above we showed that exciting the highest frequency NM leads to significant displacements of pigment 3 as well as helices 7 and 8. We are not aware of any studies explicitly studying the variation in pigment site energies with helix displacements, but the proximity of helices 7 and 8 to pigments 4 and 7 suggests that their site energies are also likely to be modulated by the DB. Other pigments are not expected to be affected. Therefore we couple the mode to pigments 3, 4 and 7 only. In practice the strength of the coupling to different pigments may vary but as a first approximation we set the Huang Rhys factor S=0.3 for pigments 3, 4 and 7. This is similar to the value of S=0.22 estimated by Adolphs et al. [18] and we note that a reasonably large Huang-Rhys factor could reflect the large amplitude nature of the non-linear vibration.

The total Hamiltonian is:

$$H = \sum_i \varepsilon_i \left|i\right\rangle \left\langle i\right| + \sum_{i \neq j} J_{ij} \left|i\right\rangle \left\langle j\right| + \sum_i g_i \left(a + a^\dagger\right) \left|i\right\rangle \left\langle i\right| + \hbar\omega a^\dagger a \qquad (5.3)$$

where ε_i is the energy of pigment i, J_{ij} is the coupling between optical excitations on pigments i and j, ω is the mode frequency and g_i is the coupling of pigment i to the mode. g_i depends on the Huang Rhys factor, S, according to $g_i = \sqrt{S}\omega$. We use the pigment energies and couplings obtained by Cole et al. [14] using large-scale quantum-mechanical calculations. To calculate the spectra we use the Master equation approach taken by Marcus [26] and Cole et al. [14], which makes the Markov approximation and hence each excitonic transition has a Lorentzian lineshape. We use the same parameters as Cole et al. for the pure dephasing rate and the spectral density function (which provides a smooth background bath) [14]. To include the effect of static disorder, the final spectra are obtained by averaging over 1000 realisations of the site energies, each drawn from a Gaussian distribution with a full-width half maximum of 100 cm^{-1}. We include 15 harmonic oscillator levels for the mode, which gives converged spectra.

The frequency of the DB is unknown (it is determined by k_2 and k_4 in our model), but from the literature high frequency protein normal modes might be expected to lie between approximately 100 and 200 cm^{-1} [8, 9, 39]. Given this uncertainty, in our calculations we consider two mode frequencies as examples: $\omega = 100$ and 180 cm^{-1}. We note that a mode has been observed experimentally with $\omega = 180$ cm^{-1} [40]. This mode is generally considered to be a pigment mode [40, 41], however as far as we are aware the intriguing possibility that this mode could be at least in part due to protein vibrations has not been ruled out. Note that we require $k_2 = 30$ kcal/mol/Å^2 for the top of the harmonic spectrum to lie around 180 cm^{-1} and previous work showing the high level of stiffness in FMO suggests that this is not unreasonable [42]. The dynamics following excitation of the highest frequency NM with $k_2 = 30$ kcal/mol/Å^2 and $k_4 = 30$ kcal/mol/Å^4 are similar to those obtained previously, leading to vibrational energy transfer to pigment 3 and helices 7 and 8, as shown in Fig. 5.14. Note that here we use $E_0 = 120$ kcal/mol, due to the higher values of $k_2 = 30$ kcal/mol/Å^2 and $k_4 = 30$ kcal/mol/Å^4.

Figure 5.15 plots optical spectra for $\omega = 100\,\text{cm}^{-1}$ and $\omega = 180\,\text{cm}^{-1}$ coupled to pigments 3, 4 and 7. We also plot the optical spectra with no mode (as calculated by Cole et al. [14]), for comparison. Spectra with modes coupled to all seven pigments (not just pigments 3, 4 and 7) are shown in Fig. 5.16. All calculated spectra are compared to experimental results for *P. aestuarii* obtained at 77K [43] (plotted in red). We note that whilst in Eq. 5.3 we have assumed linear coupling to the mode, when an anharmonic energy shift ($= \Delta\omega(a^\dagger a)^2$, where $\Delta = 0.1$) was included we did not observe significant spectral changes, as shown in Fig. 5.17.

For both $\omega = 100$ cm^{-1} and $\omega = 180$ cm^{-1}, LA and LD spectra obtained by coupling a mode to pigments 3, 4 and 7 are significantly closer to the experimental results than results obtained with no mode or a mode with equal coupling to all pigments. In particular, the peak around 12300 cm^{-1} in the LA, which was underestimated in calculations with no mode, becomes more prominent. Meanwhile the peak around 12450 cm^{-1}, which was overestimated in the calculations with no mode, is reduced. In the LD spectra, the peak at 12300 cm^{-1} was significantly underestimated in the original calculations. When the mode is included this peak is much deeper. The LD spectra around 12400 cm^{-1} are also much closer to experimental

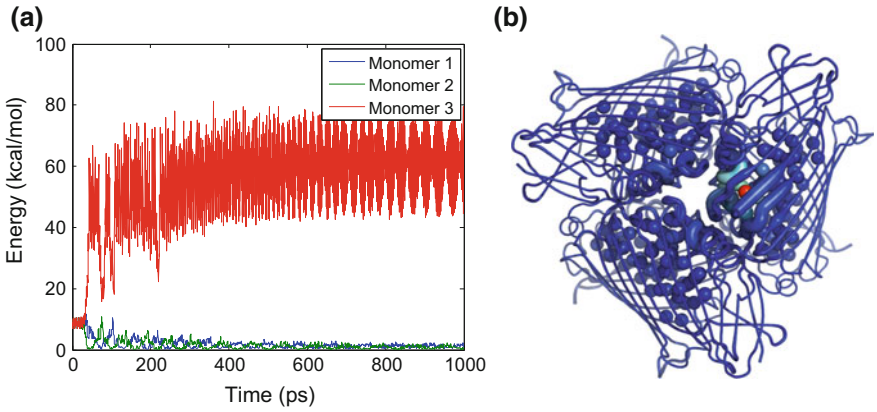

Fig. 5.14 **a** The total energy on pigment 3 on each monomer over the first 1 ns, **b** the FMO trimer coloured according to the average displacement during the MD simulation from 100 ps to 1 ns. In both cases, NM 3726 is excited, $k_2 = 30$ kcal/mol/Å^2, $k_4 = 30$ kcal/mol/Å^4 and $E_0 = 120$ kcal/mol

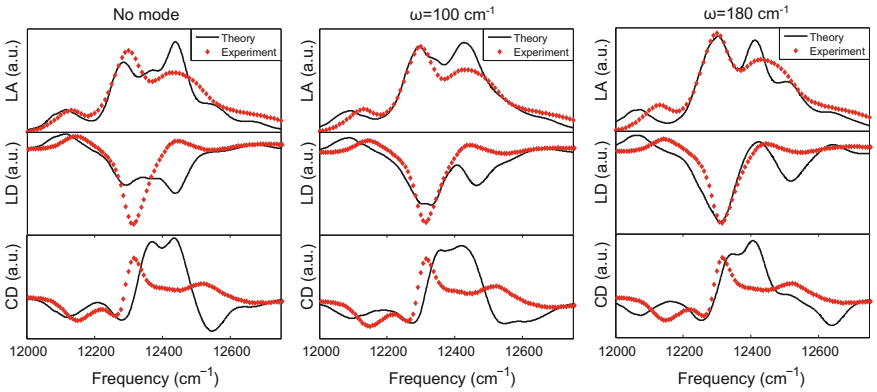

Fig. 5.15 LA, LD and CD spectra for calculations with no mode and for modes with $\omega = 100$ and 180 cm^{-1} *(black lines)*. Experimental spectra are shown in *red* for comparison [43]

results with the mode, particularly when $\omega = 180$ cm^{-1}. The inability of a mode coupling to all pigments to capture these effects, as shown in Fig. 5.16, highlights the potential importance of localised non-linear protein oscillations. Note that the coupling of the mode to pigment 3 lowers the energy of the lowest energy exciton, which red shifts the low energy parts of the spectra, slightly worsening the agreement with the experimental results in that region. This discrepancy could be caused by an error in the ab initio pigment 3 site energy, which is lower than the result obtained by Adolphs et al. for example [18]. Various approximations were employed in the calculation of ab initio site energies, see Cole et al. for details [14]. Alternatively, the mode might couple more strongly to pigments 4 and 7 than to pigment 3, perhaps

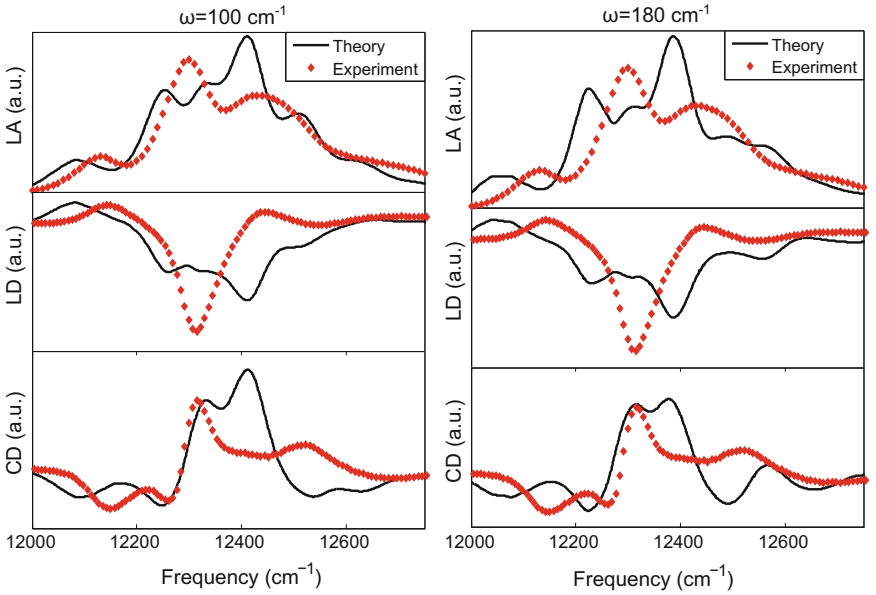

Fig. 5.16 LA, LD and CD spectra for calculations with a mode coupled equally to all pigments with $\omega = 100$ and 180 cm^{-1} *(black lines)*. Experimental spectra are shown in *red* for comparison [43]

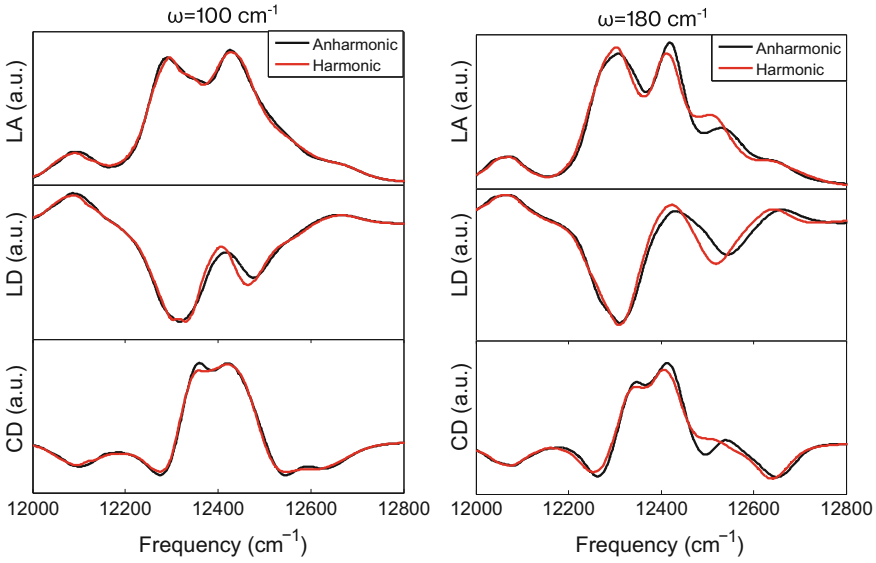

Fig. 5.17 LA, LD and CD spectra for calculations with an anharmonic term with $\omega = 100$ and 180 cm^{-1} *(black lines)*. The spectra without the anharmonic term are shown in *red* for comparison

because the DB mode which emerges from exciting the highest frequency NM is not representative of the average DB coupling across all complexes or due to other effects not captured by the relatively simple nonlinear network model. Further work is required to understand the relative importance of these sources of error and also to elucidate the circular dichroism results, which are not substantially improved by incorporating the mode.

5.6 Conclusion

To our knowledge, this work is the first to apply the nonlinear network model to study the archetypal light-harvesting complex, FMO. This computationally inexpensive approach allows us to investigate FMO's collective protein modes, which have been implicated in the energy transfer processes, at a microscopic level. Our model also incorporates an anharmonic term which enables us to take a first step towards capturing the anharmonic effects that previous work shows are often important for protein dynamics [6, 7, 33].

We find that the high frequency NMs can be delocalised across the trimer and exhibit strong components on the core pigments and on certain residues with high degree. When high frequency NMs are excited, we observe energy localisation in biologically relevant areas of the protein. For example exciting the highest frequency NM leads to energy localisation around pigment 3 and helices 7 and 8, which are expected to modulate the site energies of pigments 4 and 7. By studying the power spectrum we show that a DB mode has been formed and similar results can be obtained following excitation of other high frequency NMs. These non-linear DB modes offer the potential for intriguing alternative energy transfer routes. In particular they could play a role in localising and storing excess energy around pigments 3 and 4 which are known to funnel energy towards the reaction centre. Future work should focus on the details of these processes, both experimentally and by establishing more accurate theoretical models. The ability of DBs to transfer energy around the protein could also lead to an environment which is temporally spatially dependent; in other words an environment with a spatial dependence which changes over time. This type of environment has received little attention to date and could open up exciting possibilities for device design.

Having established the existence of potentially biologically important DBs in our system, we investigate the effect which these localised modes might have on the optical spectra which were calculated by Cole et al. [14] using ab initio site energies and couplings. To do this we approximate the DB as a single mode, localised on pigments 3, 4 and 7 with example frequencies of $\omega = 100$ or $180\ \mathrm{cm}^{-1}$. We incorporate this mode into optical spectra calculations on an equal footing with the electronic energy levels. We show that substantial improvements in the LA and LD spectra can be obtained, particularly around the $12300 - 12450\ \mathrm{cm}^{-1}$ region. We note that this is in contrast to the effect of incorporating very low frequency modes, which previous work found did not affect the spectra significantly [42]. Nonetheless

there is room for improvement, in particular the lowest energy exciton is lower than observed experimentally and the circular dichroism spectra still show substantial differences from the experimental results. This work highlights the importance of ab initio calculations of the pigment energies and couplings and further work is needed to obtain more accurate ab initio site energies [44].

References

1. Campbell, D., Crutchfield, J., Farmer, J., Jen, E.: Experimental mathematics: the role of computation in nonlinear science. Commun. Assoc. Comput. Mach. **28**, 374–84 (1985)
2. Fassioli, F., Nazir, A., Olaya-Castro, A.: Quantum state tuning of energy transfer in a correlated environment. J. Phys. Chem. Lett. **1**, 2139–2143 (2010)
3. Chin, A., Prior, J., Rosenbach, R., Caycedo-Soler, F., Huelga, S., Plenio, M.: The role of non-equilibrium vibrational structures in electronic coherence and recoherence in pigment-protein complexes. Nat. Phys. **9**, 113–118 (2013)
4. Mourokh, L.G., Nori, F.: Energy transfer efficiency in the chromophore network strongly coupled to a vibrational mode. Phys. Rev. E **92**, 052720 (2015)
5. Hu, X., Hong, L., Smith, M.D., Neusius, T., Cheng, X., Smith, J.C.: The dynamics of single protein molecules is non-equilibrium and self-similar over thirteen decades in time. Nat. Phys. **12**, 171–174 (2016)
6. Levy, R.M., Perahia, D., Karplus, M.: Molecular dynamics of an α-helical polypeptide: Temperature dependence and deviation from harmonic behavior. Proc. Natl. Acad. Sci. **79**, 1346–1350 (1982)
7. Hayward, S., Kitao, A., Go, N.: Harmonicity and anharmonicity in protein dynamics: a normal mode analysis and principal component analysis. Proteins **23**, 177–186 (1995)
8. Juanico, B., Sanejouand, Y., Piazza, F., Rios, P.D.L.: Discrete breathers in nonlinear network models of proteins. Phys. Rev. Lett. **99**, 238104 (2007)
9. Piazza, F., Sanejouand, Y.-H.: Discrete breathers in protein structures. Phys. Biol. **5**, 026001 (2008)
10. Luccioli, S., Imparato, A., Lepri, S., Piazza, F., Torcini, A.: Discrete breathers in a realistic coarse-grained model of proteins. Phys. Biol. **8**, 046008 (2011)
11. Caraglio, M., Imparato, A.: Energy transfer in molecular devices. Phys. Rev. E **90**, 062712 (2014)
12. Kopidakis, G., Aubry, S., Tsironis, G.P.: Targeted energy transfer through discrete breathers in nonlinear systems. Phys. Rev. Lett. **87**, 165501 (2001)
13. Renger, T., Klinger, A., Steinecker, F., am Busch, M. S., Numata, J., Müh, F.: Normal mode analysis of the spectral density of the Fenna-Matthews-Olson light-harvesting protein: How the protein dissipates the excess energy of excitons. J. Phys. Chem. B **116**, 14565–14580 (2012)
14. Cole, D.J., Chin, A.W., Hine, N.D.M., Haynes, P.D., Payne, M.C.: Toward Ab initio optical spectroscopy of the Fenna-Matthews-Olson complex. J. Phys. Chem. Lett. **4**, 4206–4212 (2013)
15. Morgan, S., Cole, D., Chin, A.: Nonlinear network model analysis of vibrational energy transfer and localisation in the Fenna-Matthews-Olson complex. Nat. Sci. Rep. **6**, 36703 (2016)
16. Imhoff, J. F. *Biology of Green Sulfur Bacteria* (eLS, 2014)
17. Fenna, R.E., Matthews, B.W.: Chlorophyll arrangement in a bacteriochlorophyll protein from chlorobium limicola. Nature **258**, 573–577 (1975)
18. Adolphs, J., Renger, T.: How proteins trigger excitation energy transfer in the FMO complex of green sulfur bacteria. Biophys. J. **91**, 2778–2797 (2006)
19. Müh, F., Madjet, M.E.-A., Adolphs, J., Abdurahman, A., Rabenstein, B., Ishikita, H., Knapp, E.-W., Renger, T.: α-helices direct excitation energy flow in the Fenna-Matthews-Olson protein. Proc. Natl. Acad. Sci. **104**, 16862–16867 (2007)

20. Jia, X., Mei, Y., Zhang, J.Z., Mo, Y.: Hybrid QM/MM study of FMO complex with polarized protein-specific charge. Sci. Rep. **5**, 17096 (2015)
21. Blankenship, R. *Molecular Mechanisms of Photosynthesis*, 2nd edn Wiley-Blackwell (2014)
22. Savikhin, S., Buck, D.R., Struve, W.S.: Oscillating anisotropies in a bacteriochlorophyll protein: evidence for quantum beating between exciton levels. Chem. Phys. **223**, 303–312 (1997)
23. Engel, G., Calhourn, T., Read, E., Ahn, T.-K., Mancal, T., Cheng, Y.-C., Blankenship, R., Fleming, G.: Evidence for wavelike energy transfer through quantum coherence in photosynthetic systems. Nature **446**, 782–786 (2007)
24. Panitchayangkoon, G., Hayes, D., Fransted, K., Caram, J., Harel, E., Wen, J., Blankenship, R., Engel, G.: Long-lived quantum coherence in photosynthetic complexes at physiological temperature. Proc. Natl. Acad. Sci. **107**, 12766–12770 (2010)
25. Tiwari, V., Peters, W.K., Jonas, D.M.: Electronic resonance with anticorrelated pigment vibrations drives photosynthetic energy transfer outside the adiabatic framework. Proc. Natl. Acad. Sci. **110**, 1203–1208 (2013)
26. Renger, T., Marcus, R.A.: On the relation of protein dynamics and exciton relaxation in pigment-protein complexes: an estimation of the spectral density and a theory for the calculation of optical spectra. J. Chem. Phys. **116**, 9997 (2002)
27. Tirion, M.M.: Large amplitude elastic motions in proteins from a single-parameter, atomic analysis. Phys. Rev. Lett. **77**, 1905 (1996)
28. Hinsen, K.: Analysis of domain motions by approximate normal mode calculations. Proteins **33**, 417–429 (1998)
29. Krebs, W.G., Alexandrov, V., Wilson, C.A., Echols, N., Yu, H., Gerstein, M.: Normal mode analysis of macromolecular motions in a database framework: developing mode concentration as a useful classifying statistic. Proteins **48**, 682–695 (2002)
30. Bahar, I., Rader, A.: Coarse-grained normal mode analysis in structural biology. Curr. Opin. Struct. Biol. **15**, 586–592 (2005)
31. Bahar, I., Lezon, T.R., Yang, L.-W., Eyal, E.: Global dynamics of proteins: Bridging between structure and function. Annu. Rev. Biophys. **39**, 23–42 (2010)
32. Darmstadt, T. U.: Gaussian network model (2016). http://2012.igem.org/Team:TU_Darmstadt/Modeling_GNM
33. Xie, A., van der Meer, L., Hoff, W., Austin, R.H.: Long-lived amide I vibrational modes in myoglobin. Phys. Rev. Lett. **84**, 5435 (2000)
34. Piazza, F.: Nonlinear excitations match correlated motions unveiled by NMR in proteins: a new perspective on allosteric cross-talk. Phys. Biol. **11**, 036003 (2014)
35. Tronrud, D. E., Wen, J., Gay, L., Blankenship, R. E.: The structural basis for the difference in absorbance spectra for the FMO antenna protein from various green sulfur bacteria. Photosynth. Res. **100**, 79–87 (2009)
36. Hayward, S., de Groot, B.: Normal modes and essential dynamics. Methods Mol. Biol. **443**, 89–106 (2008)
37. Swope, W.C., Andersen, H.C., Berens, P.H., Wilson, K.R.: A computer simulation method for the calculation of equilibrium constants for the formation of physical clusters of molecules: Application to small water clusters. J. Chem. Phys. **76**, 637 (1982)
38. Dostál, J., Pšenčík, J., Zigmantas, D.: In situ mapping of the energy flow through the entire photosynthetic apparatus. Nat. Chem. (2016). Advance Online Publication
39. Acbas, G., Niessen, K.A., Snell, E.H., Markelz, A.: Optical measurements of long-range protein vibrations. Nat. Commun. **5**, 3076 (2014)
40. Wendling, M., Pullerits, T., Przyjalgowski, M.A., Vulto, S.I.E., Aartsma, T.J., van Grondelle, R., van Amerongen, H.: Electron-vibrational coupling in the Fenna-Matthews-Olson complex of prosthecochloris aestuarii determined by temperature-dependent absorption and fluorescence line-narrowing measurements. J. Phys. Chem. B **104**, 5825–5831 (2000)
41. Nalbach, P., Mujica-Martinez, C.A., Thorwart, M.: Vibronically coherent speed-up of the excitation energy transfer in the Fenna-Matthews-Olson complex. Phys. Rev. E **91**, 022706 (2015)

42. Fokas, A.S., Cole, D.J., Chin, A.W.: Constrained geometric dynamics of the Fenna-Matthews-Olson complex: the role of correlated motion in reducing uncertainty in excitation energy transfer. Photosynth. Res. **122**, 275–292 (2014)
43. Hayes, D., Engel, G.S.: Extracting the excitonic Hamiltonian of the Fenna-Matthews-Olson complex using three-dimensional third-order electronic spectroscopy. Biophys. J. **100**, 2043–2052 (2011)
44. Zuehlsdorff, T.J., Hine, N.D.M., Payne, M.C., Haynes, P.D.: Linear-scaling time-dependent density-functional theory beyond the Tamm-Dancoff approximation: obtaining efficiency and accuracy with in situ optimised local orbitals. J. Chem. Phys. **143**, 204107 (2015)

Chapter 6
Conclusions

We must therefore not be discouraged by the difficulty of interpreting life by the ordinary laws of physics. For that is just what is to be expected from the knowledge we have gained of the structure of living matter. We must be prepared to find a new type of physical law prevailing in it.

Erwin Schrödinger [5]

In conclusion, from the organic material pentacene to the Fenna-Matthews-Olson complex, organic and biological light-harvesting systems exhibit novel and often counter-intuitive ultrafast dynamics. The mounting evidence that vibrations play crucial roles cannot be overlooked [1–4]. At the same time, this work also highlights the power of a number of new approaches in unravelling the dynamics of these systems; from 2DES to the nonlinear network model.

Having established a toolbox of methods to tackle organic and biological systems in Chap. 2, in Chap. 3 we used 2DES to study singlet fission in the organic semiconductor pentacene. 2DES can provide unprecedented insight into a system's electronic and vibrational properties, effectively allowing its Hamiltonian to be mapped. This unrivalled level of information, alongside a thorough analysis of the 2DES data, enabled us to directly observe the 'dark' multiexcitonic state which mediates fission in pentacene for the first time. Our work suggests that vibrations could drive the fission process and led us to propose a theoretical model for pentacene in which vibrations are included at the same level as the electronic states and which can reproduce both the ultrafast fission timescale and the experimental beating maps. Having studied 2DES results in an organic material, in Chap. 4 we turned to the more complex biological system, PSII. Here we discussed the difficulty of using wavelet analysis to distinguish interference between vibrations with similar frequencies and oscillations from electronic coherences, which theoretical work has proposed may be regener-

S.E. Morgan, *Ultrafast Quantum Effects and Vibrational Dynamics in Organic and Biological Systems*, Springer Theses, DOI 10.1007/978-3-319-63399-2_6

ated over time [1]. We concluded that the wavelet analysis results should be treated with care and that theoretical simulations are essential to understand the origins of the signals and to rule out effects from interference between vibrations or padding effects.

Future work should focus on understanding the molecular details of vibrations and ultrafast dynamics in organic and biological systems. For example, the role of specific vibrations in driving fission could be studied at an electronic structure level, using ab initio methods to explicitly assign modes which are involved in the fission process. Pentacene dimers offer a promising system to apply this approach to, since they exhibit a smaller system size with more constrained dynamics and a slower fission rate.

In biological systems the nonlinear network model represents a promising approach to study large, complicated proteins in a computationally inexpensive way. In Chap. 5 we applied this model to the Fenna-Matthews-Olson complex for the first time. We found evidence for discrete breather modes, which are highly localised and may enable vibrational energy to be transferred to biologically relevant parts of the complex. Including a mode based on the observed discrete breather dynamics in our calculations of the optical spectra using ab initio site energies and excitonic couplings improved the agreement with experimental results. To go further, more accurate theoretical models are required, as well as experimental work to test theoretical studies and to suggest future directions. More generally network methods are a powerful tool to study the underlying structure and dynamics of a wide range of complex systems; from brain networks to airline route maps. Many open questions remain, for example what the relationship is between the structure and function of networks and the extent to which networks are determined by structural constraints. Across the board, in order to make progress it is essential for biologists and physicists to work closely together to understand the details of biological systems and build physical models which are able to capture the essential features.

Ultimately, biological systems have evolved to function out of equilibrium and often exhibit non-linear effects. They could therefore open the doorway to a very different regime of physics. If we can understand how these systems function on ultrafast timescales at the microscopic level, new approaches for device design are likely to emerge. Nature may have evolved to exploit nanostructuring and dynamical environment engineering, perhaps including environments whose spatial dependence varies with time. Learning from nature could enable us to design smart devices, for example devices made from sustainable materials, with improved robustness and/or the ability to self-repair.

In the words of Erwin Schröinger, *"to the physicist the state of affairs is not only not plausible but most exciting, because it is unprecedented."* [5]

References

1. Chin, A., Prior, J., Rosenbach, R., Caycedo-Soler, F., Huelga, S., Plenio, M.: The role of non-equilibrium vibrational structures in electronic coherence and recoherence in pigment-protein complexes. Nat. Phys. **9**, 113–118 (2013)
2. Kolli, A., O Reilly, E. J., Scholes, G. D., Olaya-Castro, A.: The fundamental role of quantized vibrations in coherent light harvesting by cryptophyte algae. J. Chem. Phys. **137**, 174109 (2012)
3. O Reilly, E. J., Olaya-Castro, A.: Non-classicality of the molecular vibrations assisting exciton energy transfer at room temperature. Nat. Commun. **5**, 3012 (2014)
4. Tiwari, V., Peters, W.K., Jonas, D.M.: Electronic resonance with anticorrelated pigment vibrations drives photosynthetic energy transfer outside the adiabatic framework. Proc. Natl. Acad. Sci. **110**, 1203–1208 (2013)
5. Schrödinger, E.: *What is life? The Physical Aspect of the Living Cell.* (Cambridge University Press, 1944)

Appendix A
The Density Matrix and Reduced Density Matrix

A.1 Density Matrix

Here we give a brief introduction to density matrices. This discussion is based on Blum [1] and further information can be found there. If $|\psi\rangle$ is a pure quantum state, the density operator is defined as: $\rho = |\psi\rangle\langle\psi|$. Expanding $|\psi\rangle$ as a linear superposition of the basis states $|n\rangle$, we obtain:

$$|\psi\rangle = \sum_n c_n |n\rangle \tag{A.1}$$

Hence:

$$\rho = \sum_{n,m} c_n c_m^* |n\rangle\langle m| \tag{A.2}$$

Then the density matrix, ρ_{nm}, can be expressed as:

$$\rho_{nm} \equiv \langle n|\rho|m\rangle = c_n c_m^* \tag{A.3}$$

Furthermore, in this representation the expectation value of an operator A is given by:

$$\langle A\rangle = \mathrm{Tr}(\rho A) \tag{A.4}$$

Note that density matrices are particularly useful for mixed states (which can only be represented as statistical distributions). A mixture of the states $|\psi_n\rangle$ with statistical weights W_n is represented by the density operator [1]:

$$\rho = \sum_n W_n |\psi_n\rangle\langle\psi_n| \tag{A.5}$$

S.E. Morgan, *Ultrafast Quantum Effects and Vibrational Dynamics in Organic and Biological Systems*, Springer Theses, DOI 10.1007/978-3-319-63399-2

A.2 Reduced Density Matrix

When including dissipation in our model (see Sect. 2.2), we are only interested in the behaviour of the system over time (described by the system's Hamiltonian, H, Eq. 2.6); not in the behaviour of the bath. Therefore we use a reduced density matrix, which contains all of the information concerning the system (including how it evolves over time due to its interaction with the bath), but discards unnecessary information concerning the bath itself. To calculate the reduced density matrix for the system, $\rho(t)_S$ we take the total density matrix, $\rho(t)$, and trace over the bath degrees of freedom [1]:

$$\rho(t)_S = Tr_B \rho(t) \tag{A.6}$$

Appendix B
Interaction Picture

We also make use of the interaction picture, as described (for example) by Blum [1] or Hamm [2]. The interaction picture splits the total Hamiltonian into two parts; an interaction term V(t) and a Hamiltonian describing the rest of the system:

$$H(t) = H_0 + V(t) \tag{B.1}$$

This is helpful when the interaction V(t) is small so that the eigenstates of H_0 provide a good basis for the full system. Comparing Eq. B.1 with Eq. 2.11, $H(t)=H_{total}$, $H_0=H+H_B$ and $V(t)=H_{IB}$.

Following Blum [1], the density matrix in the interaction picture is given by:

$$\rho(t)_I = U_0^{\dagger}(t)\rho(t)U_0(t) \tag{B.2}$$

with the time evolution operator:

$$U_0(t) = e^{-(i/\hbar)H_0 t} \tag{B.3}$$

It obeys the Liouville equation in the interaction picture:

$$i\hbar\frac{\partial\rho(t)_I}{\partial t} = [V(t)_I, \rho(t)_I] \tag{B.4}$$

By formally integrating this expression, we obtain:

$$\rho(t)_I = \rho(0)_I - \frac{i}{\hbar}\int_0^t [V(\tau)_I, \rho(\tau)_I]d\tau \tag{B.5}$$

S.E. Morgan, *Ultrafast Quantum Effects and Vibrational Dynamics in Organic and Biological Systems*, Springer Theses, DOI 10.1007/978-3-319-63399-2

Then by substituting Eq. B.5 back into Eq. B.4, and switching to a reduced density matrix representation, we find:

$$\dot{\rho}(t)_{SI} = -(i/\hbar)Tr_B[V(t)_I, \rho(0)_I] - (1/\hbar)^2 \int_0^t d\tau Tr_B[V(t)_I, [V(\tau)_I, \rho(\tau)_I]] \tag{B.6}$$

This equation forms the basis of Bloch-Redfield theory, described in Sect. 2.2.

References

1. Blum, K.: Density Matrix Theory and Applications. Springer (1981)
2. Hamm, P.: Principles of nonlinear optical spectroscopy: a practical approach (2005). http://www2.chemistry.msu.edu/faculty/beck/CEM987/downloads/Hamm.pdf